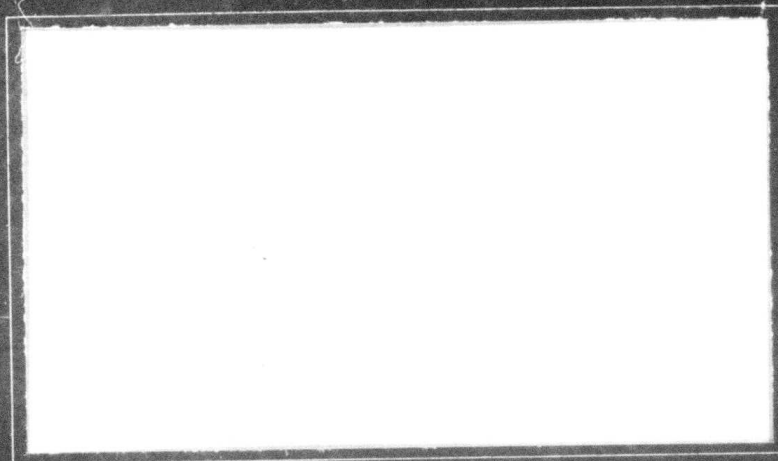


**Best Available  
Copy  
for all Pictures**

AD A014564



18

# *Microwave Laboratory*

W. W. HANSEN LABORATORIES OF PHYSICS

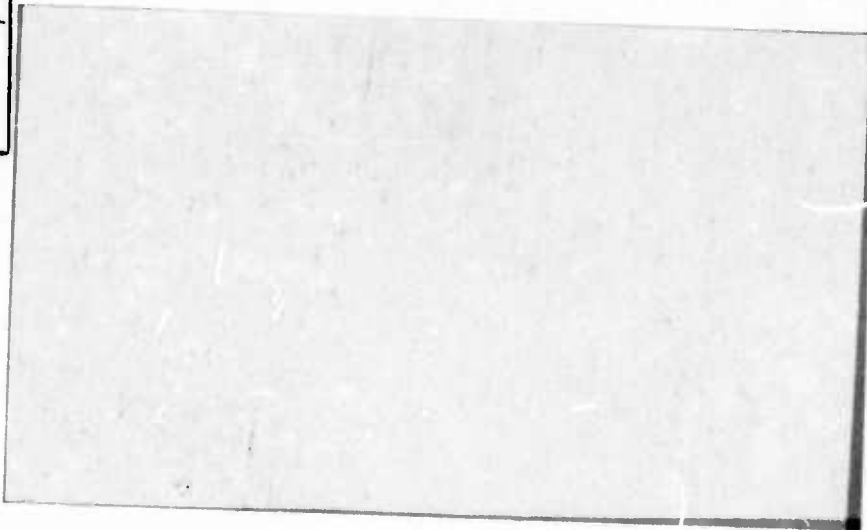
STANFORD UNIVERSITY • STANFORD, CALIFORNIA



DDC  
REF ID: A61017  
MAR 30 1970  
LIBRARY

50

ACCESSION 1A		✓
NTIS	White Section	<input checked="" type="checkbox"/>
DOC	Bufi Section	<input type="checkbox"/>
UNANNOUNCED		<input type="checkbox"/>
JUSTIFICATION.....		
BY.....		
DISTRIBUTION/AVAILABILITY CODES		
Dist.	AVAIL. and/or SPECIAL	
A		



ACOUSTIC WAVE SEMICONDUCTOR CONVOLVER APPLIED TO  
ELECTRICAL AND OPTICAL SIGNAL PROCESSING

by

H. R. Gautier

M. L. Report No. 2448

June 1975

Technical Report

Contract: N00014-67-A-0112-0084

ARPA Order No. 2778

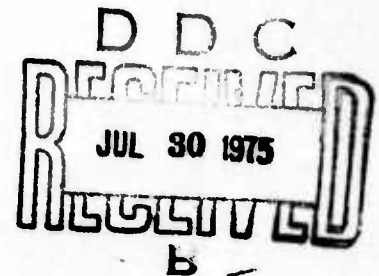
Program Code No. 4D10

Scientific Officer:

Director, Physics Program  
Physical Sciences Division  
Office of Naval Research  
Department of the Navy  
800 North Quincy Street  
Arlington, Virginia 22217

Gordon S. Kino  
Principal Investigator  
(415) 497-0205

Microwave Laboratory  
W. W. Hansen Laboratories of Physics  
Stanford University  
Stanford, California



DISTRIBUTION STATEMENT A

Approved for public release;  
Distribution Unlimited



UNCLASSIFIED

SECURITY CLASSIFICATION OF THIS PAGE (When Data Entered)

REPORT DOCUMENTATION PAGE		READ INSTRUCTIONS BEFORE COMPLETING FORM
1. REPORT NUMBER	2. GOVT ACCESSION NO.	3. RECIPIENT'S CATALOG NUMBER
4. TITLE (and Subtitle) ACUSTIC WAVE SEMICONDUCTOR CONVOLVER APPLIED TO ELECTRICAL AND OPTICAL SIGNAL PROCESSING.		5. TYPE OF REPORT & PERIOD COVERED Interim rept.
7. AUTHOR(s) H. R. Gautier		6. PERFORMING ORG. REPORT NUMBER M.L. Report No. 2448
9. PERFORMING ORGANIZATION NAME AND ADDRESS Microwave Laboratory W.W. Hansen Laboratories of Physics Stanford University, Stanford, CA 94305		8. CONTRACT OR GRANT NUMBER(s) N00014-67-A-0112-0081 ARPA Order-2778
11. CONTROLLING OFFICE NAME AND ADDRESS Advanced Research Projects Agency 1400 Wilson Boulevard Arlington, Virginia 22209		10. PROGRAM ELEMENT, PROJECT, TASK AREA & WORK UNIT NUMBERS ARPA Order No. 2778 Program Code No. 4D10
14. MONITORING AGENCY NAME & ADDRESS (if different from Controlling Office) Director, Physics Program, Physical Sciences Office of Naval Research Division, Department of the Navy 800 North Quincy St., Arlington, Virginia 22217		12. REPORT DATE June 1975
16. DISTRIBUTION STATEMENT (of this Report) ML-2448		13. NUMBER OF PAGES 172 (123 84 p.)
17. DISTRIBUTION STATEMENT (of the abstract entered in Block 20, if different from Report)		15. SECURITY CLASS. (of this report) UNCLASSIFIED
18. SUPPLEMENTARY NOTES		15a. DECLASSIFICATION/DOWNGRADING SCHEDULE
19. KEY WORDS (Continue on reverse side if necessary and identify by block number) Real time convolution convolution interaction optical signal processing convolution efficiency optical image transforms signal-to-noise ratio optical image scanning dark current		
20. ABSTRACT (Continue on reverse side if necessary and identify by block number) This work presents an experimental and theoretical study of the interactions between acoustic surface waves on a piezoelectric insulator and charge carriers in a neighboring semiconductor separated by a small airgap; and the application of these phenomena to signal processing and optical imaging. Although the two media are mechanically isolated, the electric field associated with the surface waves penetrate into the semiconductor and interact with its charge carriers. This interaction is nonlinear, and, in the case of two oppositely propagating surface waves, real time convolution is		

DD FORM 1 JAN 73 1473

EDITION OF 1 NOV 65 IS OBSOLETE

UNCLASSIFIED

SECURITY CLASSIFICATION OF THIS PAGE (When Data Entered)

229 250

~~UNCLASSIFIED~~

SECURITY CLASSIFICATION OF THIS PAGE(When Data Entered)

performed.

A new theory of the convolution interaction, taking into account the possible presence of a depletion, inversion or accumulation layer at the surface of the semiconductor, resulting from a built-in or applied dc field is presented. Experimental measurements for both n- and p-type Silicon on Lithium Niobate systems are in very good agreement with this theory, and they lead to a novel technique of measurement of the surface state distribution on semiconductors.

The silicon on lithium niobate structure used gives rise to one of the largest convolution efficiencies reported to date. Several signal processing applications are presented. They show the versatility of the device which can be employed as a programmable filter or a parametric processor. In addition, the first autocorrelation is demonstrated by cascading two convolvers.

The acoustic convolver was adapted for the scanning of optical images. The convolution efficiency can be modulated by the local variations of the illumination of the semiconductor and the scanning is performed by the acoustic surface waves. We present a simple method of reducing the dark current to arbitrary level and hence increase the optical dynamic range. The problem of light sensitivity is treated qualitatively for the various semiconductor regimes.

A major advance is the use of the device to obtain transforms of optical images. We have obtained Fourier and Fresnel transforms of an optical image. A spectrum analyzer or a matched delay line filter is used for the reconstruction of the original image. By this means, arbitrary scan rates were achieved, large increases in signal-to-noise ratio realized and the bandwidth of the transmitted signal was radically reduced. Several examples of these types of optical signal processing are presented, and analyzed.

UNCLASSIFIED

SECURITY CLASSIFICATION OF THIS PAGE(When Data Entered)

This research was supported by the Advanced Research Projects Agency of the Department of Defense and was monitored by ONR under Contract No. N00014-67-A-0112-0084

---

Disclaimer: The views and conclusions contained in this document are those of the authors and should not be interpreted as necessarily representing the official policies, either expressed or implied, of the Advanced Research Projects Agency or the U. S. Government.

# ABSTRACT

This work presents an experimental and theoretical study of the interactions between acoustic surface waves on a piezoelectric insulator and charge carriers in a neighboring semiconductor separated by a small airgap; and the application of these phenomena to signal processing and optical imaging. Although the two media are mechanically isolated, the electric field associated with the surface waves penetrate into the semiconductor and interact with its charge carriers. This interaction is nonlinear and, in the case of two oppositely propagating surface waves, real time convolution is performed.

A new theory of the convolution interaction, taking into account the possible presence of a depletion, inversion or accumulation layer at the surface of the semiconductor, resulting from a built-in or applied dc field, is presented. Experimental measurements for both n- and p-type Silicon on Lithium Niobate systems are in very good agreement with this theory, and they lead to a novel technique of measurement of the surface state distribution on semiconductors.

The Silicon on Lithium Niobate structure used gives rise to one of the largest convolution efficiencies reported to date. Several signal processing applications are presented. They show the versatility of the device which can be employed as a programmable filter or a parametric processor. In addition, the first autocorrelation is demonstrated by cascading two convolvers.

The acoustic convolver was adapted for the scanning of optical images. The convolution efficiency can be modulated by the local variations of the illumination of the semiconductor and the scanning is performed by the acoustic surface waves. We present a simple method of reducing the dark current to arbitrary level and hence increase the optical dynamic range. The problem of light sensitivity is treated qualitatively for the various semiconductor regimes.

A major advance is the use of the device to obtain transforms of optical images. We have obtained Fourier and Fresnel transforms of an optical image. A spectrum analyzer or a matched delay line filter is used for the reconstruction of the original image. By this means, arbitrary scan rates were achieved, large increases in signal-to-noise ratio realized and the bandwidth of the transmitted signal was radically reduced. Several examples of these types of optical signal processing are presented, and analyzed.



## TABLE OF CONTENTS

	<u>Page</u>
ABSTRACT . . . . .	iii
ACKNOWLEDGEMENTS . . . . .	v
LIST OF FIGURES . . . . .	ix
LIST OF TABLES . . . . .	xii
CHAPTER I. INTRODUCTION . . . . .	1
CHAPTER II. GENERAL CONVOLUTION THEORY AND EXPERIMENTAL	
RESULTS . . . . .	7
2.1 Preliminary Study . . . . .	9
2.1.1 Basic Convolution Mechanism. . . . .	9
2.1.2 Basic Explanation of the Convolution	
Variation with Bias. . . . .	13
2.2 Complete Theory . . . . .	23
2.2.1 General Discussion . . . . .	23
2.2.2 Nonlinear Coupling . . . . .	25
2.2.3 Equivalent Circuit . . . . .	32
2.2.4 Acoustic Impedance . . . . .	42
2.3 Theoretical and Experimental Results. . . . .	43
2.3.1 Flat Band Conditions . . . . .	43
2.3.2 Results for Untreated Silicon Sur-	
faces - Deep Depletion Model . . . . .	47
2.3.3 Oxidized Silicon - Off Flat Band	
Results - Surfaces States. . . . .	53
2.4 Concluding Remarks. . . . .	68



## TABLE OF CONTENTS (Cont'd)

	<u>Page</u>
CHAPTER III. APPLICATIONS OF THE SEMICONDUCTOR CONVOLVER	
TO ACOUSTIC PARAMETRIC SIGNAL PROCESSING. . . . .	70
3.1 Convolution. . . . .	72
3.2 Other Signal Processing Applications . . . . .	82
CHAPTER IV. OPTICAL SIGNAL PROCESSING AND IMAGING . . . . .	92
4.1 Introduction . . . . .	92
4.2 Improved Sensitivity Imaging Devices . . . . .	97
4.2.1 Dark Signal Reduction - General	
Principle . . . . .	98
4.2.2 Light Sensitivity and Dynamic	
Range . . . . .	104
4.2.3 Example of "Direct" Imaging . . . . .	123
4.3 Transform Techniques Applied to Optical	
Imaging. . . . .	126
4.3.1 Spatial Fresnel Transform and	
Imaging . . . . .	127
4.3.2 Spatial Fourier Transform and	
Imaging . . . . .	136
CHAPTER V. CONCLUSIONS . . . . .	149
APPENDIX A. IMAGING BY TRANSFORM CODING . . . . .	152
APPENDIX B. SILICON CLEANING AND OXIDATION PROCEDURES . . . . .	165
REFERENCES. . . . .	167

## LIST OF FIGURES

<u>Figure</u>	<u>Page</u>
2.1-1 Basic convolver geometry. . . . .	10
2.1-2 Experimental measurement of convolution efficiency and propagation loss vs bias voltage. . . . .	19,20
2.2-1 Plot of the nonlinear coupling coefficient vs dc surface potential . . . . .	31
2.2-2 Equivalent circuit used in the evaluation of linear coupling and loss . . . . .	36
2.2-3 Plot of reduction factor $\mathcal{R}$ vs inversion strength $g^+$ . . . . .	41
2.3-1 Propagation loss and $\mathcal{M}$ -values vs conductivity. . .	45,46
2.3-2 $\mathcal{M}$ -value vs dc surface potential in accumulation and depletion . . . . .	49
2.3-3 Output equivalent circuit of the convolver. . . . .	50
2.3-4 (a) $\mathcal{M}$ -value and propagation loss vs bias voltage (n-type Si) . . . . .	56
(b) Voltage shift and surface state distribution. .	57
2.3-5 (a) $\mathcal{M}$ -value and propagation loss vs bias voltage (p-type Si) . . . . .	58
(b) Voltage shift and surface state distribution. .	59
2.3-6 Surface state density distribution in Si-SiO <sub>2</sub> structure . . . . .	61
2.3-7 Propagation loss vs inversion strength. . . . .	64

# LIST OF FIGURES (Cont'd)

<u>Figure</u>		<u>Page</u>
3.1-1	Schematic of the semiconductor convolver. . . . .	73
3.1-2	Examples of convolution and interaction uniformity with a BGO-Si convolver . . . . .	79
3.2-1	V-FM chirp pulse compression experiment . . . . .	84
3.2-2	7-bit and 11-bit Barker code correlation experi- ment. . . . .	85
3.2-3	Time inversion and autocorrelation experiments. . .	87
4.1-1	Two techniques for scanning optical images. . . . .	93
4.2-1	Schematic of imager with low dark current . . . . .	99
4.2-2	Output convolution of two square pulses with off- set center frequencies. . . . .	102
4.2-3	Dark signal reduction due to a frequency offset . .	103
4.2-4	Ratio of nondegenerate convolution power to degen- erate convolution power in dark vs frequency off- set for an $n/n^+$ silicon sample under light accumulation conditions . . . . .	114
4.2-5	Experimental convolution response to white illumi- nation. . . . .	116
4.2-6	(a) Schematic of the system used for direct imaging. . . . .	124
	(b) Direct imaging of a 2 mm period pattern. . . .	125
4.3-1	Schematic of the complete imaging system using Fresnel transforms. . . . .	128

# LIST OF FIGURES (Cont'd)

<u>Figure</u>		<u>Page</u>
4.3-2	Pictures taken with the system shown in Fig. 4.3-1.	133
4.3-3	Two-dimensional picture taken with the Fresnel transform system. . . . .	134
4.3-4	Principle of the generation of the Fourier transform in a semiconductor convolver . . . . .	137
4.3-5	Schematic of the system used for taking a Fourier transform . . . . .	140
4.3-6	(a) Fourier transform of a periodic grating. . . .	141
	(b) The inverse Fourier transform taken with a spectrum analyzer. . . . .	141
4.3-7	Examples of A-scans obtained with a Fourier transform imaging system . . . . .	143
4.3-8	Two-dimensional picture taken with a Fourier transform imaging system . . . . .	148
A-1	Design curves for the imaging systems by Fresnel transform . . . . .	161

# LIST OF TABLES

<u>Table</u>		<u>Page</u>
2.1	Material characteristics of two $\text{LiNbO}_3$ -Si convolver. . . . .	40
2.2	$M$ -values - Theory and experiment. . . . .	52
2.3	$M$ -values - Theory and experiment. . . . .	60
3.1	Device characteristics . . . . .	75
3.2	Comparison of various SAW convolvers . . . . .	81
4.1	Experimental study of the resolution in a Fourier transform imaging system . . . . .	146

## CHAPTER I

### INTRODUCTION

In this work we are concerned with acoustic surface waves on a piezoelectric substrate and their interactions with charge carriers in a neighboring separated semiconductor. Although the piezoelectric and the semiconductor media are mechanically isolated due to the presence of an airgap between the two surfaces, the coupling is achieved through the electric fields which accompany the surface waves and which extend outside the piezoelectric into the semiconductor.

We are particularly interested in the study of these interactions for the purpose of VHF signal processing and optical imaging. Extensive work has been done in the past to develop acoustic wave amplifiers,<sup>1,2</sup> which are based on linear processes. More recently, nonlinear coupling mechanisms have been investigated, and, based on these principles, real time convolution devices,<sup>3-6</sup> acoustic parametric amplifiers,<sup>7</sup> and optical imaging devices<sup>8,9,10</sup> have been developed. The semiconductor medium is either separated from the piezoelectric (as in the works just cited) or directly deposited on it, thus forming a monolithic structure.<sup>11-14</sup> There is also a third family of devices which employ piezoelectric semiconductors, like GaAs.<sup>15,16,17</sup>

The structure which is treated throughout this work is composed of two crystalline materials. Firstly, a piezoelectric crystal, in



the shape of a long bar, with a very well polished surface. High efficiency interdigital transducers<sup>18</sup> are deposited on the piezoelectric material; and when an rf electric signal is fed into them, acoustic stresses are generated at the surface of the acoustic medium and acoustic surface waves are launched. Several types of surface waves may exist, and with the materials employed here, we are only concerned with the so-called Rayleigh waves.<sup>18</sup> Although the vibrational field is limited to the piezoelectric material, the concomitant electric field extends some distance outside it. Therefore, if a semiconductor - the second crystalline material - is placed close enough to the surface of the delay line, the electric fields associated with the acoustic waves can penetrate into the semiconductor and act on the charge carriers. The carriers will react to the electric field. As a reaction to the longitudinal component of the fields, a bunching of carriers will occur along the surface, resulting in wave attenuation. In addition, the normal component of the electric field will tend to deplete or accumulate the surface of the semiconductor. While the potential dropped across an accumulation layer is very small, the potential generated across a depletion layer is large and it is proportional to the square of the total electric field at the surface. In other words, the device measures the capacity of the depletion layer, which is a nonlinear function of the field. The nonlinear behavior of this potential is the basis for parametric coupling or mixing of acoustic waves. In the case of oppositely propagating surface waves at the same frequency, a uniform

potential is generated at the double frequency and, as a function of time, it represents the convolution of the modulations of the input signals.

Such a device, capable of taking the convolution of two functions, has very important applications in the signal processing field.<sup>19</sup> Indeed, if one of the inputs signals is regarded as a reference, the convolution device may be considered as a linear filter whose impulse response is the reference signal and can therefore be programmed at will. A matched filter is particularly simple to make; one only has to use, as the reference, the time inverted replica of the signal to which the filter has to be matched. Other applications include time inversion schemes and hence the possibility of making a correlator, and real time Fourier transform.

The basic nonlinear effect, as we presented it earlier, is the generation of a depletion layer at the surface of the semiconductor, with an acoustic read-out of its value. The thickness of this depletion layer is a function of the carrier concentration. Therefore, if extra charges are optically produced, the depletion layer is changed and so is the nonlinear output voltage. By opposition to a classical photodetector, this device does not measure the photocurrent passing through it, but the change in depletion layer caused by illumination. The read-out is therefore non-destructive. This principle was first suggested by Quate<sup>8</sup> and with the original system, the scanning was done by a short acoustic wave pulse. This pulse moved along the delay line at the acoustic wave velocity and it sensed changes in

the carrier density caused by local variations in the intensity of the light. This scanning has the merit of being simple but it raises several problems, namely, a high inherent dark signal and a limited sensitivity. In addition, there is a trade-off between dynamic range and resolution, and finally, the scan velocity is fixed.

The two phenomena of convolution generation and optical imaging are investigated in this work. Both n- and p-type silicon have been used with  $\text{LiNbO}_3$  or  $\text{Bi}_{12}\text{GeO}_{20}$  piezoelectric substrates. Lithium niobate was chosen for its strong piezoelectricity;  $\text{Bi}_{12}\text{GeO}_{20}$  for its slow acoustic surface wave velocity. The only semiconductor employed was silicon because of the extended knowledge of its surface properties and because of the good controllability over its parameters.

This study is divided into three parts. In Chapter II, we present a new theory of the acoustic surface wave convolver. Its operation is now well understood and confirmed experimentally in all regimes, i.e., depletion at the surface, at flat band, with an accumulated surface or with an inversion layer at the surface. This understanding was necessary for the design of high efficiency devices and this study was also a vital step in the development of sensitive optical imaging devices. Furthermore, previously published theories only cover the flat band case; we have shown that this is not the optimum regime of operation and moreover, very few semiconductors are naturally operated in this regime, due to the presence of localized states at the surface of the semiconductors. Throughout this study, a new method of measurement of the "surface state" distribution on silicon has been proposed

and made. It employs the acoustic field to measure the surface properties and offers the unique feature of using oxidized silicon without requiring deposition of metal films.

A more device-oriented experimental study of the convolver is presented in Chapter III. Particular emphasis is put on the terminal characteristics and performances of the device as a signal processor. Also comparisons are made with other competing acoustic systems. We have experimented with various signal processing schemes such as convolution, code recognition, time inversion and, for the first time, real time correlation was demonstrated by cascading two devices. Finally, several technological difficulties are discussed: they are related to the problem of maintaining a uniform and small airgap (a few thousands angstroms) between the piezoelectric and the semiconductor media. In addition, the semiconductor surface is unprotected and has a tendency to become contaminated if no precautions are taken.

In Chapter IV we show how the semiconductor convolver was used as an optical imaging device. A new technique has been developed to reduce the dark signal to arbitrarily low levels and hence greatly enhance the dynamic range and the sensitivity of the system. A quantitative study of the light sensitivity of the device is given and compared to simple theoretical predictions.

With the acoustic semiconductor convolver, we have been able to obtain directly, in real time, in the device, Fresnel and Fourier spatial transforms of an optical image. The original images have

been reconstructed by carrying out the inverse transforms. In the case of the Fresnel transform, we do this by inserting the output signal, which is in the form of an rf chirp, into a dispersive delay line. In the case of the Fourier transform, we take the inverse transform by using a spectrum analyzer or another acoustic convolver. The employment of such signal processing techniques leads to an improvement in signal-to-noise ratio corresponding to several times the number of spots in a line. This is basically because we are using the pulse compression concepts of radar in optical imaging. It implies that we read off the signal from one single spot in the line time rather than in the scan time of one spot. This is an entirely new technique for scanning an optical image. This same technique also provides arbitrary line time and output bandwidth. Several imaging systems using these signal processing schemes have been demonstrated and an experimental and theoretical study of their characteristics and limitations is presented in Chapter IV.

## CHAPTER II

### GENERAL CONVOLUTION THEORY AND EXPERIMENTAL RESULTS

In this chapter we shall give a description of the structure of the semiconductor airgap piezoelectric convolver. A simplified theory relying on the depletion layer approximation will then be described: this will introduce the concept of the varactor-like behavior of the system and will show from where the nonlinear field-potential relation arises and how the system can be used to take the convolution product of electrical signals.

The structure to which all the work reported here applies, is illustrated in Fig. 2.1-1. An acoustic surface wave delay line is made of a piezoelectric material with a well polished top surface. Surface waves, i.e., waves which decay rapidly away from the surface, are generated by applying electrical signals to interdigital transducers deposited on the surface of the material. Because of the piezoelectric nature of the substrate, an acoustoelectric field is associated with each wave. A semiconductor, such as Silicon, is placed in close proximity to the surface of the acoustic delay line. The airgap present between the semiconductor and the piezoelectric surfaces is required to keep the semiconductor from mass loading the piezoelectric. When the airgap is small, the electric field penetrates into the semiconductor and act with its carriers.

This surface wave-carrier coupling depends on the geometry of the device; it is also sensitive to the surface properties of the



semiconductor. It can therefore be controlled by varying the state of the semiconductor surface. This can simply be done by applying a biasing voltage to the MIS structure. To be able to choose the optimum geometry and the optimum operating conditions for the convolver and the optical imaging device derived from it, a detailed study of the interaction process is needed, and should be carried out for all surface conditions.

Several theories have been published.<sup>5,3,20,21</sup> Although some of those theories are mathematically rigorous, it is difficult to understand from them the basic physical processes underlying the convolution phenomenon; moreover, except for the work by Takada, et al.,<sup>21</sup> they only apply to the flat band case. To avoid these difficulties, we have developed a somewhat different theory making certain assumptions, valid in all the cases of practical interest, which lead to considerable simplification in the theory and a better physical insight into the nonlinear phenomenon involved. When the energy bands are bent in the semiconductor, under the influence of an external biasing voltage, simple physical models are used with the same goal. This study also provides an understanding of the effect of the surface states present on the semiconductor. The results of the analysis suggest a novel technique for measuring their density distribution across the energy gap of the semiconductor.

## 2.1 PRELIMINARY STUDY

### 2.1.1 The Basic Convolution Mechanism

We refer to the schematic shown in Fig. 2.1-1, which represents the convolver structure. When the airgap is small, the electric field associated with a surface wave can interact with the carriers in the semiconductor. To obtain a more precise idea of how this interaction takes place, we consider the simplest regime of operation, the "depletion" regime and we make use of the depletion layer approximation.<sup>22</sup> Any electric field  $E$  normal to the surface of the semiconductor produces a depletion layer of thickness  $l$  where

$$E = -qN_d l / \epsilon \quad . \quad N_d \text{ is the donor density of the assumed n-type semiconductor, } q \text{ the electronic charge and } \epsilon \text{ the permittivity of the semiconductor.}$$

In turn, this implies that there will be a potential developed across the depletion layer, of value  $\phi = -qN_d l^2 / 2\epsilon$  or

$$\phi = -\epsilon E^2 / 2qN_d \quad . \quad (2.1-1)$$

In this case,  $-\epsilon/2qN_d$  is the nonlinear coupling coefficient. Hence a normal component of electric field  $E$  at the surface creates a potential which is proportional to the square of the field. This is the mechanism that takes place in a varactor; but whereas a varactor is generally voltage driven, the semiconductor convolver can be considered as a displacement current or an E-field driven varactor.

When the device is operated as a convolver, two waves are launched at frequencies  $\omega_1$  and  $\omega_2$  respectively, in opposite directions by

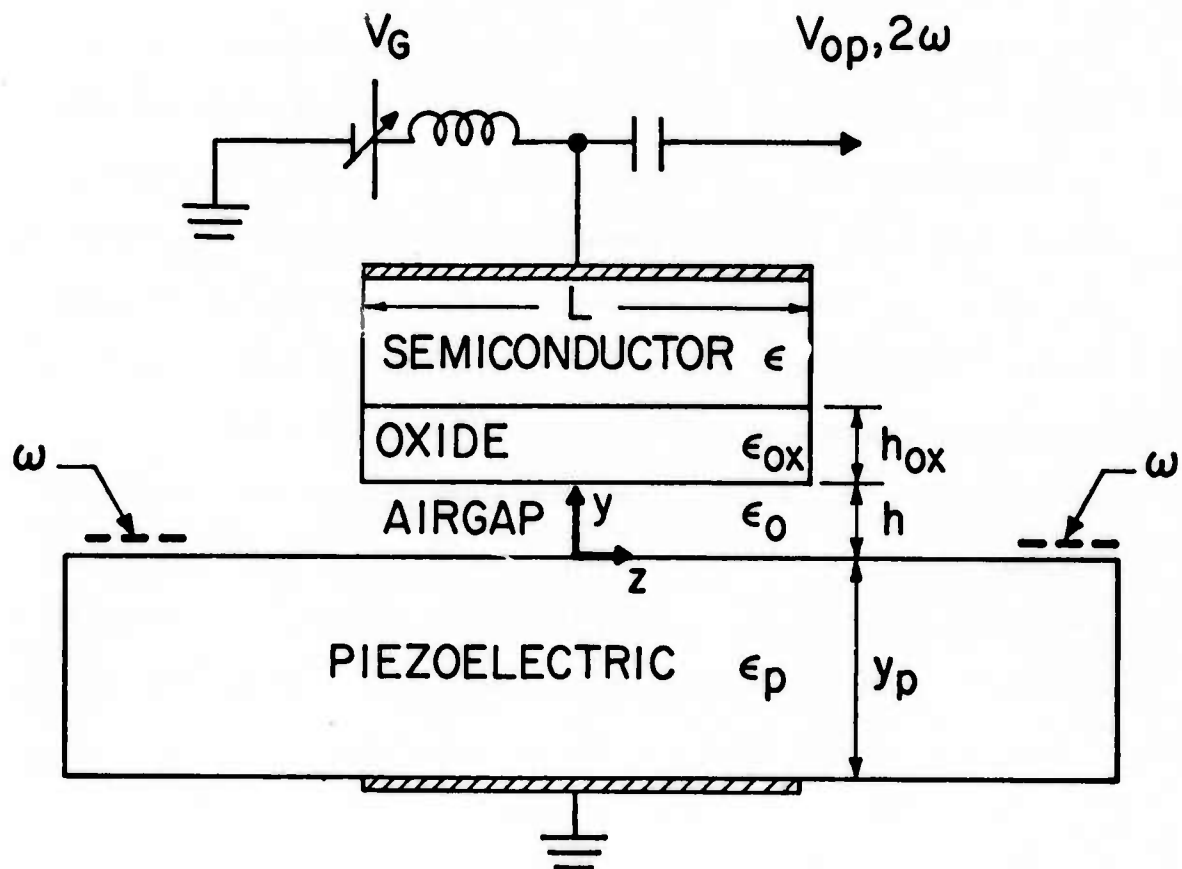


FIG. 2.1-1--Basic convolver geometry.

means of interdigital transducers. If we take the center of the semiconductor as the origin  $z = 0$  and neglect the propagation loss for the time being, these waves have fields that vary as

$$f_1(t - z/v) \exp [j\omega_1(t - z/v)] \quad \text{and} \quad f_2(t + z/v) \exp [j\omega_2(t + z/v)]$$

respectively;  $v$  is the surface wave velocity and  $f_1$  and  $f_2$  are the modulations of the input signals. Because of the nonlinearity associated with the semiconductor, a potential will be developed across the depletion layer which is proportional to the product of these two signals, which has a variation of the form

$$\exp j[(\omega_1 + \omega_2)t - (\omega_1 - \omega_2)z/v] \quad .$$

In the degenerate case, the two input signals are at the same frequency  $\omega = \omega_1 = \omega_2$  and the potential  $\phi$  is uniform along the length of the depletion layer. It can be detected between a metal plane electrode on the top surface of the semiconductor and a plane electrode on the lower surface of the delay line. In this case, the open circuit output signal takes the form

$$V_{op} = \mathcal{A} \exp(2j\omega t) \int_{-L/2}^{L/2} f_1(t - z/v) f_2(t + z/v) dz \quad (2.1-2)$$

where  $\mathcal{A}$  is a constant evaluated in Sections 2.2.2 and 2.3.1, and  $L$  is the length of the semiconductor. If we suppose that the modulated signals exist for a time shorter than the acoustic delay along

the semiconductor, we can take the limits of integration to infinity; and with the change of variable  $t - z/v = \tau$ , the output signal takes the final form

$$V_{op} = \mathcal{A} v \exp(2j\omega t) \int_{-\infty}^{+\infty} f_1(\tau) f_2(2t - \tau) d\tau \quad (2.1-3)$$

The output is seen to be the true convolution of the modulations of the two inputs, compressed by a factor of 2, and it is the modulation of a carrier with a frequency twice the input frequency.

Since the semiconductor is uniform, it is best suited to detect spatially invariant potentials. For this reason, the semiconductor convolver is generally operated in a degenerate mode, i.e., with identical input frequencies. Non-degenerate operation is nevertheless possible and of interest.

More generally, we can assume that the coupling coefficient  $\mathcal{A}$  is nonuniform along the semiconductor  $\mathcal{A} = \mathcal{A}(z)$ . The output voltage  $V_{op}$  should then be expressed as follows:

$$V_{op} = \exp(2j\omega t) \int_{-L/2}^{L/2} \mathcal{A}(z) f_1(t - z/v) f_2(t + z/v) dz \quad (2.1-4)$$

Equation (2.1-4) provides a different interpretation of the mathematical operation which takes place in the device. Instead of considering the output as the convolution product of the two electrical inputs, we can view it as an integral transform of the silicon-piezoelectric coupling distribution  $\mathcal{A}(z)$ . In this case, the maximum

duration of the input signals is not necessarily limited to the acoustic delay time along the semiconductor.

We shall make extensive use of these two remarks in Chapter IV when we describe the optical imaging device. In this application,  $\mathcal{A}(z)$  will be a function of the illumination, i.e., of the optical input signal.

### 2.1.2 Basic Explanation of the Convolution Variation with Bias Voltage

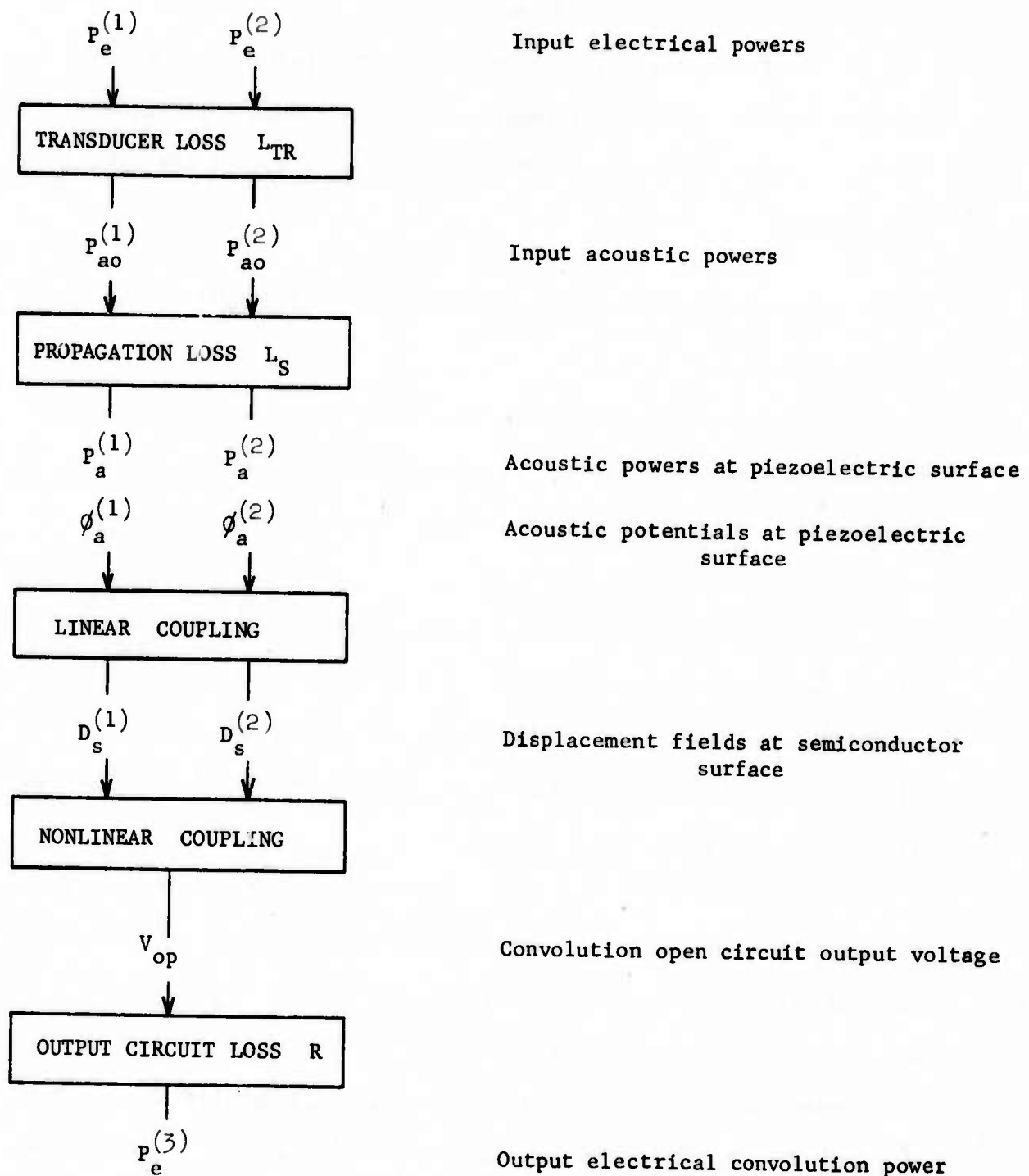
In the preceding section, we showed, in a simple example, how the semiconductor can supply a nonlinear mechanism and how this can be used to perform certain mathematical functions, namely the convolution of two signals.

We are now going to define and study qualitatively the efficiency of the device and how it depends on the material parameters and the operating conditions. To do this we must determine the various mechanisms leading to the generation of the output convolution signal. The flow graph in Chart I will be used.

We denote by  $P_e^{(1)}$  and  $P_e^{(2)}$  the input electrical powers. Due to the transducer loss, the corresponding acoustic powers in the acoustic waves right after their generation are  $P_{ao}^{(1)} < P_e^{(1)}$  and  $P_{ao}^{(2)} < P_e^{(2)}$ . As the surface waves propagate, they are influenced by the presence of the semiconductor and this will result in some propagation loss. The displacement fields in the acoustic waves  $D_a^{(1)}$  and  $D_a^{(2)}$  penetrate into the semiconductor and generate displacement fields  $D_s^{(1)}$  and  $D_s^{(2)}$ .



CHART I. Flow graph of the various mechanisms present in a semiconductor convolver



at the surface of the semiconductor. Then, through the nonlinear coupling mechanism described in Section 2.1.1, these fields give rise to the convolution voltage  $V_{op}$  which is then transferred to a load and the output power  $P_e^{(3)}$  is detected.

We can define several figures of merit. The propagation loss due to the semiconductor is denoted by  $L_S$  and will be expressed in decibels. The terminal convolution efficiency is defined as

$$F_T = 10 \log \left( P_e^{(3)} / P_e^{(1)} \cdot P_e^{(2)} \right) . \quad (2.1-5)$$

The powers are expressed in mW and  $F_T$  in dBm. Finally the internal convolution efficiency is defined as<sup>23</sup>

$$\mathcal{M} = \frac{V_{op} w}{\left( 2 P_a^{(1)} P_a^{(2)} \right)^{1/2}} \quad (2.1-6)$$

where  $w$  is the acoustic beam width.  $\mathcal{M}$  does not take into account the transducer loss  $L_{TR}$ , the propagation loss  $L_S$  and the loss introduced by the output circuit  $R$ .  $\mathcal{M}$  is also normalized to the power densities in the acoustic waves. It will be seen that the following relation holds:

$$20 \log \mathcal{M} = A + F_T + L_S + L_{TR} + R \quad (2.1-7)$$

where

$$A = 10 \log (R_L w^2) + 30 ,$$

$R_L$  is the load resistance. All the previous coefficients can be

measured experimentally except  $\mathcal{M}$  which is computed with the help of Eq. (2.1-7).

Three of the mechanisms shown in Chart I are due to the semiconductor. They are the propagation loss, the linear coupling and the nonlinear coupling. They will depend very strongly on the carrier density and carrier mobility at the semiconductor surface. We shall describe these mechanisms in more detail later.

As the surface waves propagate under the semiconductor, the longitudinal component of their E-fields will interact with the carriers causing a current  $J$  to flow which depends on the semiconductor resistivity. There will be a power  $J \cdot E^*/2$  per unit volume, absorbed from the acoustic wave which will therefore be attenuated. This attenuation is directly related to the resistivity of the active part of the semiconductor, i.e., the region which is actually affected by the acoustic field. For very low resistivity, metal-like semiconductors, the loss will be small and it will increase with the resistivity. On the other end of the spectrum, a very high resistivity, dielectric-like semiconductor will also not attenuate the waves very strongly since there are very few carriers. The attenuation is maximum for an intermediate value of resistivity. In addition, the larger the airgap, the smaller the coupling to the semiconductor and hence the smaller the attenuation.

Each acoustic wave can be considered as a voltage source  $\phi_a$  coupled to the semiconductor through the airgap; the voltage  $\phi_a$  can be considered as being placed across the gap capacitance in

series with an equivalent semiconductor impedance. The displacement field at the surface of the semiconductor, which corresponds to the current flowing into it, depends on the value of these two impedances. The relation between the field at the semiconductor and the potential at the piezoelectric substrate defines the linear coupling between the piezoelectric and the semiconductor. The coupling strength will decrease as the impedance of the gap, i.e., its thickness, or that of the semiconductor increases; the latter occurs when the carrier density is reduced. In addition, if a thin charge sheet is present at the surface of the semiconductor, as is the case when a dc inversion layer is formed, this layer will tend to screen out the free carriers in the semiconductor bulk from the piezoelectric field. This will result in a reduction of the E-field inside the semiconductor and consequently a reduction of the linear coupling.

Finally, the convolution output voltage is a nonlinear function of the surface displacement fields. In Section 2.1.1, we derived an expression for the nonlinear coupling coefficient. If we write Eq. (2.1-1) in the form

$$\phi = - D_s^2 / 2qN_d \epsilon \quad (2.1-8)$$

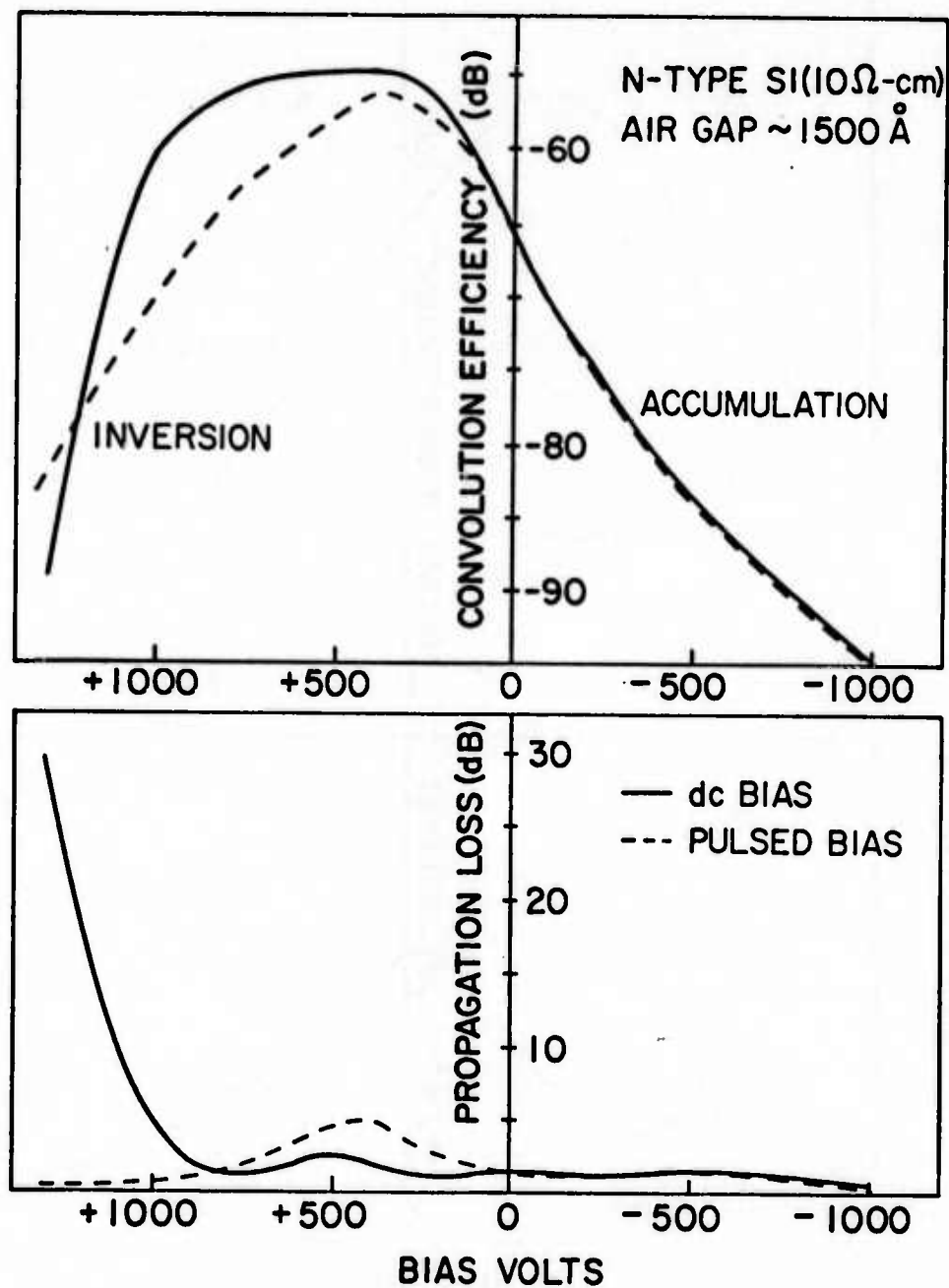
where  $D_s = \epsilon E_s$  is the displacement field at the surface, the nonlinear coefficient defined as  $B = \phi / D_s^2$ , is found to be  $B = -1/2qN_d \epsilon$ . In deriving these results, we reasoned that the rf field creates an rf depletion layer across which an rf potential is formed. When a dc depletion layer exists at the semiconductor surface, the rf field will be able to modulate fully the depletion layer

width and one can expect the above results to be exact. This will be proved rigorously in Section 2.2.2. On the other hand, when the semiconductor surface is at flat band (uniform concentration) or in accumulation (increased majority carrier concentration at the surface), there is no dc depletion layer and only half of each cycle of the acoustic field will deplete the semiconductor<sup>24</sup> and create a nonlinear potential. The other half-cycles will accumulate on the surface and, because of the  $1/N_d$  dependence of  $B$ , the nonlinearity associated with them will be negligible. One would therefore expect a reduced nonlinear coupling in these circumstances.

To check the previous qualitative assertions, we measured experimentally, the convolution efficiency  $F_T$  and the propagation loss  $L_S$  in two devices, as we varied the dc gate voltage  $V_G$  applied to the top electrode of the semiconductor (see Fig. 2.1-1). The results are plotted in Figs. 2.1-2(a) and (b) for p- and n-type silicon, respectively.

We first consider a p-type semiconductor convolver [Fig. 2.1-2(a)]. A positive biasing voltage will force holes toward the surface and hence will accumulate the surface of the semiconductor. On the contrary a negative bias will deplete the surface of its holes and, for a sufficiently high bias, an inversion layer of negative polarity will be formed. The flat band condition - uniform carrier distribution throughout the semiconductor - corresponds roughly to a zero bias.

For  $V_G = 0$ , the flat band condition is nearly satisfied. The surface resistivity of the silicon is relatively large (100  $\Omega$ -cm) and



(a)

FIG. 2.1-2--Experimental measurement of convolution efficiency ( $F_T$ ) and propagation loss ( $L_S$ ) vs bias voltage ( $V_G$ ), for  
 (a) an n-type Silicon on YZ  $\text{LiNbO}_3$  convolver. The full line curve corresponds to the dc bias measurements; the dashed line curve to the pulsed bias measurement.

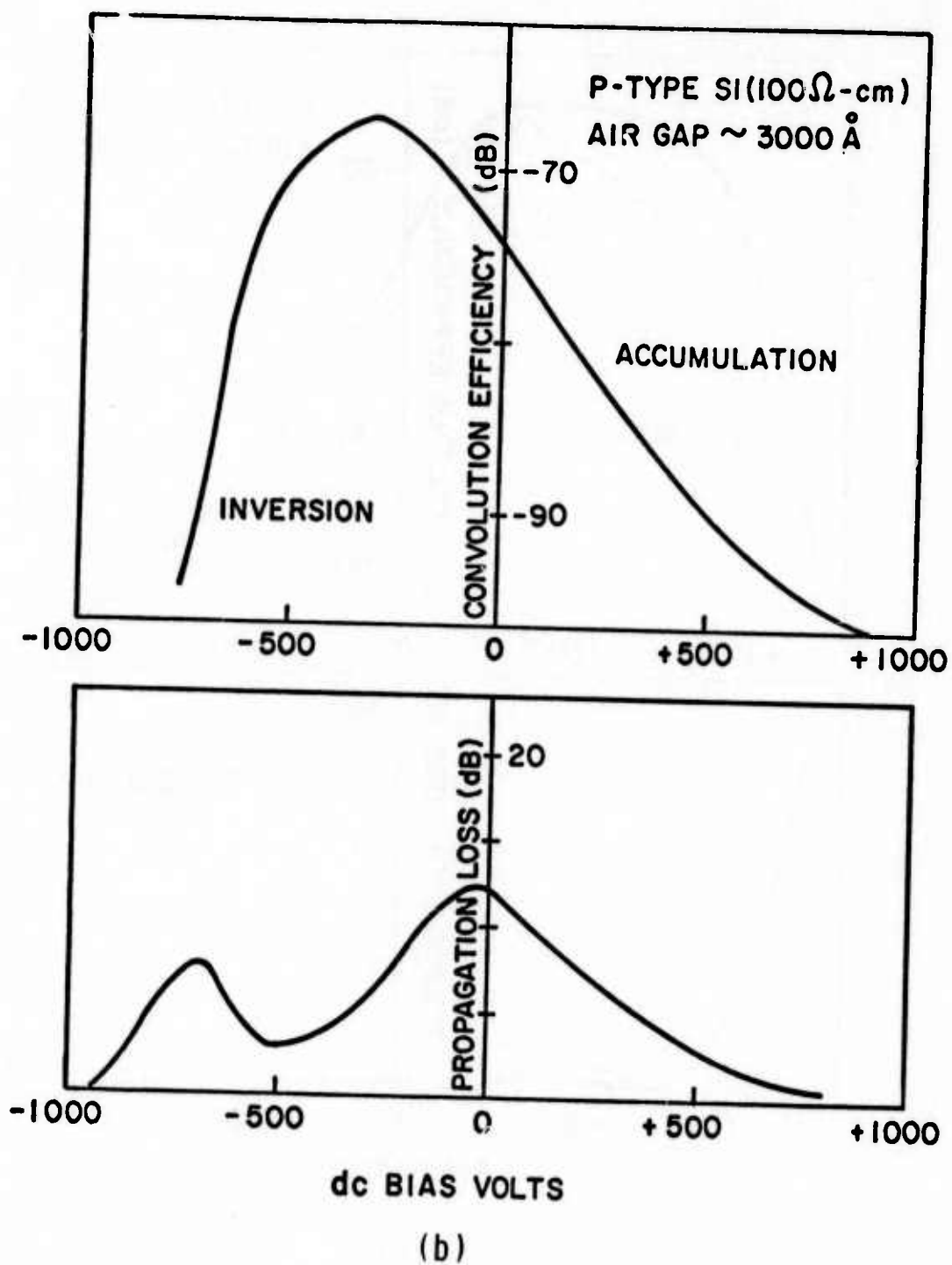


FIG. 2.1-2--Experimental measurement of convolution efficiency ( $F_T$ ) and propagation loss ( $L_S$ ) vs bias voltage ( $V_G$ ), for  
 (b) a p-type Silicon on YZ  $\text{LiNbO}_3$  convolver (dc bias only).



the propagation loss is rather high. As the bias is increased positively, the surface is driven into accumulation; thus the surface resistivity decreases sharply and so does the loss. For negative bias, a dc depletion layer is first formed, which acts as an extra insulating gap and reduces the coupling to the semiconductor and hence the loss. As the bias is made more negative, an inversion layer is generated and the surface resistivity decreases monotonically from almost infinity (insulating depletion layer) to zero. The loss exhibits a maximum as we predicted earlier.

As for the convolution efficiency, it decreases in the accumulation regime because of the increased carrier density. In depletion, the nonlinear mechanism becomes more efficient because the fields can now fully modulate the depletion layer; this shows up as an increase in convolution efficiency. Finally, for large negative bias voltages, the inversion layer charge shields the semiconductor and, at the same time, attenuates the waves, both of these effects resulting in a sharply reduced convolution efficiency.

The n-type semiconductor convolver behaves in a similar fashion. A negative voltage is now necessary for accumulation, and a positive one for depletion and inversion. The loss at flat band is low because of the lower resistivity of the silicon used here ( $10 \Omega\text{-cm}$ ). In inversion, the propagation loss increases, but the maximum of loss corresponds to a bias voltage outside the experimental range and it is not observed in this experiment.

A quantitative theory is required to explain the exact shape of the curves plotted in Figs. 2.1-2(a) and (b). It is developed in this chapter. It is necessary to take account of the charges trapped at the surface of the semiconductor.<sup>22,25-27</sup> According to the dc bias used, these traps are emptied or filled; this gives rise to a surface state screening effect so that higher voltages are necessary to obtain inversion than would be the case if no surface states were present.

In Fig. 2.1-2(b), we also show plots of the convolution efficiency and of the propagation loss with a pulsed bias.  $F_T$  and  $L_S$  are measured right after the bias has been applied. It is interesting to note that, in this case, when a pulsed bias is used, no charge can be exchanged with the traps because of their long time constants.<sup>25</sup> Very large fields are therefore present at the surface and if there exists a source of minority carriers at the surface of the semiconductor (like a  $p^+$  impurity center), a large number of minority carriers will immediately be injected. These carriers will be concentrated in a thin sheet of very low resistivity at the surface, under the influence of the applied field. The propagation loss  $L_S$  will therefore be very small and the convolution decreases because of the screening introduced by this minority charge sheet. This seems to be the mechanism which controls the n-type silicon convolver whose  $F_T$  and  $L_S$  are plotted in dashed lines in Fig. 2.1-2(b). Minority carrier sources may be created during the preparation of the samples. In particular, the samples are cut with a diamond saw; this may introduce  $p^+$  impurity centers at the extremities of the semiconductor.

Let us note however that other silicon samples did not show any sign of minority charge injection; the corresponding  $F_T$  remained at approximately a constant level when a positive bias was applied, as we would expect from a deep depletion theory without any inversion.

## 2.2 COMPLETE THEORY

### 2.2.1 General Discussion

In this section, we are concerned with a quantitative study of the linear and nonlinear coupling between Rayleigh surface wave field and carriers in a neighboring semiconductor. We shall evaluate the convolution efficiency  $\mathcal{M}$  and the propagation loss  $L_S$  for all surface conditions, i.e., all gate voltage  $V_G$ . The structure used is that of Fig. 2.1-1.

We assume that the properties of the Rayleigh wave propagating along the electrically free surface of the piezoelectric substrate is known.<sup>18</sup> Because of the weak coupling approximation, i.e., the fact that the electrical power is a fraction of the mechanical power in the piezoelectric, the acoustic wave propagation constant is only slightly affected by the electrical loading due to the semiconductor. This loading can be considered as a small perturbation of the unperturbed system composed of the bare delay line. This technique was developed by Kino-Reeder<sup>28</sup> and we use their results to solve the linear coupling problem in Section 2.2.3.

To evaluate the nonlinear coupling due to the space charge layer in the semiconductor, we assume thermal equilibrium, i.e., we assume

that the carriers follow the acoustic field variations. This is only a valid assumption for majority carrier concentrations, and particular attention must be paid to its use near intrinsic and inversion conditions. We shall discuss this further in Section 2.2.2.

In this study we compute the open circuit convolution output voltage denoted by  $V_{op}$  and we shall refer it to the acoustic powers on the delay line. This means that we do not take into account the transducer and output circuit loss. We write  $V_{op}$  as

$$V_{op} = \alpha V_0 .$$

$V_0$  is the open circuit output voltage computed assuming no propagation loss under the semiconductor; the loss  $L_s = -20 \log \alpha$  is the propagation loss due to the presence of the semiconductor. If a normal surface displacement field  $D_s$  is created at the surface of the semiconductor, we shall see that a potential  $\phi_s$  is generated across the device, which has the following form:

$$\phi_s = AD_s + BD_s^2 .$$

We now assume two oppositely traveling waves are present with fields  $D_s^{(1)}$  and  $D_s^{(2)}$  at the surface of the semiconductor, with acoustic potentials at the surface  $\phi_a^{(1)}$  and  $\phi_a^{(2)}$  and powers  $P_a^{(1)}$  and  $P_a^{(2)}$ . The "nonlinear convolution" voltage generated at the sum frequency of the input frequency is

$$V_0 = BD_s^{(1)} D_s^{(2)} .$$

It can be rewritten as

$$V_0 = B \left( \frac{D_s^{(1)} D_s^{(2)}}{\phi_a^{(1)} \phi_a^{(2)}} \right) \cdot \left( \frac{\phi_a^{(1)} \phi_a^{(2)}}{\sqrt{P_a^{(1)} P_a^{(2)}}} \right) \cdot \sqrt{P_a^{(1)} P_a^{(2)}} \quad (2.2-1)$$

-- B is the nonlinear coupling coefficient; it is derived in Section 2.2.2 by integration of Poisson's equation.

-- The term

$$\frac{D_s^{(1)} D_s^{(2)}}{\phi_a^{(1)} \phi_a^{(2)}} = \left( \frac{D_s^{(1)}}{\phi_a^{(1)}} \right)^2$$

is the linear gap coupling; it is derived in Section 2.2.3 by use of an equivalent circuit concept.

-- The term

$$\frac{\phi_a^{(1)} \phi_a^{(2)}}{\sqrt{P_a^{(1)} P_a^{(2)}}} = 2Z_a$$

is twice the acoustic impedance of the piezoelectric used. This concept is reviewed in Section 2.2.4.

The loss term  $L_s$  is a linear term and hence is obtained in Section 2.2.3.

## 2.2.2 The Nonlinear Coupling

We define the potential  $\phi$  as zero in the bulk of the semiconductor;  $\phi$  is therefore measured from the intrinsic Fermi level of the conduction band level in the bulk. We consider an n-type

semiconductor with a donor density  $N_d$ . At room temperature, most of the donors are ionized, and the bulk electron concentration is  $n_b \approx N_d$ ; from the mass action law,<sup>22</sup> the hole concentration in the bulk is given by  $p_b = n_i^2/n_b \approx n_i^2/N_d$  where  $n_i$  is the intrinsic concentration. If we assume non-degenerate conditions and thermal equilibrium, Boltzmann statistics apply and the carrier concentrations are the following functions of the potential  $\phi$ :

$$n = N_d \exp (q\phi/kT)$$

$$p = n_i^2/N_d \exp (-q\phi/kT) .$$

We then solve the relation between  $D_s$  and  $\phi_s$  at the semiconductor surface by using standard MIS diode theory, and perturbing the dc solution so as to determine  $\phi_s$  to second order in the perturbing displacement field  $D_s$ . The potential as a function of  $y$  may be determined by writing the one-dimensional Poisson's equation

$$d^2\phi/dy^2 = -\rho/\epsilon$$

where  $\rho$  is the space charge density given by

$$\rho = q(N_d - n + p) .$$

Poisson's equation can therefore be written as

$$\frac{d^2\phi}{dy^2} = \frac{qN_d}{\epsilon} \left[ \exp \left( \frac{q\phi}{kT} \right) - 1 \right] - \frac{qn_i^2}{\epsilon N_d} \left[ \exp \left( -\frac{q\phi}{kT} \right) - 1 \right] \quad (2.2-2)$$

When the surface is well depleted, the potential is strongly negative over the extent of the depletion layer and the charge density in the depletion layer is essentially  $N_d$ . In this case, the depletion layer assumption can be used and one can define an equivalent depletion width<sup>27</sup> of length  $l$  over which the semiconductor is fully depleted. Equation (2.2-2) reduces to

$$\begin{aligned} d^2\phi/dy^2 &= -qN_d/\epsilon & \text{for } 0 \leq y \leq l \\ \phi &= 0 & \text{for } y \geq l \end{aligned}$$

By integration, we can evaluate the surface potential  $\phi_s = \phi(y=0)$  and the surface displacement field  $D_s = -\epsilon \frac{d\phi}{dy}(y=0)$ ,

$$\phi_s = -qN_d l^2 / 2\epsilon \quad \text{and} \quad D_s = -qN_d l$$

Elimination of  $l$  yields the relation

$$\phi = -D_s^2 / 2qN_d\epsilon$$

which is the simple result used previously in Section 2.1.1.

In general, we integrate Eq. (2.2-2) once by multiplying by  $d\phi/dy$ ; we find at the surface of the semiconductor

$$D_s^2 = N_d kT \epsilon F^2(q\phi_s/kT) \quad (2.2-3)$$

where the function  $F$  is defined<sup>29</sup> as

$$F(v) = \sqrt{2} \left( \exp v - v - 1 + \frac{n_i^2}{N_d^2} \left[ \exp(-v) + v - 1 \right] \right)^{1/2}, \quad (2.2-4)$$

where  $v$  is a dummy variable.



If a dc bias  $V_G$  is applied to the semiconductor, we write the potential and the displacement field as

$$\phi_s = \phi_{s0} + \phi_{s1}$$

$$D_s = D_{s0} + D_{s1}$$

respectively, where the subscripts 0 and 1 refer to dc and rf terms, respectively.  $\phi_s$  and  $D_s$  must satisfy Eq. (2.2-3) and a general solution for  $\phi_s$  can be written as a series expansion in the successive powers of  $D_s$

$$\phi_s = \phi_{s0} + A(D_s - D_{s0}) + B(D_s - D_{s0})^2 + \dots \quad (2.2-5)$$

The convolution output voltage corresponds to the second order non-linear term; we therefore solve Eq. (2.2-3) for  $\phi_s$  to second order in  $D_s$ . It follows that

$$A = 2D_{s0} \left[ a(\exp u_0 - 1) - b(\exp(-u_0) - 1) \right]^{-1} \quad (2.2-6)$$

$$B = \left[ a(\exp u_0 - 1) - b(\exp(-u_0) - 1) \right]^{-1} \times \left\{ 1 - \frac{\frac{2q}{kT} (a \exp u_0 + b \exp(-u_0))}{\left[ a(\exp(u_0) - 1) - b(\exp(-u_0) - 1) \right]^2} D_{s0}^2 \right\}, \quad (2.2-7)$$

where

$$u_0 = q\phi_{s0}/kT ; \quad a = 2qN_d\epsilon ; \quad b = 2qn_i^2\epsilon/N_d \quad (2.2-8)$$

$$D_{s0} = \sqrt{N_d kT\epsilon} \cdot F(q\phi_{s0}/kT) \cdot \text{sgn}(\phi_{s0})$$

For an n-type semiconductor and flat band condition,  $D_{s0} = 0$  ,  
 $A = \lambda_d/\epsilon$  and  $B = -1/6qN_d\epsilon$  . When the surface is well depleted  
 $A = d/\epsilon$  ,  $B = -1/2qN_d\epsilon$  where  $d$  is the length of the depletion  
layer and  $\lambda_d$  the Debye length. This is again the result derived  
in Section 2.1.1. When the surface is strongly accumulated  $A \rightarrow 0$   
and  $B \rightarrow 0$  .

So far we have assumed thermal equilibrium, i.e., equilibrium,  
at all times, between the carriers and the total electric field. The  
total field here is the superposition of the dc biasing field and the  
rf acoustic field. To stay in equilibrium, the carriers must be  
supplied at a rate higher than the rf frequency. For a frequency  
of 100 MHz, the time constant associated with this transport of  
carriers must therefore be smaller than 10 nsec. In the accumulation  
and depletion regimes, the principal carriers are of the majority type  
and the time constant involved is of the order of 10 psec;<sup>22</sup> so we  
can use the thermal equilibrium assumption. On the contrary, in the  
case of a dc inversion layer being formed at the surface of the semi-  
conductor, the supply of minority carriers from the bulk is very slow,  
because of the very long generation-recombination times involved.  
These carriers will not be able to follow the normal component of the  
acoustic E-field, which is the cause of the nonlinear potential. The  
only source of nonlinear coupling will be the depletion layer located  
behind the inversion layer and  $B$  will remain equal to  $-1/2qN_d\epsilon$  .  
This is equivalent to the well known result for the behavior of the  
capacity of MOS diodes with frequency: the high frequency capacitance

remains equal to the depletion capacitance before inversion.<sup>22,25,26</sup>

A complete plot of  $-BqN_d\epsilon$  vs  $q\phi_{s0}/kT$  is given in Fig. 2.2-1. The low frequency curves have been drawn assuming thermal equilibrium, but as we have just discussed, the high frequency curve should be used in the inversion regime.

Let us note, however, that minority carriers can move quite easily along the surface of the semiconductor. The surface mobility is typically half of the bulk mobility.<sup>25</sup> Hence we can assume that the minority carriers are in equilibrium with the tangential component of the electric field. This coupling between tangential field and carriers is responsible for the propagation loss and the so-called longitudinal convolution effect.<sup>30,3</sup> The former effect will be discussed in Section 2.2.3.

Equation (2.2-8) allows us to relate the bias voltage  $V_G$  to the dc surface potential  $\phi_{s0}$ . Because of the low capacitance of the piezoelectric material (thickness  $y_p = 1$  to  $3$  mm, and for YZ  $\text{LiNbO}_3$  the permittivity is  $\epsilon_{yy} \sim 70 \epsilon_0$ ) compared to the airgap capacitance (height  $h = 0.1$  to  $0.5$   $\mu\text{m}$ , permittivity  $\epsilon_0$ ), all the voltage is dropped across the piezoelectric. If  $D_{s0}$  is the dc displacement field in the piezoelectric material, we can write

$$V_G = D_{s0} y_p / \epsilon_{yy} \quad (2.2-9)$$

and from Eq. (2.2-8),  $\phi_{s0}$  is given by the relation

$$V_G = \frac{y_p}{\epsilon_{yy}} \sqrt{N_d k T \epsilon} \cdot F(q\phi_{s0}/kT) \cdot \text{sgn}(\phi_{s0}) \quad (2.2-10)$$

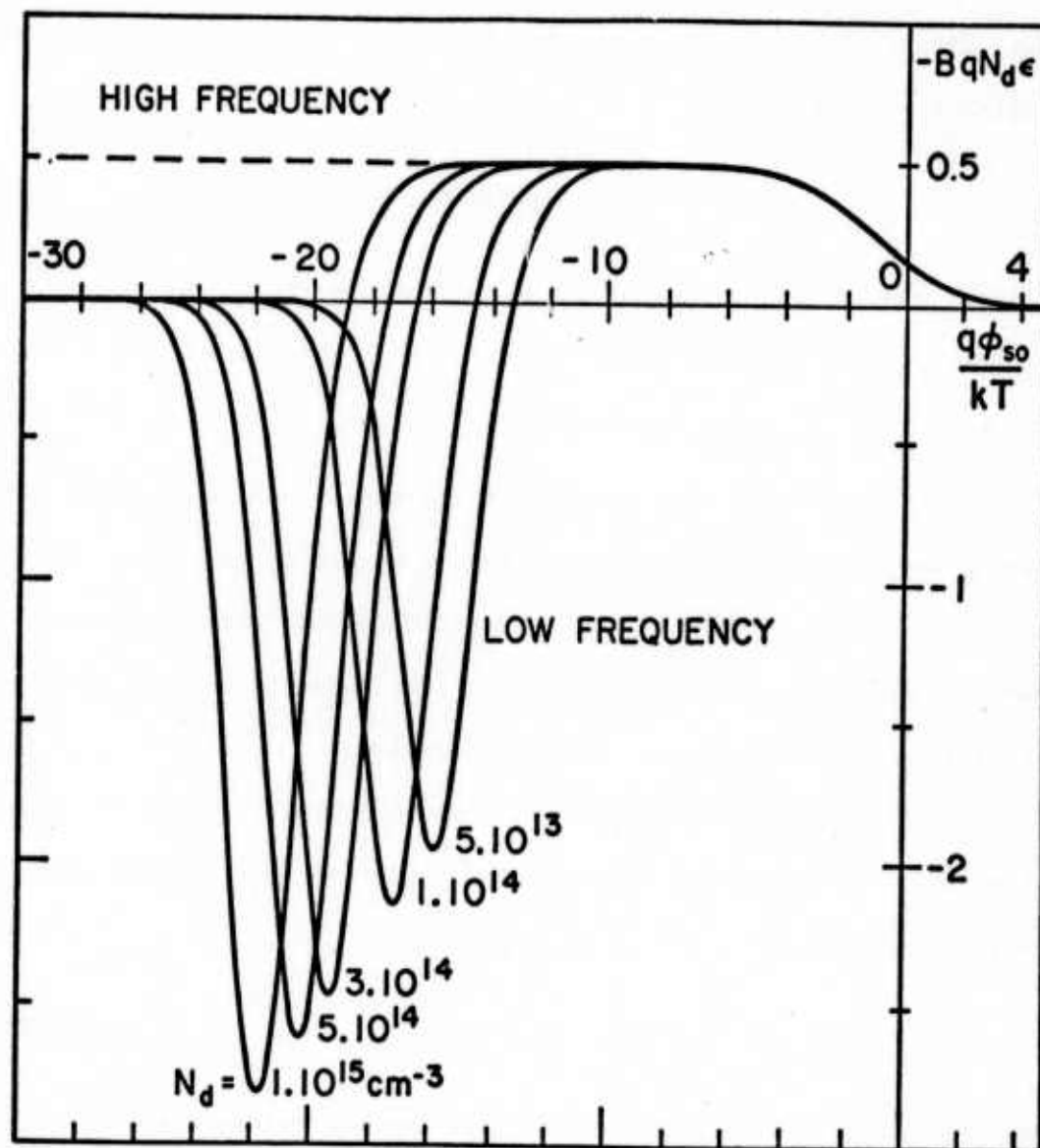


FIG. 2.2-1--Plot of the nonlinear coupling coefficient  $B$  vs the dc surface potential.

### 2.2.3 Equivalent Circuit

To relate the first order term in  $\phi_s$  to the value of  $D_s$ , we use an equivalent electrical circuit in which "current" is displacement current  $I = j\omega D$  and "potential" is electric potential  $\phi$ . The admittance is then

$$Y = j\omega D / \phi .$$

We shall make extensive use of the Kino-Reeder perturbation theory<sup>28</sup> for the Rayleigh wave amplifier to derive this circuit.

#### Flat band conditions.

Following Kino-Reeder, we compute the admittance  $Y^-$  at the surface of the semiconductor in two different ways: 1) looking at the piezoelectric through the airgap thus yielding the "piezoelectric coupling equation", 2) looking into the semiconductor assumed semi-infinite, this yields the "electronic equation".

To derive the piezoelectric coupling equation, we write the total rf potential as the sum of the acoustic potential  $\phi_a$  and the space charge potential  $\phi_s$

$$\phi = \phi_a + \phi_s . \quad (2.2-11)$$

For  $y \leq h$ ,  $\phi_s$  can be computed by replacing the volume charge in the semiconductor by a fictitious charge  $\rho'_s$  at  $y = h$ . Solving Poisson's equation in the layered system so formed and matching the boundary conditions at  $y = 0$  and  $y = h$ , it is shown in Eq. 18 of

reference 28 that

$$\phi_s(h) = (\rho'_s / \beta \epsilon_0) M(\beta h) \quad (2.2-12)$$

where

$$M(\beta h) = \frac{\epsilon_0 + \epsilon_p \tanh(\beta h)}{(\epsilon_0 + \epsilon_p)(1 + \tanh(\beta h))} \quad (2.2-13)$$

$\beta$  is the propagation constant of the wave,  $\epsilon_p = (\epsilon_{yy}\epsilon_{zz} - \epsilon_{yz}^2)^{1/2}$  is the effective permittivity of the piezoelectric material in the  $y$  direction.

In the normal mode theory of Auld-Kino,<sup>31</sup> the acoustic potential  $\phi_a$  is the term associated with the excitation of the principal acoustic mode, the Rayleigh surface wave. It is found to be given by the relation

$$\phi_a(h) = - \frac{\omega \beta \rho'_s w Z_a(\beta h)}{\beta'^2 - \beta^2}, \quad (2.2-14)$$

where  $\beta'$  is the perturbed propagation constant,  $\beta$  the unperturbed one;  $w$  is the width of the acoustic beam,  $Z_a(\beta h)$  the acoustic impedance at the surface of the semiconductor. With the help of the boundary conditions at  $y = h$ , the admittance on the lower side of the fictitious charge is

$$Y^- = j\beta\omega\epsilon_0 - j\omega\rho'_s/\phi(h) \quad (2.2-15)$$

The piezoelectric coupling equation follows from Eqs. (2.2-11), (2.2-12), (2.2-14), and (2.2-15):

$$\frac{1}{Y^- - Y_0} = j \left[ \frac{M(\beta h)}{\beta \omega \epsilon_0} - \frac{\beta w Z_a(\beta h)}{\beta'^2 - \beta^2} \right] \quad (2.2-16)$$

where

$$Y_0 = j\beta \omega \epsilon_0 .$$

The electronic equation is obtained by writing the current, continuity and Poisson's equations in the semiconductor.<sup>28</sup> The general solution is the superposition of two waves: the Laplacian wave which corresponds to a zero rf charge density and has a variation  $\exp(-j\beta z \pm \beta y)$  and the diffusion wave which propagates as  $\exp(-j\beta z \pm \gamma y)$ . Assuming the semiconductor is semi-infinite, it can be shown that the admittance at the surface  $y = h$  is

$$Y^- = Y_s + \frac{\omega \omega_c \epsilon \beta (\gamma - \beta)}{\gamma \omega - j \omega_c \beta} , \quad (2.2-17)$$

where  $Y_s = j\beta \omega \epsilon$  is the admittance of the free semiconductor,  $\omega_c = \mu q N_d / \epsilon$  is the dielectric relaxation frequency and  $\mu$  the mobility of the majority carriers. We make the further approximation that  $\omega \ll (\omega_c \omega_D)^{1/2}$  or, written in another way,  $\beta \ll 1/\lambda_d$ , where  $\omega_D = v^2 / (kT/q) \mu$  is the diffusion frequency. This restricts the validity range of the present theory to approximately  $f \leq 500$  MHz and  $N_d \geq 10^{14} \text{ cm}^{-3}$ . This being the range of practical interest, the



assumption is sound and it will make the study simpler and the equivalent circuit easier to picture. The attenuation constant  $\gamma$  or the e-folding distance of the rf charge density, reduces to

$$\gamma \approx \frac{(\omega_c \omega_D)^{1/2}}{v} = \lambda_d^{-1}, \quad (2.2-18)$$

where  $\lambda_s$  is the Debye length. The electronic equation becomes

$$Y^- - Y_s = - \frac{\omega_c \beta \epsilon}{-1 + j(\omega_c / \omega_D)^{1/2}} \quad (2.2-19)$$

With the use of Eqs. (2.2-17) and (2.2-19), we can now draw the equivalent circuit shown in Fig. 2.2-2 where we ignore, for the moment, the two components  $Y_{\text{inversion}}$  and  $C_{\text{depletion}}$ . The acoustic properties of the piezoelectric substrate are modeled by an inductance  $\mathcal{L}_a$  across which the potential developed is  $\phi_a$ . The gap coupling is represented by the capacitance  $C_{\text{gap}}$  and the bulk of the semiconductor contains a lossy term  $R_b$  and a capacitive term  $C_b$ . The respective expressions are given below:

$$\mathcal{L}_a = \frac{1}{\omega} \frac{\beta w Z_a (\beta h)}{\beta'^2 - \beta^2}$$

$$C_{\text{gap}} = \beta \epsilon_0 / M(\beta h)$$

$$R_b = (\omega_c \epsilon \beta)^{-1}$$

$$C_b = (\omega_c \omega_D)^{1/2} \beta \epsilon / \omega = \epsilon / \lambda_d$$

(2.2-20)

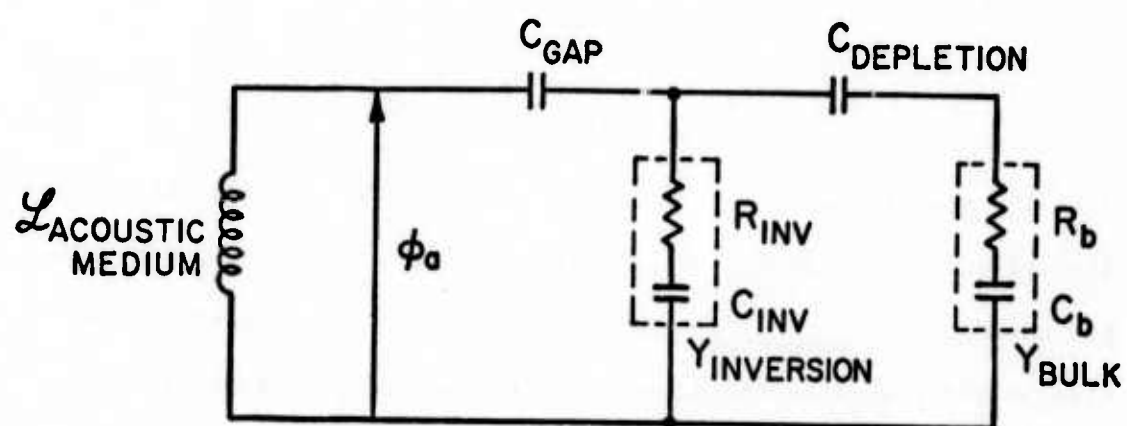


FIG. 2.2-2--Equivalent circuit used in the evaluation of linear coupling and loss.

It will be noted that thanks to the assumption  $\omega \ll (\omega_c \omega_D)^{1/2}$  we can ignore the effect of the terms  $Y_0$  and  $Y_s$  which should appear as capacitors in parallel with bulk admittances. Let us also note that for the semiconductors of interest  $\omega_c \ll \omega_D$  and hence the resistive term is small,

$$R_b \ll 1/(C_b \omega) ,$$

thus inferring that the propagation loss due to the presence of the semiconductor is small.

The "linear gap coupling" term  $D_s/\phi_a$  is now straightforward to evaluate

$$D_s/\phi_a = \frac{\beta \epsilon_0}{M(\beta h)} \left[ 1 + \frac{\beta \epsilon_0 \lambda_d}{\epsilon M(\beta h)} + j \frac{\omega \epsilon_0}{\omega_c \epsilon M(\beta h)} \right]^{-1} . \quad (2.2-21)$$

The last bracket in Eq. (2.2-21) is equal to unity to within 10% or less for 10 to 100  $\Omega$ -cm silicon.

#### Accumulation conditions

The majority carrier concentration is larger near the surface than the bulk value  $(N_d)$ . The density of this accumulation layer varies essentially exponentially with distance and can be calculated by integration of Eq. (2.2-2); a useful measure of the extent of the accumulation layer is the distance, from the surface, of the center of mass of the excess carrier distribution. This distance, called  $L_c$ , is found<sup>29</sup> to be equal to the bulk Debye length  $\lambda_d$  for weak accumulation and is a slowly decreasing function of the dc surface potential. Experimentally,

the strongest accumulation we have been able to achieve corresponds to  $q\phi_{s0}/kT = 5$ , when  $L_c$  has decreased to  $0.3 \lambda_d$ . The total excess charge can also be computed,<sup>29</sup> and we can thus define an equivalent uniform surface concentration  $N_{accn}$  as follows:

$$N_{accn} = N_d + \Delta N / 2L_c, \quad (2.2-22)$$

where  $\Delta N$  is the total excess charge per unit area. The gap coupling is still given by Eq. (2.2-21) where  $\lambda_d$  is now computed for a concentration  $N_{accn}$ . Only the correction term is affected and it becomes even smaller.

#### Depletion conditions.

We use the simple depletion layer approximation. This introduces an extra capacitance  $C_{depletion}$  in series with  $C_{gap}$  where

$$C_{depletion} = \epsilon / l. \quad (2.2-23)$$

$l = (2\epsilon\phi_{s0}/qN_d)^{1/2}$  is the depletion length. In other words, the air-gap  $h$  has now increased to  $h + l\epsilon_0/\epsilon$  and all previous results are directly applicable.

#### Inversion.

The depletion width continually increases until inversion sets in. This occurs when  $\phi_{s0}$  becomes approximately twice the bulk potential  $\phi_B$ . For larger  $\phi_{s0}$  the depletion width will level off and any increase of surface potential will correspond to an inversion of the surface. The maximum depletion width is given by the expression

$$l_{max} = (4\epsilon\phi_B/qN_d)^{1/2} = \lambda_d (4q\phi_B/kT)^{1/2}.$$

For 10 to 100  $\Omega$ -cm silicon,  $q\phi_F/kT$  is 10 to 11, hence the maximum depletion width is approximately  $6.5 \lambda_d$ . The inversion extends into the semiconductor. To keep the calculations simple but nevertheless account for the charge spreading, we model the inversion layer as an infinitesimally thin charge sheet located at its true center of mass, a distance  $L_{ci}$  away from the surface. This decreases the effective depletion length by  $L_{ci}$  and increases the airgap by  $L_{ci}\epsilon_0/\epsilon$ . It is necessary to take into account the spreading of the inversion charge because we are concerned with weak inversion and with calculating the capacity of the depletion layer as accurately as possible. The effect of the finite thickness of the inversion layer  $L_{ci}$  is not negligible since for weak inversion<sup>29</sup>  $L_{ci} \approx 3\lambda_d$  and for the highest density inversion layer that we have generated experimentally,  $L_{ci}$  has a value which is still of the order of  $\lambda_d$ . The total inversion charge per unit area is given by the relation

$$\Delta N_{is} = N_d \lambda_d g^+ \quad (2.2-24)$$

This relation defines the parameter  $g^+$ . And as in the case of accumulation,  $g^+$  and  $L_{ci}$  are functions of  $\phi_{s0}$  and they have been plotted by Many, et al.<sup>29</sup> Referring again to Kino-Reeder,<sup>28</sup> the admittance of a sheet of charge is

$$Y_{inv} = \frac{\omega_{ci} \epsilon \beta^2 \delta}{1 - j\omega/\omega_{Di}} \quad (2.2-25)$$

where  $\omega_{ci}$  and  $\omega_{Di}$  are the dielectric relaxation and diffusion frequencies, respectively, for minority carriers.  $\delta$  is the width of the

equivalent charge sheet. From Eqs. (2.2-24) and (2.2-25), we obtain the admittance of the inversion layer as

$$Y_{inv} = \frac{\mu_i q N_d \lambda_d \beta^2 g^+}{1 - j\omega/\omega_{Di}} \quad (2.2-26)$$

and we can now draw the full equivalent circuit. It is shown in Fig. 2.2-2. To first order,  $Y_{bulk}$  is mainly capacitive and  $Y_{inversion}$  mainly resistive introducing some extra loss and hence reducing the current  $I$  flowing into the semiconductor, therefore reducing the convolution output. This reduction occurs mainly in the inversion regime; it is therefore of interest to evaluate the ratio of  $I$  in the presence of an inversion (characterized by  $g^+$ ) to  $I$  at maximum depletion ( $g^+ = 0$ ):

$$\mathcal{R} = \left[ \frac{I(g^+)}{I(g^+=0)} \right]^2 = \left[ \frac{\phi_a/D_s(g^+)}{\phi_a/D_d(g^+=0)} \right]^2 \quad (2.2-27)$$

The "reduction factor"  $\mathcal{R}$  is straightforward to evaluate using the equivalent circuit, and the plots for  $L_{ci}$  and  $g^+$ . It is found that  $\mathcal{R}$  is a monotonically decreasing function of  $g^+$  and for  $g^+ \sim 10$ , which corresponds to a medium inversion,  $\mathcal{R}$  is of the order of  $10^{-2}$ . Plots of  $\mathcal{R}$  are given in Fig. 2.2-3 in the two particular cases summarized in Table 2.1.

TABLE 2.1

Piezoelectric	YZ LiNbO <sub>3</sub> $\epsilon_p/\epsilon_0 = 50.2$	
Semiconductor	Silicon length = 2 cm	
	$N = 7.10^{20} \text{ m}^{-3}$ $\epsilon/\epsilon_0 = 11.7$ $\mu_p = 0.025 \text{ m}^2/\text{Vs}$ $\mu_n = 0.07 \text{ m}^2/\text{Vs}$	
	n-type	p-type
Airgap	1500 Å	3000 Å

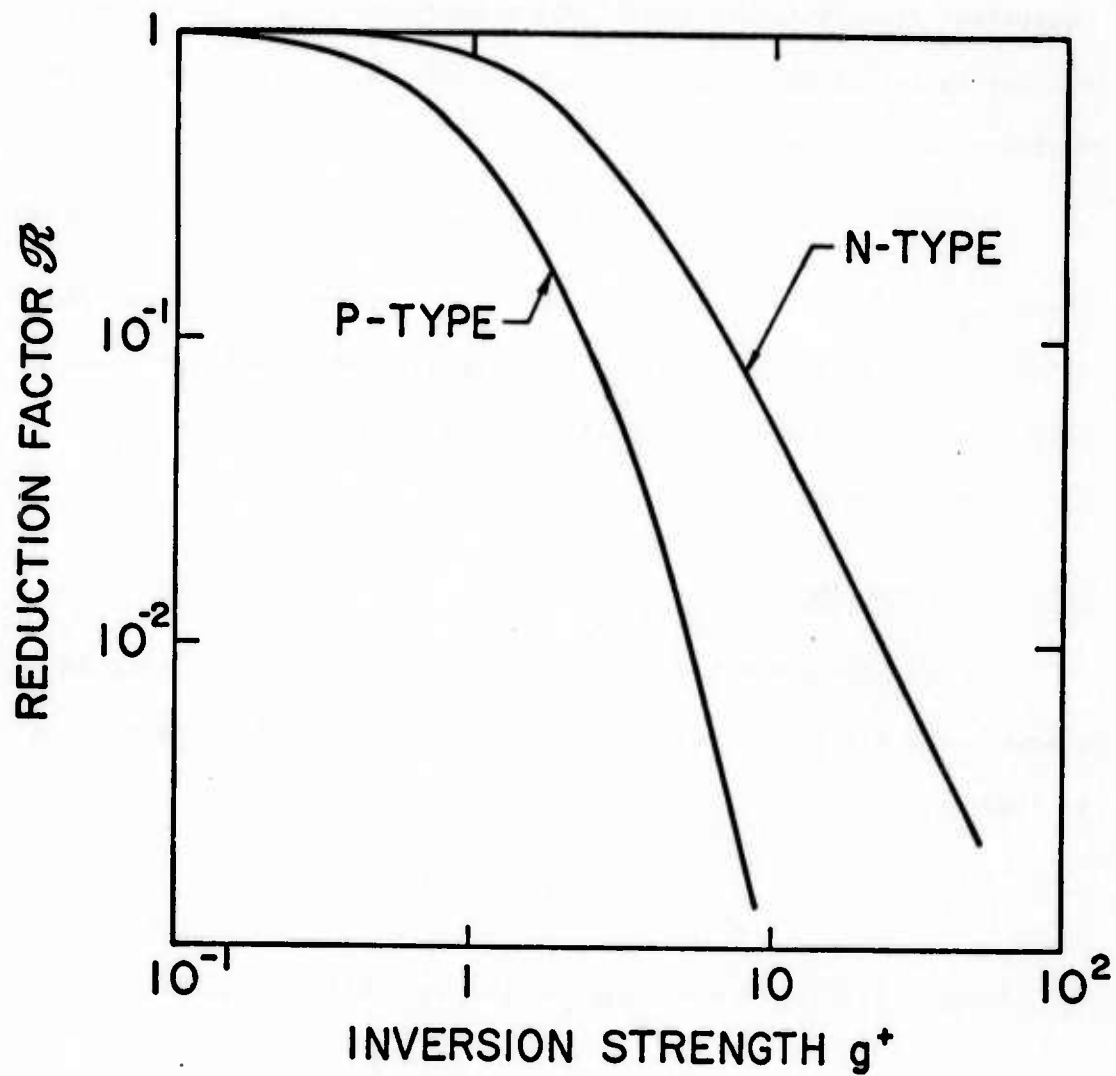


FIG. 2.2-3--Reduction factor  $\mathcal{R}$  vs inversion strength  $g^+$  for the two cases given in Table 2.1.



#### Propagation loss due to the semiconductor.

The dispersion relation for the semiconductor-airgap-piezoelectric system is obtained by writing the condition for total impedance in the equivalent circuit to be zero. In the expression for  $Z_a$  it is convenient to assume that the perturbed acoustic wave has a propagation constant of the form

$$j\beta' = j\beta + \alpha_r + j\beta_r \quad (2.2-28)$$

where  $\alpha_r$  and  $\beta_r$  are, respectively, the incremental loss and phase delay constants for the system. Equating real and imaginary parts to zero in the dispersion relation yields the propagation loss  $\alpha_r$  (in Nepers per meter).

#### 2.2.4 Acoustic Impedance

The acoustic potential at the surface of the piezoelectric is related to the acoustic power  $P_a$  through the acoustic impedance as follows:

$$\phi_a(0) = \left[ 2P_a Z_a(0) \right]^{1/2} . \quad (2.2-29)$$

$Z_a$  is given by the perturbation formula Eq. (83) in reference 28:

$$Z_a(0) = \frac{2}{\omega(\epsilon_p + \epsilon_0)} \left| \frac{\Delta v(0)}{v} \right| . \quad (2.2-30)$$

$|\Delta v(0)/v|$  is the relative surface wave velocity change when a shorting plane is introduced at  $y = 0$ . Since the rf electric field associated with the surface wave must vary as  $\exp(-\beta y)$  in the region  $y > 0$ , it

follows that

$$Z_a(\beta h) = Z_a(0) \exp(-2\beta h) \quad . \quad (2.2-31)$$

## 2.3 THEORETICAL AND EXPERIMENTAL RESULTS

### 2.3.1 Flat Band Conditions

We first examine the flat band results since they will provide simple design curves to select the airgap thickness and the conductivity of the semiconductor.

The convolution efficiency can be normalized, thus defining the  $\mathcal{M}$ -value,<sup>23</sup> as  $\mathcal{M} = V_0 w \left( 2P_a^{(1)} P_a^{(2)} \right)^{-1/2}$ . For flat band conditions, the full expression is derived from Eqs. (2.2-1), (2.2-7), (2.2-21), (2.2-30), and (2.2-31). We obtain for  $\mathcal{M}$ ,

$$\mathcal{M} = \frac{\sqrt{2} \epsilon_0}{3qN_d \epsilon(\epsilon_p + \epsilon_0)} \left| \frac{\Delta v(0)}{v} \right| \frac{\omega}{v^2} \frac{\exp(-2\beta h)}{M^2(\beta h)} \left| 1 + \frac{\beta \epsilon_0 \lambda_d}{\epsilon M(\beta h)} + j \frac{\omega \epsilon_0}{\omega_c \epsilon M(\beta h)} \right|^{-2} \quad (2.3.1)$$

and for the attenuation constant  $\alpha_r$ :

$$\alpha_r = \frac{\mu q N_d}{v} \left| \frac{\Delta v}{v} \right| \frac{\exp(-2\beta h)}{\epsilon_0 + \epsilon_p} \left[ 1 + \left( \sqrt{\frac{\omega_c}{\omega_D}} + M(\beta h) \frac{\omega_c \epsilon}{\omega \epsilon_0} \right)^2 \right]^{-1} \quad . \quad (2.3-2)$$

Recalling the assumption  $\omega \ll (\omega_c \omega_D)^{1/2}$  we can greatly simplify the expression for  $\alpha_r$  and write it in the form

$$\alpha_r \approx \frac{\omega^2}{\mu q N_d} \frac{\Delta v}{v^2} \frac{\epsilon_0^2}{\epsilon(\epsilon_p + \epsilon_0)} M^{-2}(\beta h) \quad . \quad (2.3-3)$$

The loss expressed in dB in a length  $L$  is

$$L_S = 8.6 \alpha_r L . \quad (2.3-4)$$

The loss is seen to be proportional to the resistivity of the semiconductor. As mentioned earlier in Section 2.2.3, the last bracket in the expression for  $\mathcal{M}$  is a correction term and, in first approximation, we may neglect it. So with the help of Eq. (2.3-3),  $\mathcal{M}$  can be written simply as follows:

$$\mathcal{M} \approx \frac{\sqrt{2}}{3} \frac{\mu}{\omega v \epsilon_0} \alpha_r . \quad (2.3-5)$$

If we now include the propagation loss term, we obtain the open voltage  $V_{op}$

$$V_{op} \propto \mathcal{M} \exp(-\alpha_r l/2) = \mathcal{M} 10^{-L_S/20} . \quad (2.3-6)$$

When the approximations leading to Eqs. (2.3-3) and (2.3-5) are valid, we obtain the following important result, first given by Otto: For a given semiconductor and piezoelectric material, the convolution is optimum when the propagation loss introduced by the semiconductor is 1 Neper or 8.6 dB. In Fig. 2.3-1(a) and (b), we show plots of the loss  $L_S$  and the  $\mathcal{M}$ -values  $\mathcal{M}$  and  $\mathcal{M} 10^{-L_S/20}$  vs conductivity for airgaps ranging from 0.1  $\mu\text{m}$  to 1.0  $\mu\text{m}$ . The expressions given by Eqs. (2.3-1) and (2.3-2) are used. Both n- and p-type silicons are considered and the operating frequency is 100 MHz. The silicon length is  $L = 2$  cm and the piezoelectric material is YZ  $\text{LiNbO}_3$ .

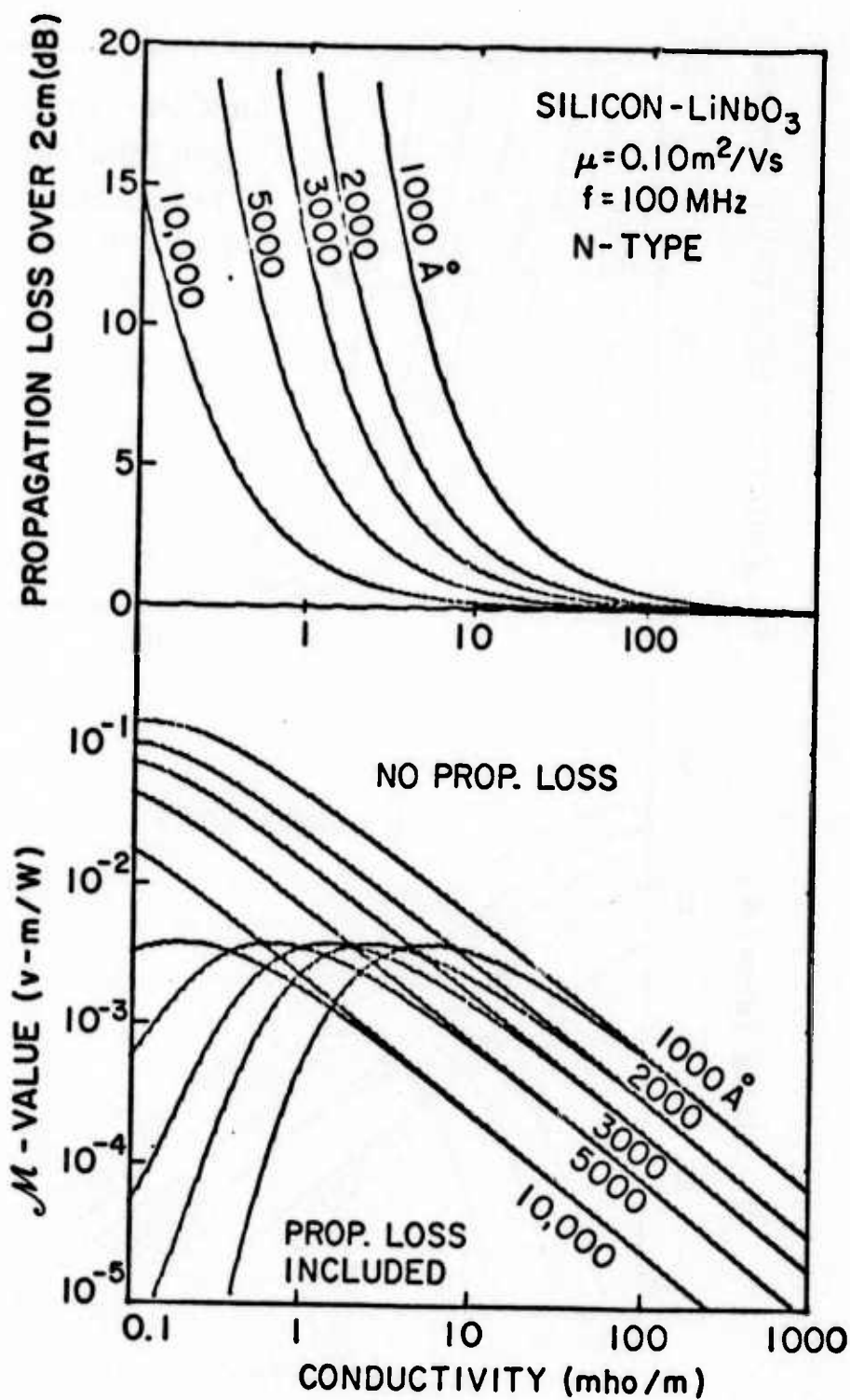


FIG. 2.3-1--Propagation loss and  $M$ -values vs conductivity for various airgaps.

(a) n-type silicon.

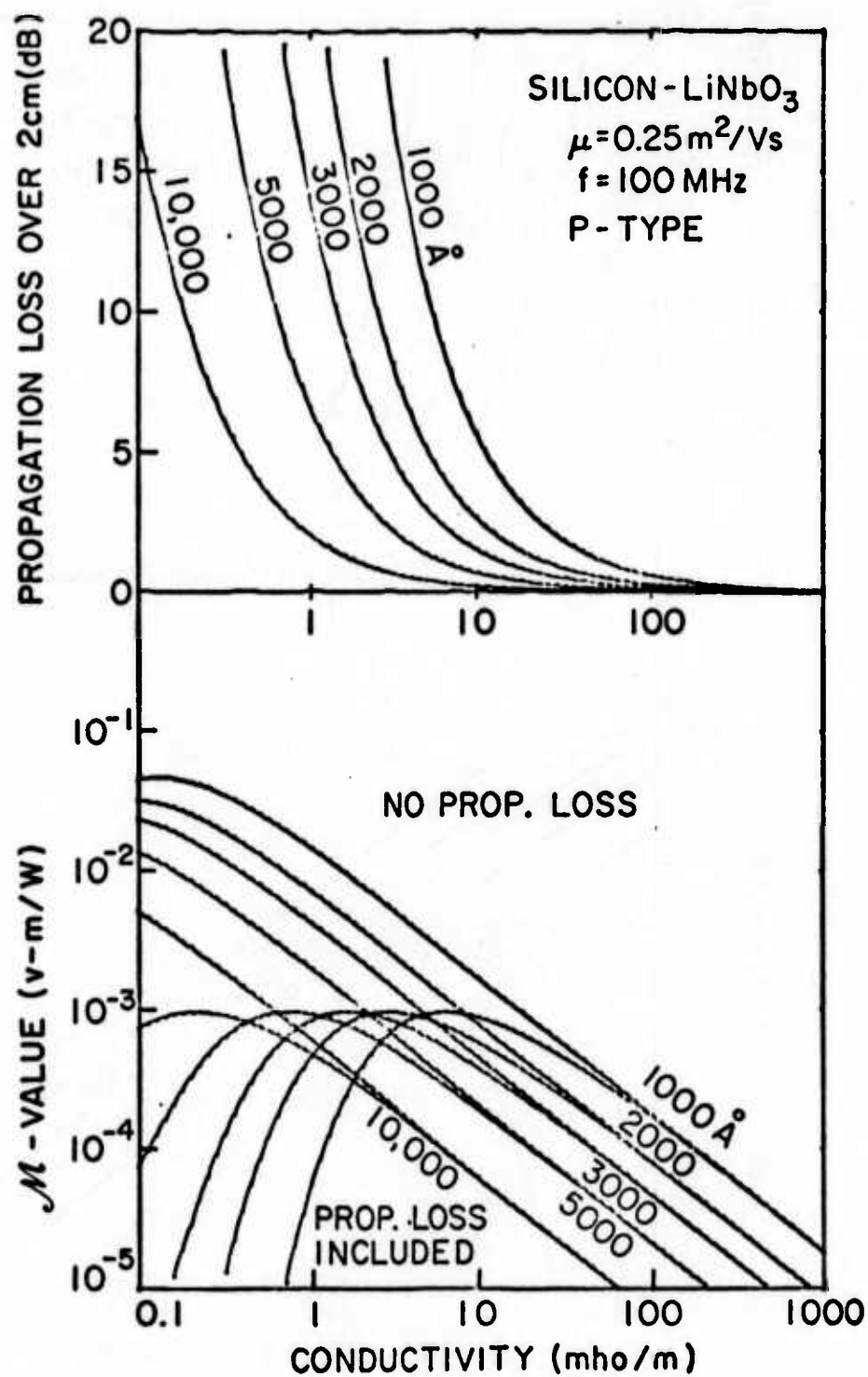


FIG. 2.3-1--Propagation loss and  $M$ -values vs conductivity for various airgaps.

(b) p-type silicon.

The approximation made earlier limits the validity range of these results. A direct comparison with the full theory of Otto<sup>20</sup> shows that the error is less than 10% if the frequency  $f$ , the conductivity  $\sigma$ , and the mobility  $\mu$  are such that

$$f \leq 120 \sqrt{\sigma/\mu} 10^6$$

for a  $\text{LiNbO}_3$ -Silicon system. The present theory is therefore limited to approximately  $f \leq 500$  MHz and  $\sigma > 0.1$  U/m. In practice, interdigital transducers are not easily made to operate above 1 GHz and silicon wafers of conductivity below 0.1 U/m tend to be unstable. This theory is therefore well adapted to the design of practical convolvers.

### 2.3.2 Results for an Untreated Silicon Surface - Deep Depletion Model

The case of untreated silicon (n-type especially) is dealt with separately because of its practical importance: it has been used in most of the early convolvers and it provides a very large nonlinear coupling.

It is now a well established fact that the surface of a semiconductor, like silicon, consists of an oxide film, some  $10^8$  Å thick, together with various chemicals adsorbed from the etchants and the atmosphere. This creates electronic states - the "surface states" - whose energy levels lie within or around the silicon bandgap. When the surface has been given no special treatment, like thermal oxidation,

we may assume that the surface state density is very high - in the  $10^{13} \text{ cm}^{-2}$  range - comparable to the value found under a Schottky barrier. We may estimate the surface potential by using the results obtained for Schottky barriers in which it is normally assumed that there is an interfacial oxide layer of atomic dimension  $\delta$  at the surface of the semiconductor.<sup>22</sup> In addition, it is assumed the presence of surface states at the interface between semiconductor and the layer of thickness  $\delta$ . The Schottky barrier treatment leads to the evaluation of the surface potential at a free surface and the surface states. It is found that the Fermi level is pinned down approximately 0.3 V above the valence band edge and the surface state density is of the order of  $10^{13} \text{ cm}^{-2}$ . For an n-type silicon of  $10 \text{ } \Omega\text{-cm}$  resistivity, this means a dc potential given by the relation

$$q\phi_{s0}/kT = -20 ,$$

i.e., a slight surface inversion (the parameter  $g^+$  defined in Section 2.2.3 is less than 0.01). Although the surface is slightly inverted, we shall compute the nonlinear coupling as if the surface were in deep depletion (see discussion in Section 2.2.2). Figure 2.3-2 gives theoretical plots of the  $\mathcal{M}$ -value in the depletion and accumulation regimes.  $\mathcal{M}$  has been normalized to its value at flat band. As the depletion layer widens, the  $\mathcal{M}$ -value only moderately increases under the combined effect of the increase of the nonlinear coupling and of the decrease of the linear coupling.



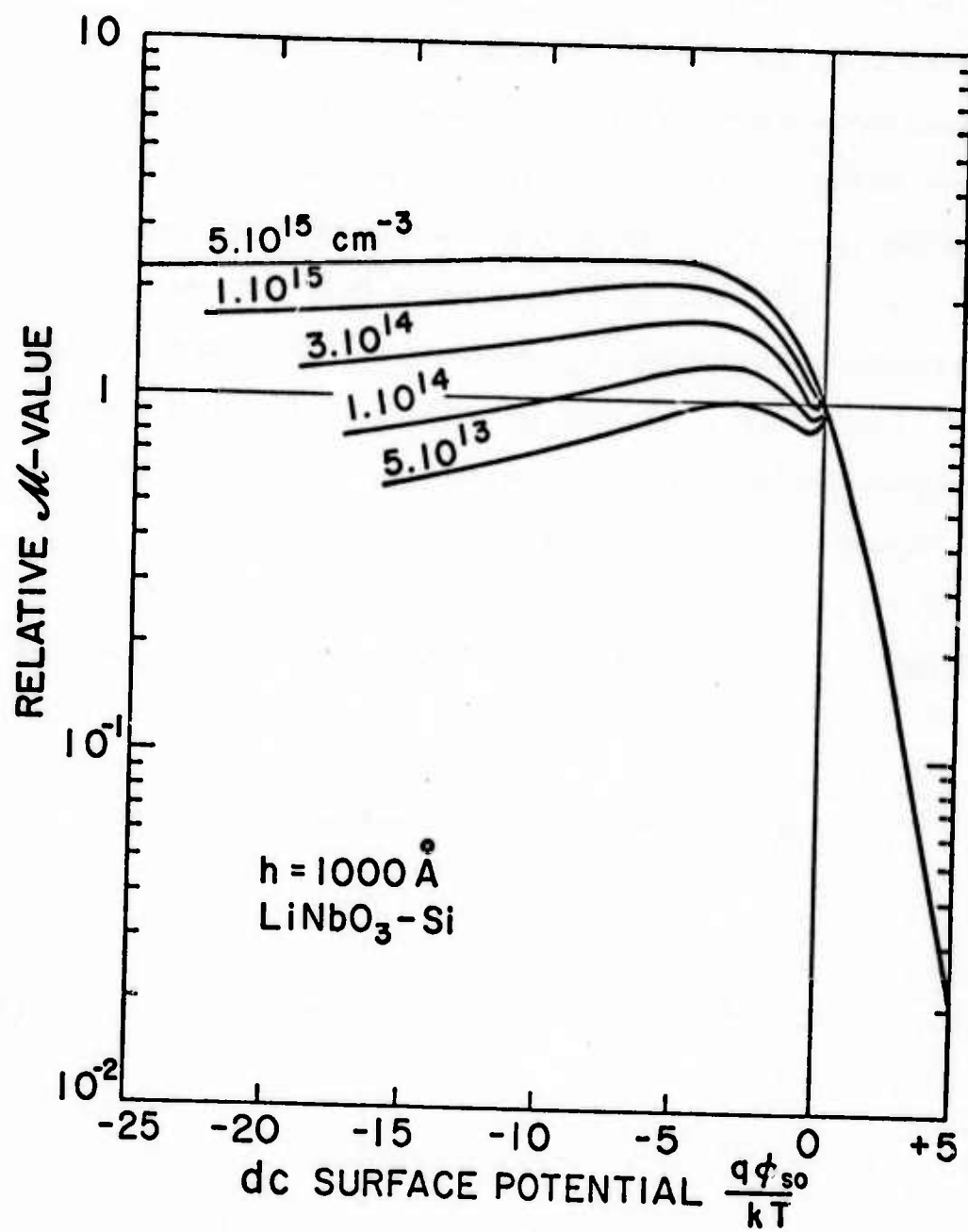


FIG. 2.3-2--  $M$ -values in the case of depleted or accumulated semiconductor surface.

Several experimental devices were constructed and tested to check these results. Both  $\text{LiNbO}_3$  and  $\text{Bi}_{12}\text{GeO}_{20}$  were used in conjunction with various silicon wafers. The output power developed across a  $50\ \Omega$  load was measured and the convolution efficiency computed: this has been defined in Section 2.1.2 as  $F_T$ , the ratio in dB of the output untuned power  $P_e^{(3)}$  (in  $50\ \Omega$ ) to the product of the input electrical powers  $P_e^{(1)}$  and  $P_e^{(2)}$ , all powers in mW. To obtain the open circuit output voltage  $V_{op}$  and hence  $M$ , the output electrical circuit must be known. Accurate measurements of the output impedance of the convolver were carried out in the range 150–500 MHz by using an HP network analyzer. From these data, the equivalent circuit shown in Fig. 2.3-3 was derived. The various elements are easily identified.  $C_1$  is the capacitance between the semiconductor and the

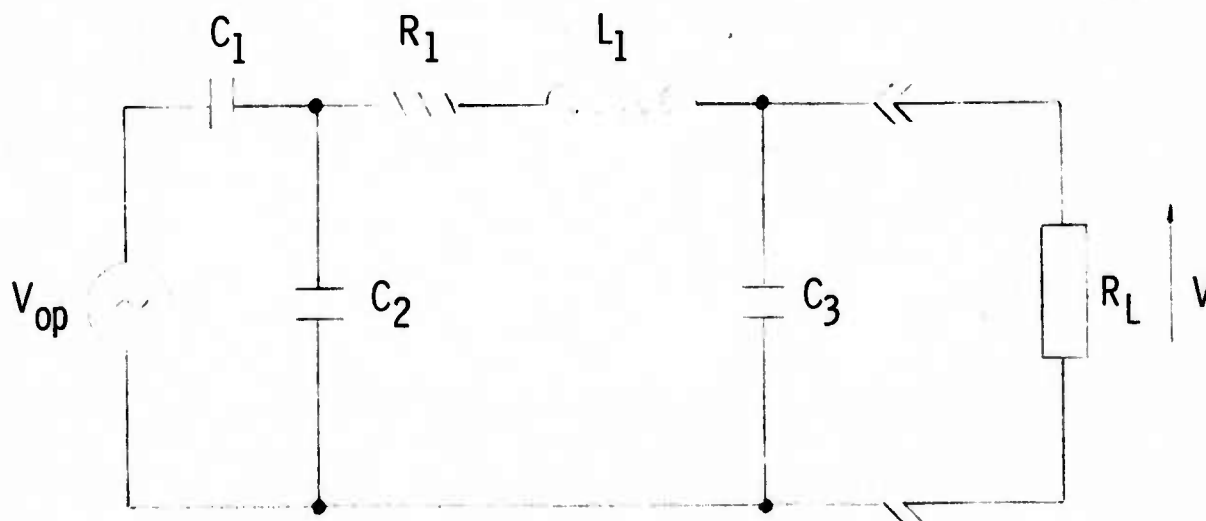


FIGURE 2.3-3

ground electrode over the acoustic beam.  $C_2$  is the extra capacitance to ground,  $R_1$  is the resistance of the output gold leads,  $L_1$  is the inductance of the output leads and grounding connections, and  $C_3$  is the extra capacitance to ground in the lead-connector interface. By theoretical fitting of the measured impedance curves vs frequency, the values of  $C_1 + C_2$ ,  $R_1$ ,  $L_1$  and  $C_3$  were obtained. The ratio  $C_1/(C_1 + C_2)$  was determined from a purely geometrical argument: it is equal to the ratio of the acoustic beamwidth to the semiconductor width. This circuit applies very well to convolvers made with  $\text{LiNbO}_3$ . When  $\text{Bi}_{12}\text{GeO}_{20}$  is used, the capacitors  $C_1$  and  $C_2$  have to be replaced by parallel RLC resonant circuits to account for some internal acoustic resonances in the acoustic medium. Once the output circuit is known, its "voltage transfer function" can be evaluated. This is defined as the ratio of the voltage actually dropped across a  $50 \Omega$  load to the open circuit output voltage  $V_{op}$ . If  $\xi$  is this transfer function, the power loss  $R$  in the output circuit is given by the relation

$$R = 20 \log \xi .$$

Some of the experimental results for  $M$  are given in Table 2.2 and compared to the theoretical predictions for deep depletion conditions. As can be seen, the agreement is very good.

TABLE 2.2

 $\mathcal{M}$ -Values Theory and ExperimentSemiconductor: n-type Silicon; untreated; 2 cm long;  $\mu = 0.1 \text{ m}^2/\text{Vs}$ Piezoelectric: YZ  $\text{LiNbO}_3$ ;  $w = 1.25 \text{ mm}$ ;  $h = 1500 \text{ \AA}$ ;  $f = 108 \text{ MHz}$ (111), ( $\bar{1}\bar{1}\bar{1}$ )  $\text{Bi}_{12}\text{GeO}_{20}$ ;  $w = 1.25 \text{ mm}$ ;  $h = 3000 \text{ \AA}$ ;  $f = 52 \text{ MHz}$ 

Piezoelectric	$\text{LiNbO}_3$			$\text{Bi}_{12}\text{GeO}_{20}$
Si Resistivity ( $\Omega\text{-cm}$ )	7	7	9	7
Concentration ( $\text{m}^{-3}$ )	$7 \times 10^{20}$	$7 \times 10^{20}$	$5.5 \times 10^{20}$	$7 \times 10^{20}$
2-port Insertion Loss <sup>(1)</sup> $L_{\text{TR}} + L_{\text{S}}$ (dB)	14	22	20	18
Convolution Efficiency $F_{\text{T}}$ (dB) <sup>(2)</sup>	-56	-58	-66	-80.5
Output Circuit Efficiency $\xi$ <sup>(3)</sup>	0.4	0.7	0.2	0.18
$\mathcal{M}$ at flat band (theory)	$4.0 \times 10^{-3}$	$4.0 \times 10^{-3}$	$5.5 \times 10^{-3}$	$1.0 \times 10^{-3}$
$\mathcal{M}$ depletion/ $\mathcal{M}$ flat <sup>(4)</sup> band	1.50	1.50	1.40	2.10
$\mathcal{M}$ depletion (theory)	$6.0 \times 10^{-3}$	$6.0 \times 10^{-3}$	$7.7 \times 10^{-3}$	$2.1 \times 10^{-3}$
$\mathcal{M}$ (experiment) (V-m/W)	$5.6 \times 10^{-3}$	$6.3 \times 10^{-3}$	$7.0 \times 10^{-3}$	$1.7 \times 10^{-3}$

- (1) This includes transducer and propagation losses.  
 (2) Ratio in dB of output terminal power (in  $50 \Omega$ ) to product of input terminal powers. All powers in mW.  
 (3) Ratio of voltage actually developed across a  $50 \Omega$  load to open circuit output voltage.  
 (4) From Fig. 2.3-2 and similar one for BGO with  $3000 \text{ \AA}$  (not given) ( $q\phi_{\text{SO}}/kT = -20$ ).

### 2.3.3 Results for Oxidized Silicon - Off Flat Band Regimes - Surface States

Although convolvers built with untreated silicon are among the most efficient, the very large surface state density reduces the light sensitivity of the semiconductor and it makes it almost impossible to vary the dc surface potential by applying any reasonable bias. If the surface of the semiconductor is carefully cleaned and thermally oxidized, then annealed in an inert atmosphere such as nitrogen, the surface state concentration can be reduced by several orders of magnitude.

Like the bulk impurity levels, a surface state can be a donor state or an acceptor state. A donor state is either neutral or positive, when it donates an electron. An acceptor state is either neutral or negative, when it accepts an electron. The probability of occupancy of a surface state by an electron is given by Fermi-Dirac statistics:<sup>22</sup> a state will be occupied if its energy level lies below the Fermi level. It follows that a donor state will be positive (no electron) if its energy level lies above the Fermi level; and an acceptor state will be negative (electron trapped) if its energy level lies below the Fermi level. In all cases, as the Fermi level crosses a state level upward, the surface becomes more negative. In the following, we shall only be interested in the net surface charge and shall no longer specify the type of the states.

By applying a bias voltage  $V_G$  to the structure, the energy bands can be bent at the surface relative to the Fermi level. The probability of occupation of the surface states will thus vary as a function of the

applied bias; so will the charge located in these states, denoted by  $Q_{ss}(V_G)$ . In the case of thermally oxidized silicon, it is found that, in the absence of any bias ( $V_G = 0$ ), the electron concentration is increased at the surface: an n-type silicon will therefore be accumulated and a p-type depleted or inverted. This n-type surface conductance is attributed to the presence of a net donor-type surface state concentration resulting in a positive charge  $Q_{ss}(V_G = 0)$ . As a consequence, the theoretical curves will be shifted towards inversion or accumulation by an amount

$$V = \frac{Q_{ss}(0)}{C_{oxide}}.$$

A further voltage shift will occur as the bias is increased.

We use the results derived in Part 2.2 to obtain a theoretical plot of the relative  $\mathcal{M}$ -value vs bias voltage in the accumulation and depletion regimes. As shown in Figs. 2.3-4(a) and 2.3-5(a), we obtain a very good fit with the experimental data (dots) if we allow for the presence of a charge  $Q_{ss}(0)$  at the Si-SiO<sub>2</sub> interface. The p-type semiconductor starts out slightly depleted corresponding to a  $Q_{ss}(0)/q$  of  $8 \times 10^9 \text{ cm}^{-2}$  (90 volt shift). The n-type semiconductor starts out accumulated with a  $Q_{ss}(0)/q$  of  $9 \times 10^9 \text{ cm}^{-2}$  (100 volt shift). Figures 2.3-4(a) and 2.3-5(a) only show relative values of  $\mathcal{M}$ ; absolute values are compared in Table 2.3, now that we know what the flat band voltages are. The agreement is good here too.

As the bias forces the surface of the semiconductor to invert, the Fermi level begins to scan through the surface states energy distribution near one edge of the bandgap; this will introduce a further

shift of the characteristics. In Figs. 2.3-4(a) and 2.3-5(a) the dashed curves are drawn in the absence of any more surface states; to account for them these curves must be shifted by an amount  $\Delta V$  shown in Figs. 2.3-4(b) and 2.3-5(b) as functions of the surface potential  $q\phi_{s0}/kT$ . The surface state distribution per unit energy  $N_{ss}$  is then obtained by graphical differentiation

$$N_{ss} = \frac{1}{q} \frac{dQ_{ss}}{d\phi_{s0}} = \frac{C_{\text{oxide}}}{kT} \frac{d(\Delta V)}{d(q\phi_{s0}/kT)} \text{ states/cm}^2/\text{eV}.$$

As seen in Figs. 2.3-4(b) and 2.3-5(b), this distribution exhibits maxima near the band edges. The total number of surface states measured in this way is  $Q_{ss} = 2.5 \times 10^{10} \text{ cm}^{-2}$  near the conduction edge and  $Q_{ss} = 5.2 \times 10^{10} \text{ cm}^{-2}$  near the valence band edge. Since it is comparably harder to accumulate strongly than to invert a semiconductor, the surface state distribution could only be studied at one extremity of the bandgap with a given semiconductor. The surface state concentration is rather small because of the careful cleaning and oxidation procedures followed (see Appendix B).

The measure of the  $\mathcal{M}$ -value of the semiconductor convolver therefore provides a new method of measurement of the surface state density. This density is plotted vs energy in Fig. 2.3-6 and compared to the results obtained by other authors.<sup>32,33,34</sup> These authors used MOS diodes and measured either their capacitance or their conductance as a function of the applied gate voltage or by varying the temperature. The distribution we obtain is more sharply peaked around two definite energy levels, 0.2 eV and 0.83 eV. The surface state density was not



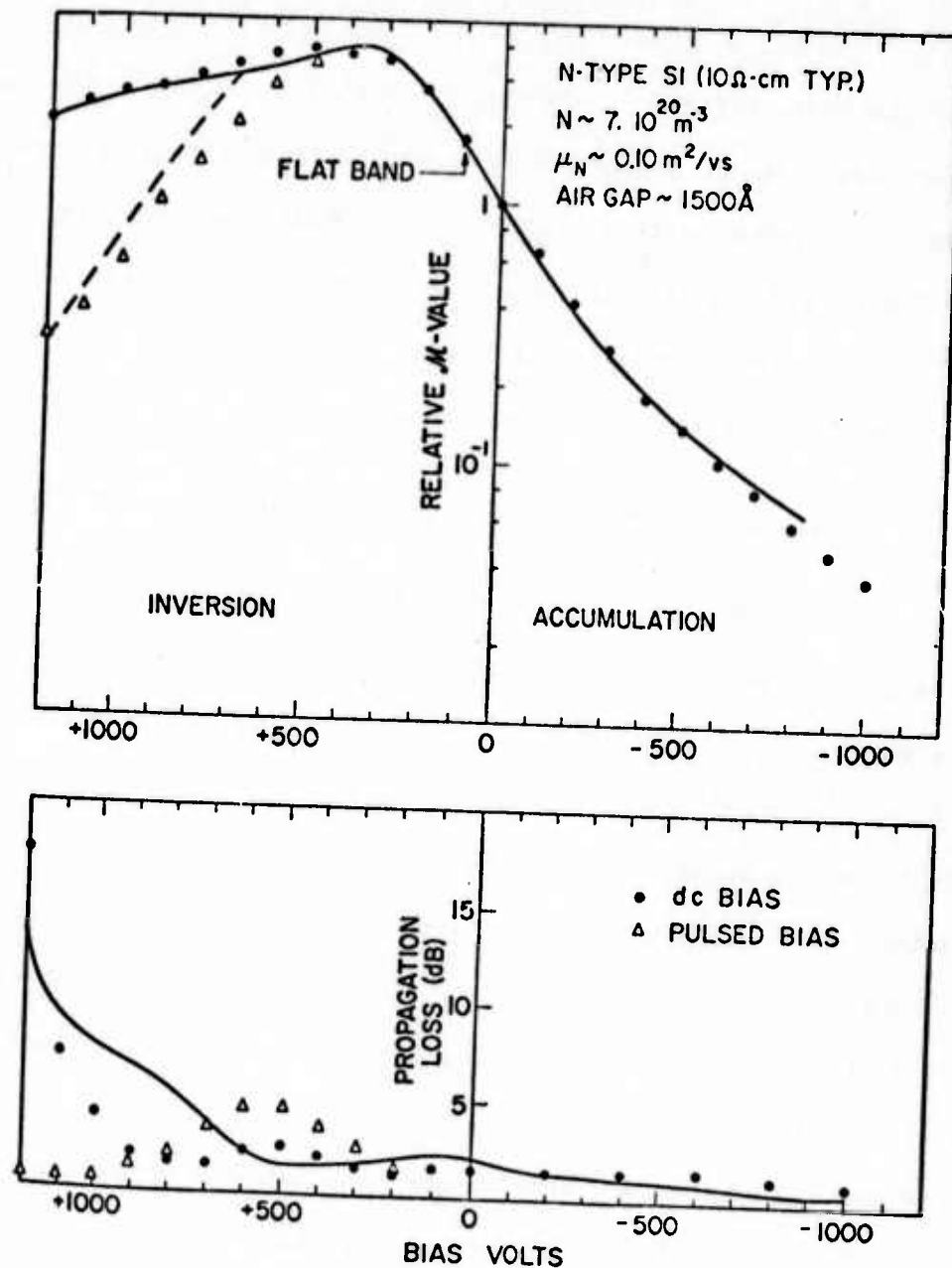


FIG. 2.3-4(a)  $M$ -value and propagation loss vs bias voltage (n-type silicon). The dots are the experimental points in the presence of a dc bias; the triangles are the experimental points in the presence of pulsed bias. The full line curve corresponds to the complete theory, the dashed line curve to the theory in the absence of surface states near the valence band edge.

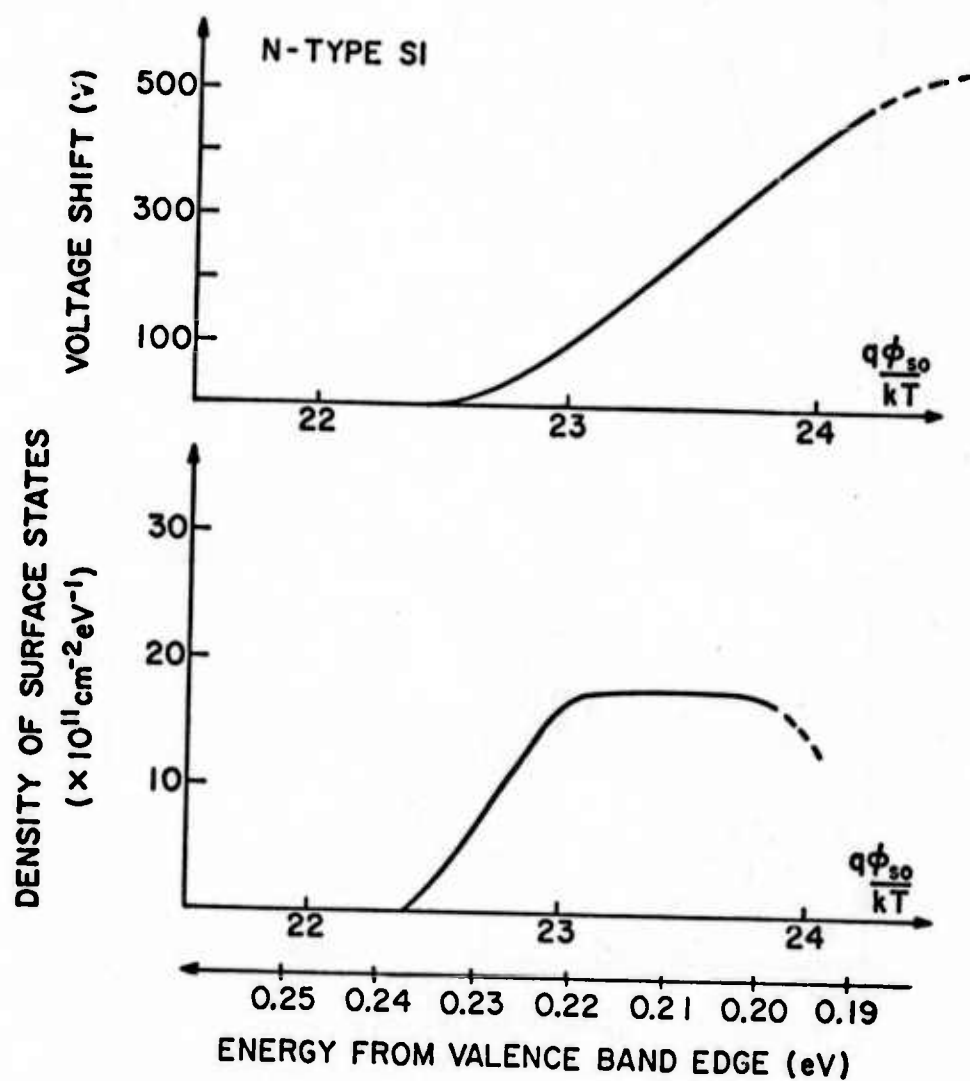


FIG. 2.3.4(b)--Voltage shift and surface state distribution (n-type silicon).

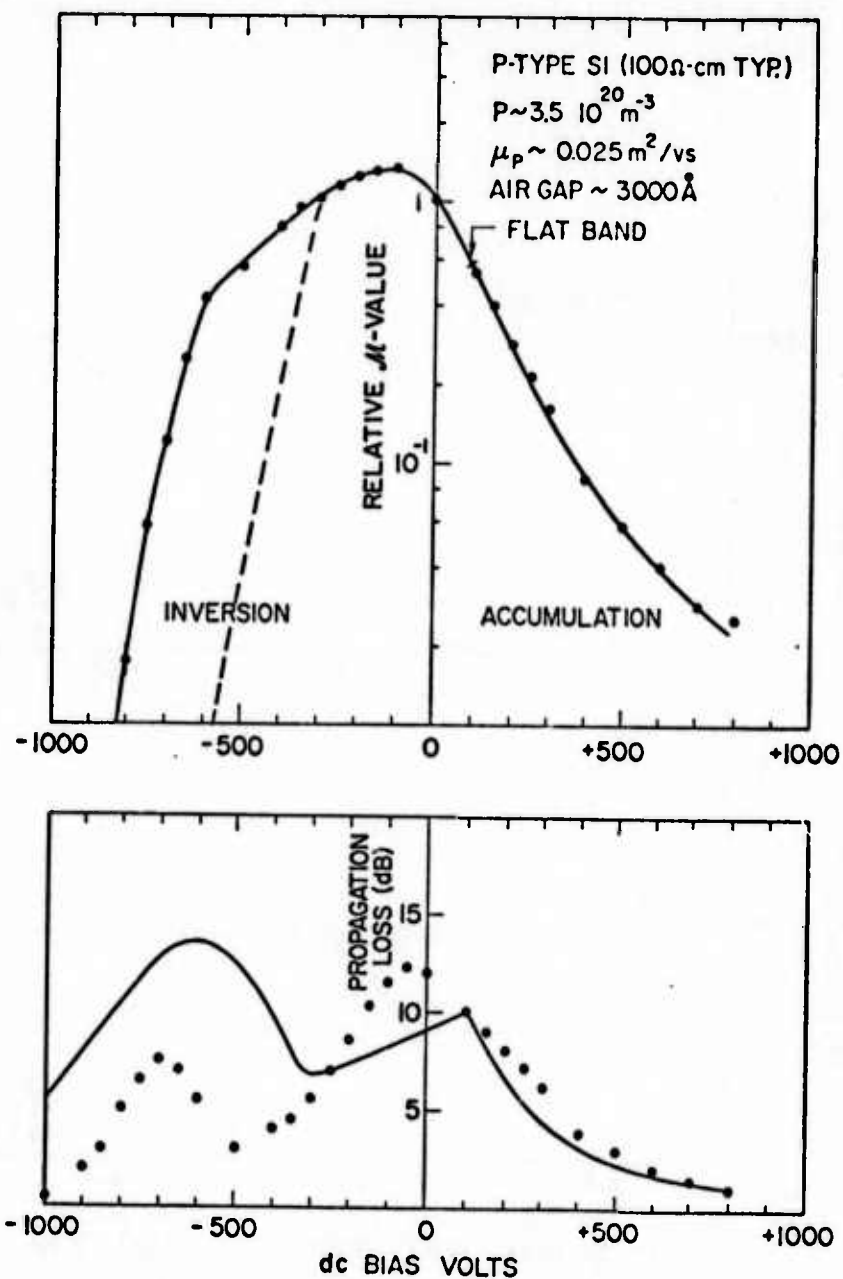


FIG. 2.3.5(a)--- $\mu$ -value and propagation loss vs bias voltage (p-type silicon). The dots are the experimental points. The full line curve corresponds to the complete theory; the dashed line curve to the theory in the absence of surface states near the conduction band edge.

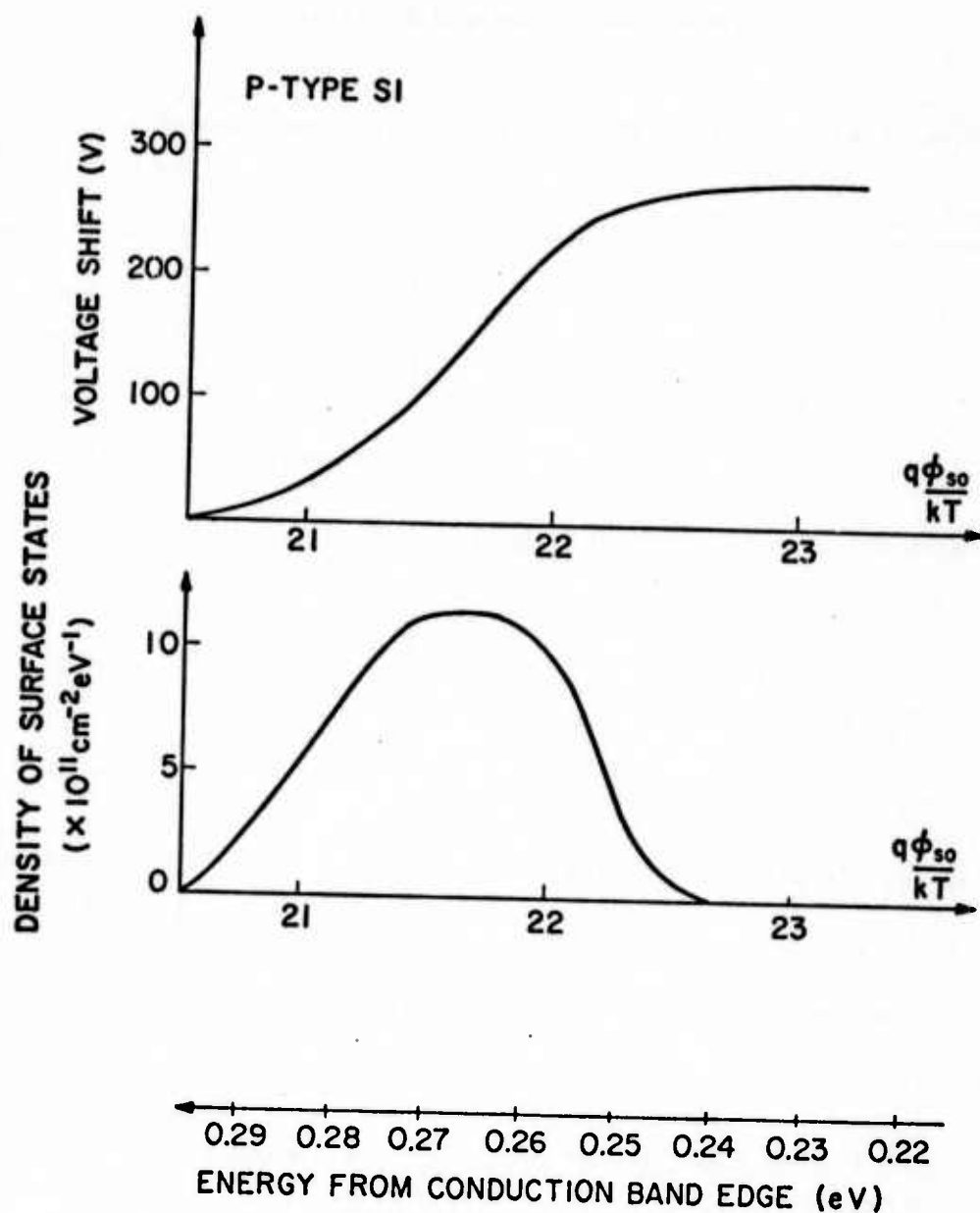


FIG. 2.3-5(b)--Voltage shift and surface state distribution (p-type silicon).

TABLE 2.3

*M*-Values Theory and Experiment

Semiconductor: Silicon; 1000 Å SiO<sub>2</sub> layer; 2 cm long,  $\mu_p = .025 \text{ m}^2/\text{Vs}$   
 $\mu_n = .07 \text{ m}^2/\text{Vs}$   
 Piezoelectric: YZ-LiNbO<sub>3</sub>; w = 1.25 mm; f = 108 MHz

Silicon type	N	P
concentration (m <sup>-3</sup> ) (*)	$7 \times 10^{20}$	$3.5 \times 10^{20}$
resistivity (Ω-cm)	~ 12	~ 70
Airgap (Å)	1500	3000
2-port Insertion Loss <sup>(1)</sup> (No bias) $L_{TR} + L_S$ (dB)	16	30
Convolution Efficiency <sup>(2)</sup> (No bias) $F_T$ (dB)	-66	-74
Output Circuit Efficiency <sup>(3)</sup> %	0.25	0.20
<i>M</i> -value (Experiment, No bias)	$2.8 \times 10^{-3}$	$8.8 \times 10^{-3}$
<i>M</i> at flat band/ <i>M</i> at OV Bias <sup>(4)</sup>	1.7	0.6
<i>M</i> -value at flat band (Expt)	$4.8 \times 10^{-3}$	$5.3 \times 10^{-3}$
<i>M</i> -value at flat band (Theory) (V-m/w)	$4.5 \times 10^{-3}$	$5 \times 10^{-3}$
<i>M</i> -value at optimum voltage	$9.4 \times 10^{-3}$	$8.8 \times 10^{-3}$

(\*) from MOS C-V Measurements

(1), (2), (3) - See Table 2.2

(4) from Figs. 2.3-4(a) and 2.3-5(a)

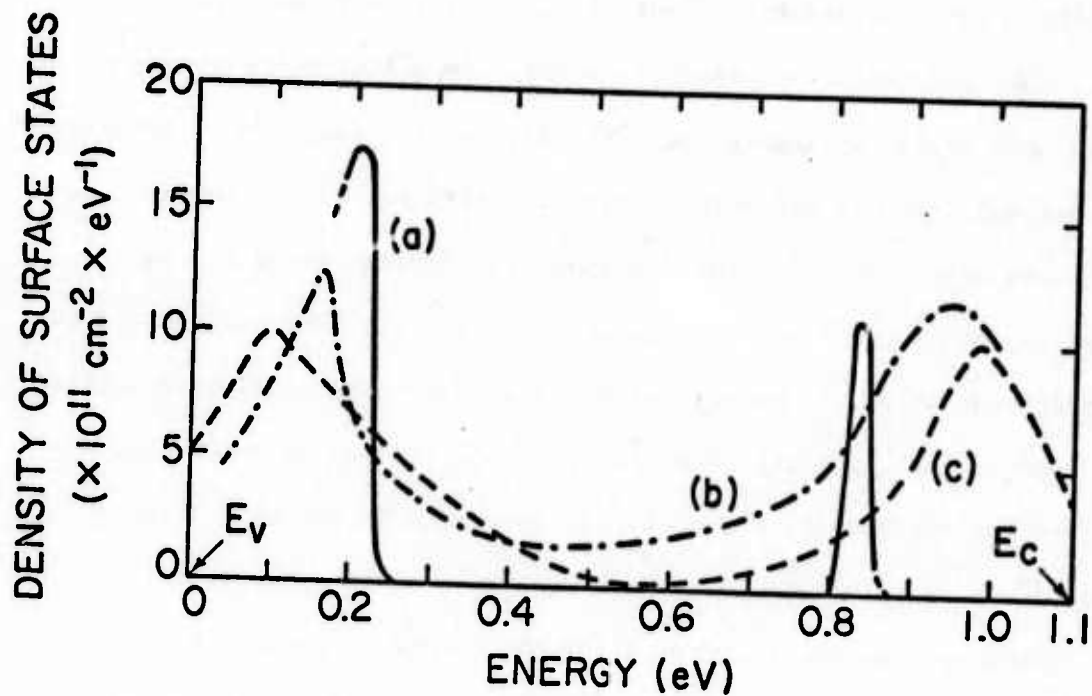


FIG. 2.3-6--Surface state density of Si-SiO<sub>2</sub> structure as obtained from  
 (a) present work,  
 (b) After Nicollian and Goetzberger<sup>34</sup>  
 (c) After Castro and Deal.<sup>32</sup>



measured very close to the band edges  $E_c$  and  $E_v$  because it is almost impossible to have the Fermi level get close to these band edges by the use of an applied gate voltage only. One needs to use the temperature method.<sup>22</sup> The measurement of the voltage shift between ideal and real curves leads to the evaluation of the surface state density. This measurement is most inaccurate in very weak inversion, i.e., when the two curves begin to split. In addition, in this same range, the surface potential is a rapidly varying function of the bias voltage and hence is determined more inaccurately. These two sources of errors may account for the discrepancies between curve (a) and curve (b) or (c) in the energy range 0.25 to 0.4 eV and 0.65 to 0.8 eV. In addition, it should be pointed out that the method used by Nicollian and Goetzberger, in particular, and the indirect way in which they derived the surface state density, is very much argued upon at this time;<sup>57</sup> no definite answer has yet been cast on this matter.

There are two new features about the method we propose here. First we measure a second-order characteristic, namely the derivative of the capacitance w.r.t. the surface potential. In addition, this method is non-destructive, since no metal is deposited on the silicon oxide, therefore no extra impurity centers are added to the surface. We must, however, note that a careful measurement should be made under vacuum so that the possible contaminants from the surrounding air do not affect the long term properties of the surface of the semiconductor.

With this knowledge of the voltage shift introduced by the surface states, we can now plot the theoretical propagation loss due to the semiconductor in all regimes [see Figs. 2.3-4(a) and 2.3-5(a)]. For the



inversion regime, we used the plot shown in Fig. 2.3-7. It shows the theoretical loss vs the inversion strength  $g^+$ . We note that the loss is maximum when  $1 < g^+ < 10$ , which correspond to the minority carrier resonance. The depletion layer approximation is not very accurate in accounting for the propagation loss. The theoretical loss is somewhat higher than experimentally observed in inversion. The inversion layer uniformity is indeed a very sensitive function of the uniformity of the airgap and we noticed that only portions of the surface were inverted; hence the transmission loss was lower than expected. Besides, the model we used for the inversion layer is quite simple and may not be very accurate for light inversion when the inversion layer extends several Debye lengths into the bulk. But the general shape and orders of magnitude can be correctly predicted and in the case of the  $\mathcal{M}$ -value, the agreement is excellent.

We have only discussed, so far, the effect of a dc biasing voltage. If a pulsed bias voltage is now used and if the measurement is made right after the bias is applied, no charge will be exchanged with the surface traps. And for all purposes we may ignore them. No additional voltage shift will take place and large surface fields may be created. As a second consequence of the use of a pulsed bias, no minority carrier will be generated at the surface from the bulk of the semiconductor because of the long generation-recombination times involved in this process. One would therefore expect the surface to be driven in deep depletion. The  $\mathcal{M}$ -value would then remain at the constant depletion level (see Fig. 2.3-2) and the loss would be very

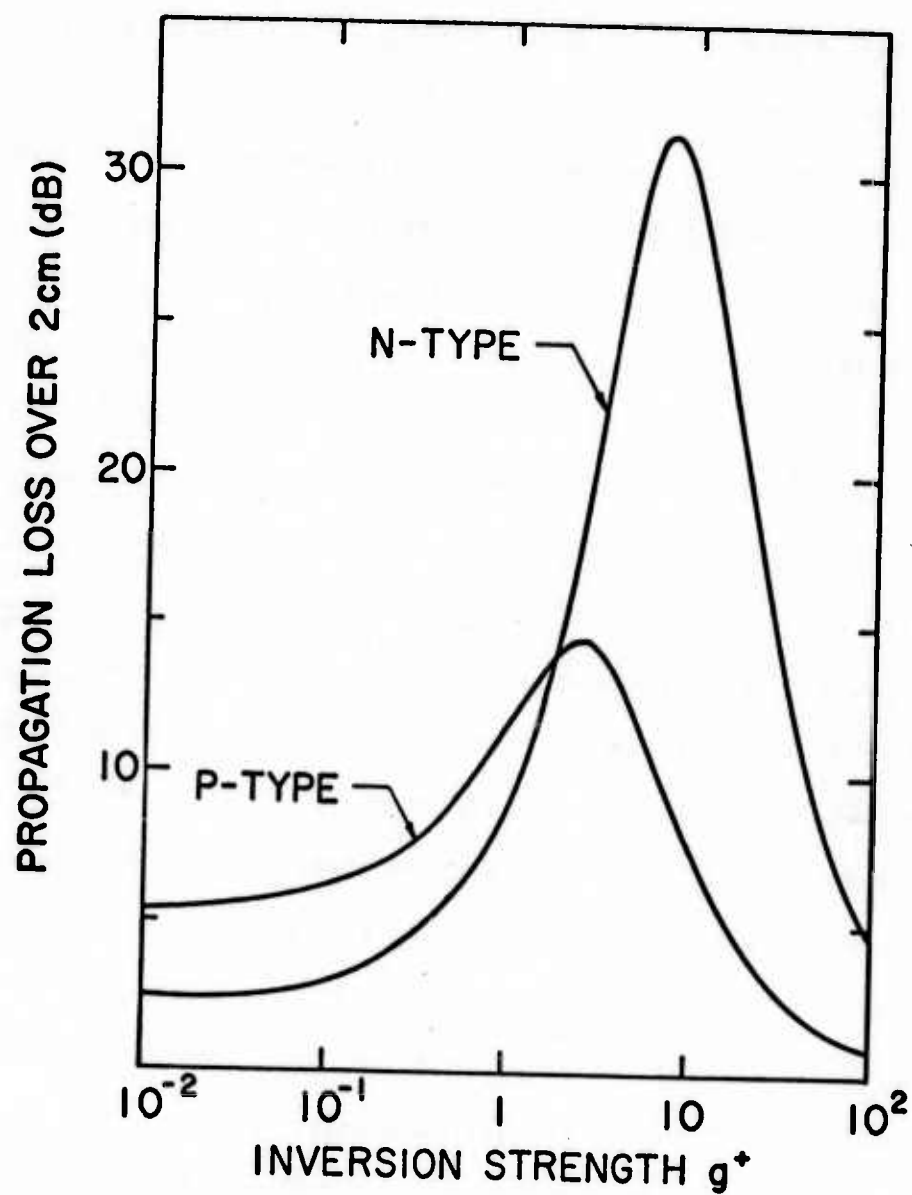


FIG. 2.3-7--Propagation loss vs inversion strength for the two cases given in Table 2.1.

low because of the large depletion layer. Although some convolvers behaved in this manner, others did not. The response of one of these is represented by the triangular dot curves of Fig. 2.3-4(a). The mechanism believed to be responsible for this behavior is the presence, at the surface of the semiconductor, of sources of minority carriers like  $p^+$  impurity centers. Under the high surface fields, these centers can inject a large quantity of minority carriers which will stay confined at the surface because of the biasing field. This is the mechanism that takes place in a field-effect-transistor where one of the end  $p^+$  contacts (the "source") injects minority carriers and thus form the inverted channel of the transistor. Since these carriers are of majority type for the generation centers, the supply will be very fast. Hence, with a pulsed bias an inversion layer is formed, and one would expect the  $M$ -value to decrease as predicted by the previous general theory in the absence of surface states. [see the dashed curve in Fig. 2.3-4(a)]. The results shown in Fig. 2.3-4(a) confirm this assertion well. In addition, the maximum of the propagation loss is now visible because the inversion now occurs for lower voltages, but the value of the maximum is smaller than expected. Once again, airgap nonuniformities may well be one of the reasons for this discrepancy.

Since the dc bias response differs from the pulsed bias response, we have been interested in studying the transient phenomena involved, just as is done in a normal MIS diode measurement. For that purpose, the bias voltage was turned on at the time  $t = 0$  and the output convolution signal was displayed against time by inserting into the

acoustic convolver, two identical pulse trains: the pulse length was  $4 \mu\text{sec}$  and the repetition rate approximately  $30 \text{ kHz}$ . It was found that for bias voltages lower than  $300 \text{ V}$ , the output signal is almost constant in time and it is therefore difficult to measure any decay time. As the bias is increased, the convolution output variation with time becomes essentially exponential. The time taken for the steady state to be reached is maximum for a bias voltage  $V_G = 400 \text{ to } 600 \text{ V}$ , and it is found to be  $15 \text{ ms}$ . This corresponds to a time constant of approximately  $2 \text{ ms}$ . These values of  $V_G$  corresponds respectively to a surface potential  $q\phi_{s0}/kT$  of  $-15$  and  $-24$ ; in other words, they correspond to a semiconductor surface in deep depletion at  $t = 0_+$ . This time constant is associated with the trapping rate in the surface states as we saw earlier and, on this basis, the largest time constants should be expected when the background total concentration of mobile charges is minimum;<sup>34</sup> hence to a surface in deep depletion. The presence of impurities consisting of shallow acceptor centers will perturb the trapping process when they start injecting minority carriers at the surface; as a consequence, the trapping time becomes shorter. No matter whether we consider the surface states as being of donor or acceptor type, the concentration of mobile minority carriers (holes here) will decrease as trapping takes place.

To show this experimentally, we measured the propagation loss versus time after a large biasing voltage had been turned on ( $V_G = 1300 \text{ V}$ ). For  $t < 0$ , the loss is approximately  $2 \text{ dB}$  [see Fig. 2.1-2(a),  $V_G = 0 \text{ V}$ ]. At  $t = 0_+$ , because of the large hole

injection due to the presence of shallow acceptor centers, the surface mobile carrier concentration is very high and the propagation loss decreases to almost 0 dB [see the dashed curve in Fig. 2.1-2(a) with  $V_G = 1300$  V]. As time evolves, trapping takes place, the hole concentration at the surface decreases and the propagation loss is seen to increase monotonically until it reaches the steady state value, i.e., the dc bias value, of 30 dB (see full line curve in Fig. 2.1-2(a) with  $V_G = 1300$  V). If we now look at the convolution output, at  $t = 0_+$ , it decreases sharply by 15 to 20 dB due to the large screening effect introduced by the hole surface concentration. With time, this concentration decreases, the screening becomes weaker and the convolution efficiency increases; but the increase in propagation loss will soon be preponderant and the convolution is seen to go through a relative maximum before it decreases again to finally reach the dc bias level, some 25 dB below the zero bias level [see Fig. 2.1-2(a)].

The results we have just summarized, have shown that very long time constants are associated with surface states on silicon surfaces. These experiments led Hayakawa and Kino<sup>35</sup> to consider a new type of storage process using the same convolver structure. In this process, the information is represented by the amount of charge stored in the surface states; it can be written in or read out acoustically and long storage times of 2 ms or more have been demonstrated.<sup>35</sup> A careful measurement of the storage time vs applied bias voltage was done by Hayakawa; this is in fact a direct measurement of the surface state time constant, and it was found to be in good agreement with previous

theory and measurement by Nicollian and Goetzberger.<sup>34</sup>

A detailed quantitative study of the storage is beyond the scope of this work; but it has recently been the subject of considerable interest<sup>35,36,37</sup> because of the possibility of building acoustoelectric correlators with memory.

#### 2.4 CONCLUDING REMARKS

It has been shown that for real semiconductors, the effect of surface states is dominant and cannot be overlooked. In particular, if untreated n-type silicon is used, deep depletion must be assumed at the surface. Several experiments were conducted and confirmed this assumption. Furthermore, if a convolver is designed to be optimized for flat band conditions, its convolution output can still be enhanced if the surface of its semiconductor is depleted. The untreated n-type silicon surface is naturally almost intrinsic and it is therefore a good choice when only electrical signal processing applications are the aim.

Oxidized silicons were studied in detail. The propagation loss and convolution efficiency were compared to theoretical predictions on the basis of our model. The same conclusions concerning the optimum operating conditions hold. In addition, this study provided a new measurement technique of the surface state distribution in silicon. Detailed information about the surface state is supplied by the study of the variation of the convolution efficiency and of the propagation loss with respect to the applied bias voltage. In addition, the use

of pulsed bias and the study of the transient responses provide a direct measurement of the time constant of the surface states. We shall also see in Chapter IV, that illumination of the semiconductor affects the convolver characteristics and some extra information, like the lifetime of minority carriers, can be retrieved.

The semiconductor-airgap-piezoelectric convolver is therefore a very powerful tool for the investigation of semiconductor surfaces. The effect of bias has been treated in some detail here, but the effect of illumination could be studied more deeply and so could the effect of temperature.



CHAPTER III  
APPLICATION OF THE SEMICONDUCTOR CONVOLVER TO  
ACOUSTIC PARAMETRIC SIGNAL PROCESSING

In this chapter, we show how the separated medium semiconductor-piezoelectric configuration, studied previously, can be used as an efficient signal processor, and how it compares with other acoustic devices.

Parametric signal processing using acoustics has been the subject of considerable interest for the last few years, because of the new techniques it brought to this field. Among them are real time convolution,<sup>30,6</sup> and Fourier transform,<sup>38</sup> pulse compression,<sup>39</sup> and time inversion.<sup>40</sup> Under the label "parametric" we include all the techniques by which, from two input signals, one can generate a third one at the sum or difference frequency. In an acoustic wave device, these signals may be traveling waves or standing waves with electric fields associated with them if the material is piezoelectric. A parametric processor must therefore include a nonlinear mechanism allowing for the coupling of the waves. There are two major such nonlinear mechanisms. The first is the acoustic nonlinearity of the acoustic medium itself on or through which the acoustic waves propagate. Quate and Thompson<sup>6</sup> first studied bulk wave interactions, Svaasand<sup>41</sup> and Luukkala and Kino<sup>40</sup> studied surface wave interactions for this purpose. In the second mechanism, the electric field associated with the acoustic waves interact with charge carriers in a semiconductor located within or near

the piezoelectric medium; and wave-wave coupling is achieved through the space charge nonlinearity. There exists two classes of devices built on this principle: one uses a piezoelectric semiconductor. This was first investigated by Wang<sup>42</sup> and Turner, et al.,<sup>43</sup> with CdS, then by Ludvik<sup>15</sup> with GaAs. In the other class, described in this report, the semiconductor is placed in close proximity to a piezoelectric (references 3, 44, 4, this work) or the piezoelectric is deposited on the surface of a semiconductor thus forming a monolithic structure.<sup>12,45,14</sup>

The piezoelectric nonlinearity is limited and the devices making sole use of it exhibit low efficiencies. Various methods of beam guiding<sup>46,47</sup> or of beamwidth compressing<sup>48</sup> have been used with success to increase the power density in the wave and hence the nonlinear efficiency.

On the other hand, the space charge nonlinearity can be very strong, and efficient devices have been built, but the corresponding technology is more difficult. Some of the problems such as interaction uniformity in non-monolithic devices and material preparation in monolithic devices require much care. One unique feature of the semiconductor systems is their light sensitivity (see Chapter IV).

In Section 3.1, we shall study the semiconductor-airgap-piezoelectric convolver from a device point of view. We shall be mainly interested in its electronic characteristics such as time-bandwidth product, terminal efficiency and dynamic range. We shall compare the different types of convolvers presented earlier.

In Section 3.2, we shall describe other signal processing applications, in particular, code recognition, time inversion, correlation and Fourier transformation. Here, the parametric processor may be considered as a programmable filter: one of the inputs acts as a reference or a filter for the other. Since this reference can be varied, the filter is programmable.

### 3.1 CONVOLUTION

The standard semiconductor-piezoelectric configuration is illustrated in Fig. 3.1-1. A surface wave delay line is polished optically flat and interdigital transducers are deposited at either end. Two materials have been used: Y-cut, Z-propagating  $\text{LiNbO}_3$  because of its high piezoelectric coupling and (111)-cut,  $(\bar{1}\bar{1}\bar{1})$ -propagating  $\text{Bi}_{12}\text{GeO}_{20}$  (BGO) because of its slow acoustic velocity. The standard transducers have four finger-pairs, the aperture is 1.25 mm and the finger width and spacing is 8  $\mu\text{m}$ . On  $\text{LiNbO}_3$  ( $v = 3480$  m/s) the operating frequency range is  $108 \pm 11$  MHz; on BGO ( $v = 1620$  m/s) it is  $52.5 \pm 5.5$  MHz. A silicon chip is pressed down on spacer rails deposited on the piezoelectric surface. The rail thickness varies from 1000  $\text{\AA}$  to 5000  $\text{\AA}$  and the system relies on the flexibility of the semiconductor to follow the rails to maintain a uniform airgap and hence a uniform interaction strength. On  $\text{LiNbO}_3$ , the rails are made of sputtered  $\text{SiO}_2$ ; because of the chemical activity of BGO, three layer rails had to be used on BGO (1000  $\text{\AA}$  of  $\text{ThOF}$ ; 700  $\text{\AA}$  of  $\text{ZnS}$ ; 1500  $\text{\AA}$  of  $\text{ThOF}$ ). Electrodes on the top and bottom of the structure allow for a capacitive pick-up of the

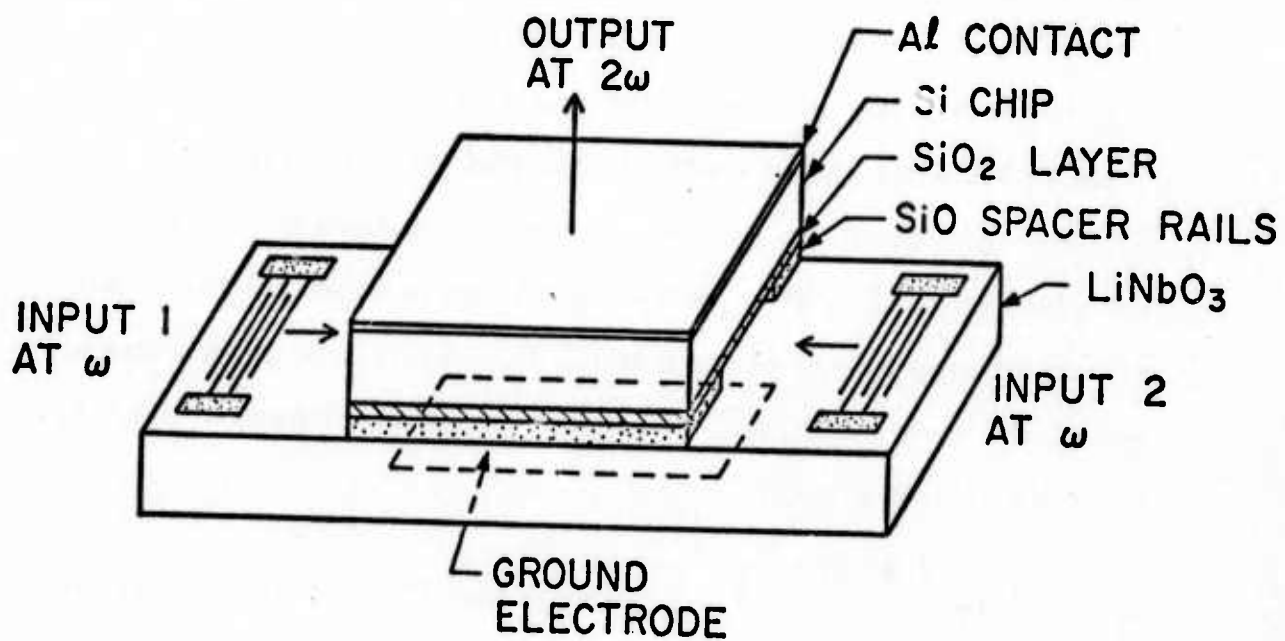


FIG. 3.1-1--Schematic of the semiconductor convolver.

parametric output. The silicon chips are typically 20 to 30 mm long, 5 mm wide and 250  $\mu\text{m}$  thick. When the semiconductor is untreated, it is only cleaned in the usual solvents and kept dust-free. If a further oxidation is needed, a special cleaning procedure is followed to remove all contaminants; after thermal oxidation, the surface is annealed in nitrogen to lower the surface state density down to the  $10^{10} \text{ cm}^{-2}$  range. Details of this procedure are given in Appendix A.

Characteristics of some of the convolvers built on this model are given in Table 3.1 and we shall now describe them in detail.

From a device point of view, an important parameter is the terminal efficiency  $F_T$ ; it is defined as the ratio in dB, of the output electrical power to the product of the input electrical powers when all powers are expressed in mW. Recalling the results of Section 2.3,  $F_T$  is of the following form:

$$F_T = 20 \log \left( \frac{\mathcal{M} \cdot 10^{-L/2}}{2 R_L w} \right) - \text{Transducer Loss (dB)} - \text{Output Circuit Loss (dB)} \quad (3.1-1)$$

where  $R_L$  is the load resistance.

In designing a convolver, the choice of the materials, airgap and resistivity is made from the results of Section 2.3. In our case,  $\text{LiNbO}_3$  and BGO were used to be able to operate in the VHF range with efficient transducers; we decided upon silicon as the semiconductor because of its availability and because of the good control over its resistivity up to 100  $\Omega\text{-cm}$ . Optimum choices of the airgap height are

TABLE 3.1

## Device Characteristics

Piezoelectric:  $\text{LiNbO}_3$  YZ or  $\text{Bi}_{12}\text{GeO}_{20}$  (111)( $\bar{1}\bar{1}\bar{1}$ );  $w = 1.25$  mm

Semiconductor: Silicon, 2 cm long

Piezoelectric	$\text{LiNbO}_3$			BGO
Airgap ( $\text{\AA}$ )	(1) 1500	(2) 1500	(3) 3000	(4) 3000
Silicon type resistivity ( $\Omega\text{-cm}$ )	N 7	N 10	P 70	N 10
2-port insertion loss (dB)	14	15.5	23	18
Convolution Efficiency (dB)	Untuned	-56	-55	-67
	Tuned	-44.5	-44	-61
M-Value (V-m/W)	$5.6 \times 10^{-3}$	$9.4 \times 10^{-3}$	$8.8 \times 10^{-3}$	$2.1 \times 10^{-3}$
Interaction Uniformity (dB)	$\pm 1.5$	$\pm 1.5$	$\pm 1.5$	$\pm 0.7$
Frequency (MHz)	108	108	108	52.5
Input Bandwidth (MHz)	14	23	20	7
Processing Time ( $\mu\text{s}$ )	5.5	5.5	5.5	11.5
Remarks		Optimum Bias Used		

- (1) Same device as in column 1 of Table 2.2  
 (2) Same device as in column 1 of Table 2.3 (oxidized silicon)  
 (3) Same device as in column 2 of Table 2.3 (oxidized silicon)  
 (4) Same device as in column 4 of Table 2.2

then 1000 Å to 1500 Å with 10  $\Omega$ -cm silicon and 3000 Å with 100  $\Omega$ -cm. If the semiconductor is oxidized, a bias voltage will, in general, be necessary to drive the surface into depletion and hence optimize the  $M$ -value.

As seen from Eq. (3.1-1) the acoustic beamwidth should be as small as possible; beam guiding and compressing techniques have been used by other authors<sup>46,48,47</sup> for that purpose. In the absence of any such guiding, the minimum width is limited by diffraction of the acoustic wave, and the choice of a reasonable impedance for the input transducers.

The output electrical circuit must be carefully designed. In particular, the width of the output electrode must be chosen as close as possible to the beamwidth in order to reduce any stray capacitance to ground which would act as a capacitive bridge and reduce the maximum available voltage. Simple spacer rails do not allow for a complete cancellation of the stray capacitance. Output tuning will also enhance the power transfer.

We have been able to build devices with terminal efficiencies as high as  $F_T = -44$  dB. This is among the highest device efficiencies reported to-date if we exclude the multistrip coupler convolver of Shreve.<sup>49</sup> Probably more important than the efficiency, is the dynamic range of the system. It is limited by the saturation effects and the spurious signal level. In our devices, the 3 dB compression of the bilinearity corresponds to an input power of 20 dBm; the noise in the detection system is at -95 dBm, so we could expect a dynamic range of



more than 85 dB. This is actually the case when the two input powers are identical but, in practice, one of the input signals is taken as a reference of constant power. The dynamic range will then not be limited by the noise level but by the reflections of the signal of higher power off the end transducers and the edges of the silicon. With the present devices, the dynamic range is found to be limited to approximately 50 dB. Many solutions have been proposed to reduce the echoes on a surface wave delay line and it seems certain that with their help, we could increase the dynamic range to some 60 to 70 dB.

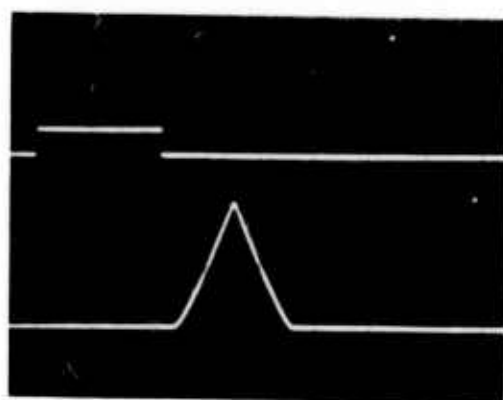
A second parameter of importance is the uniformity of the airgap. This will relate to the accuracy of the convolution product and the quality of the system as a signal processor. Testing of the gap uniformity, i.e., of the nonlinear coupling uniformity is performed by convolving a narrow rf pulse with a very long one; the output should be trapezoidal in shape with a flat top over a time corresponding to the acoustic delay under the semiconductor less the narrow pulse length. Furthermore, the shorter the narrow pulse, the more accurate the picture of the gap uniformity. The measure of the amplitude variation in the output waveform will define the "uniformity" of the gap. It has been determined from experience (code recognition experiments) that a uniformity of  $\pm 1$  dB is adequate for most processing applications.

With careful cleaning of the surfaces of the semiconductor and of the piezoelectric, we have obtained consistently uniformities of  $\pm 1.5$  dB or less (see Table 3.1). Excellent results ( $\pm 0.7$  dB over 11  $\mu$ sec) were obtained with a BGO delay line. This is attributed to the softness

of the material, whose surface can deform more easily to match the shape of the semiconductor surface. Oscillograms showing the uniformity and the accuracy of the convolution product in two particular instances are given in Fig. 3.1-2 for the BGO-silicon system.

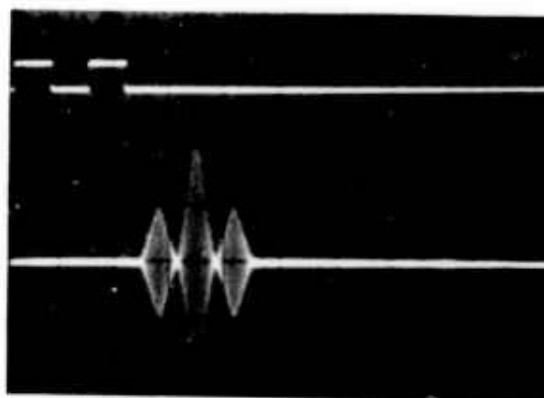
The airgap height is subject to some changes with time and atmospheric conditions. One method to improve its uniformity and stability was devised by Smith, et al.<sup>50</sup> They ion-beam etch small posts in the  $\text{LiNbO}_3$  and pressed a narrow strip of silicon on them. This made the interaction strength more uniform and furthermore, solved the stray capacitance problem we mentioned earlier.

The quantity of information a system is able to process is measured by its Time-Bandwidth product, TB, where  $T$  is the maximum duration of the input signals which can be accurately processed and  $B$  is the 3 dB bandwidth of the system, as measured on the input. In the case of the acoustic surface wave convolvers,  $T$  depends on the interaction length and on the acoustic velocity of the piezoelectric. Technological difficulties limit the usable length of the semiconductor to 20 to 30 mm; these difficulties are related to the availability of large good quality semiconductor wafers and, above all, to the ability to maintain a uniform gap over long distances. Let us point out that similar limitations exist with the integrated monolithic devices. On the other hand, this problem is not as acute in the devices using only the piezoelectric nonlinearity. Low velocity piezoelectrics are suitable to increase  $T$  but they will make the realization of high frequency interdigital transducers harder, because



→ | ← 5  $\mu$ s

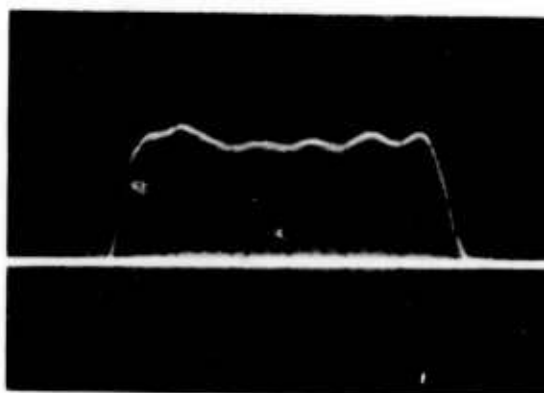
(a)



→ | ← 5  $\mu$ s

(b)

1.5 dB  
↑ ↓



→ | ← 2  $\mu$ s

(c)

FIG. 3.1-2--Bi<sub>12</sub>GeO<sub>20</sub>-airgap-Silicon convolver.

- (a) Autoconvolution of one square pulse;
- (b) Autoconvolution of a double pulse;
- (c) Picture of the uniformity of the interaction over 2 cm.

the acoustic wavelength and, hence, the finger width will be smaller.

As can be seen from the derivations of Chapter II, the nonlinear effect is a slow function of frequency; the bandwidth will therefore essentially be limited by the transducer response. Wideband operation can be achieved with transducers with small number of finger pairs and adequate tuning circuits, but the efficiency will be reduced. In our devices, we used 4 finger pair transducers; on  $\text{LiNbO}_3$ , they are tuned by means of a simple series inductor and they yield a 20% bandwidth together with a low insertion loss; on BGO they are not quite optimal and the bandwidth is only 15%.

Devices built with 4 finger pair transducers, and employing 2 cm long silicon pieces, exhibit typical TB products in the 100 to 200 range, depending on the piezoelectric material and the operating frequency (50 to 100 MHz on BGO; 100 to 200 MHz on  $\text{LiNbO}_3$ ).

For comparison purposes, we have gathered in Table 3.2, the characteristics of most of the acoustic surface wave convolvers reported on to-date, with the exception of those corresponding to the present work; these were detailed in Table 3.1. The device parameters we have been discussing in this section are given when available; the  $M$ -values are also included. The most efficient structure makes use of a multi-strip coupler between the acoustic beam and the semiconductor.<sup>49</sup> Although the efficiency is very high ( $F_T$  up to -23 dB), for this reason the system saturates for very low levels (of the order of 0 dBm); furthermore, it is very sensitive to reflections at the strips. This limits its applications as a practical convolver. The semiconductor-

TABLE 3.2  
COMPARISON OF THE CHARACTERISTICS OF VARIOUS ACOUSTIC SURFACE WAVE CONVOLVERS

Type (*)	Materials	Velocity (m/s)	Beamwidth (mm)	Interaction Length (mm)	Frequency (MHz)	$\eta$ -Value (Vm/V)	F <sub>T</sub> (dB)	2-port loss (dB)	Remarks	Reference
I	LiNbO <sub>3</sub> YZ	3480	1	15	33	$1.21 \times 10^{-4}$	--	--	Waveguide 20 : 1 Multistrip compressor 15 : 1 Bandwidth = 48 MHz; BT = 400	23
I	LiNbO <sub>3</sub> YZ	3480	1	20	200	$2.0 \times 10^{-4}$	-81	17		24
I	LiNbO <sub>3</sub> 41.5°-ZX	4000	3.72	24	21.5	$2.86 \times 10^{-3}$	-71.3	19		47
I	LiNbO <sub>3</sub> YZ	3480	1.65	42	156	$1.1 \times 10^{-3}$	-55	24.5		48
II	LiNbO <sub>3</sub> YZ-Si(8.2 Ω-cm)	3480	0.5	12	193	$6.1 \times 10^{-3}$	-64	17	Cap = 1000 Ω Optimum bias Optimum bias Cap = 1000 Ω; optimum bias	4
II	LiNbO <sub>3</sub> YZ-Si(100 Ω-cm)	3480	--	4	35	$21 \times 10^{-3}$	--	--		5
II	PZT-H <sub>2</sub> O-Si(10 Ω-cm)	2600	4	5	14.5	$1.9 \times 10^{-3}$	--	--		51
II	LiNbO <sub>3</sub> YZ-Si(1 Ω-cm) (10 Ω-cm) (140 Ω-cm) (30KΩ-cm)	3480 " " "	-- -- -- --	-- -- -- --	165 " " "	$7 \times 10^{-3}$ $14 \times 10^{-3}$ $17 \times 10^{-3}$ $5 \times 10^{-3}$	-62 -42 -46 -55	-- -- -- --		52
II	LiNbO <sub>3</sub> YZ-Si(9 Ω-cm)	3480	~ 1	32	190	$1.2 \times 10^{-3}$	-62	19	Cap = 2000 Ω; "post" configuration Uniformity = ± 1 dB; BT = 600 Bandwidth = 65 MHz Multistrip coupler to silicon Uniformity = ± 0.5 dB; low level sat.	50
II	LiNbO <sub>3</sub> YZ-Si(7 Ω-cm)	3480	~ 1.5	10	42.5	$600 \times 10^{-3}$	-23	--		49
III	GaAs (110)(011)	2860	2.1	6	176	$1.01 \times 10^{-3}$	-90-100	40-50	Optimum bias Optimum bias Uniformity = ±1.5 dB Multistrip coupler narrow-band 10%	15
III	GaAs (110)(011)	2860	1.4	~ 10	165	$0.60 \times 10^{-3}$	~ -65	15		16
III	ZnO/Si(111)(112̄)(10 Ω-cm)	3600	1	20	120	$3.20 \times 10^{-3}$	-58	18		12
III	AlN/SOS	3800	~ 1	~ 10	385	$0.73 \times 10^{-4}$	-94	19		15

# In the waveguide structures, the  $\eta$ -value is computed by using the input beamwidth.

(\*) Type I: Piezoelectric nonlinearity only

Type II: Space charge nonlinearity, separate medium structure

Type III: Space charge nonlinearity, monolithic structure

airgap-piezoelectric systems have good dynamic ranges and the TB product can be as high as 500 to 1000 when one uses special technologies to maintain a long uniform gap, and wide band transducers.<sup>50</sup> Finally, very practical devices using  $\text{LiNbO}_3$  and beam-compressors have been demonstrated<sup>48</sup> and they show good efficiency and dynamic range and TB product in the range of 400. This structure is planar, it uses no semiconductor and it looks very promising.

### 3.2 OTHER SIGNAL PROCESSING APPLICATIONS

The output of a time invariant linear filter is the convolution of the input signal with the filter impulse response. In the acoustic parametric convolver, we can consider one of the inputs as a reference or "filter impulse response" for the other. The system is thus a linear filter with variable impulse response.

The general purpose of filtering a signal is to extract information of interest by discriminating against other information contained in the signal, or against spurious signals. If the shape - say  $f(t)$  - or the spectrum of the signal is known, but not its time of occurrence, there exists an optimum filter - the "matched filter" - which maximizes the output signal-to-noise: its impulse response  $h(t)$  is the time inverted version of the signal it is matched to, i.e.,  $h(t) = f(-t)$ . This filter is also sometimes called a correlation filter, since its output is the autocorrelation of the input signal, i.e.,

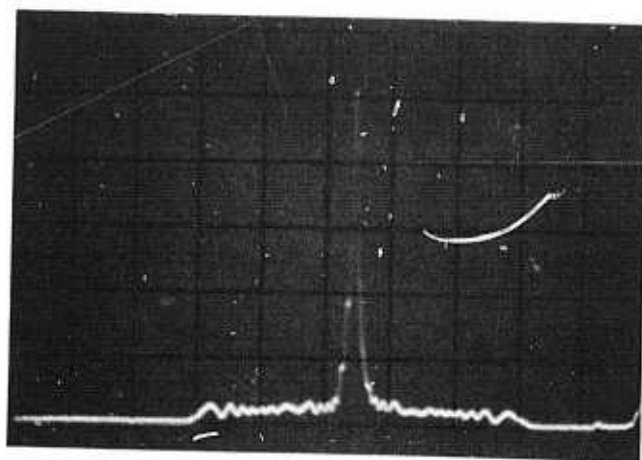
$$g(t) = \int f(\tau) \cdot f(\tau + t) d\tau \quad (3.2-1)$$

The parametric convolver is well suited for this signal detection or signal recognition, provided the signal is inverted in time before it is used as the reference. We shall give examples of such operations for which the signals  $f(t)$  are coded so that the autocorrelation output is sharply peaked with low sidelobes.

Symmetrical V-FM chirp signals are especially easy to use because of their even parity. In the example shown in Fig. 3.2-1, the input signal is gated on for 5.7  $\mu$ sec and swept in frequency from 104 MHz to 111 MHz and back to 104 MHz. The output is a compressed pulse whose 3 dB-width should theoretically be  $0.44/\Delta f$ , where  $\Delta f$  is the frequency excursion.<sup>53</sup> The measured 3 dB-width is 60 nsec, a result in good agreement with the theoretical value of 63 nsec. This experiment corresponds to a 90:1 compression ratio. The maximum compression ratio is approximately 2.3 times the Time-Bandwidth product of the system.

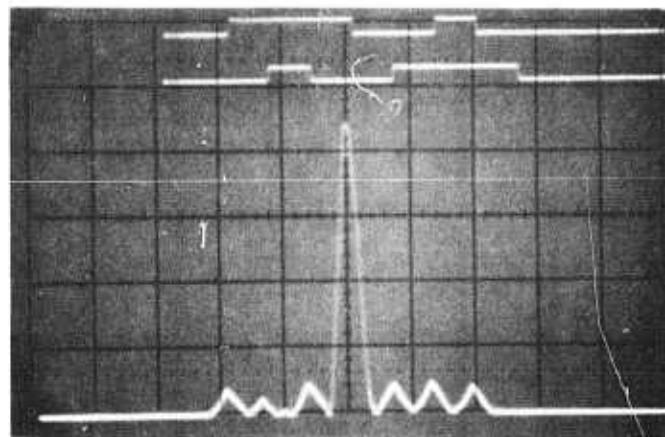
Digital codes have also been used; among them, the biphase Barker sequences. They have the property that their autocorrelation product has a peak with amplitude equal to the number of bits and relative sidelobes of -1, 0, and +1 only; all the lobes are triangular in shape. Examples of 7-bit and 11-bit Barker code autocorrelations are shown in Fig. 3.2-2. The nonuniformity of the interaction region ( $\pm 1.5$  dB) is found to introduce supplementary phase inversions, which show up as extra zeroes in the output and sidelobes too low by 2 dB in the 11-bit code case.



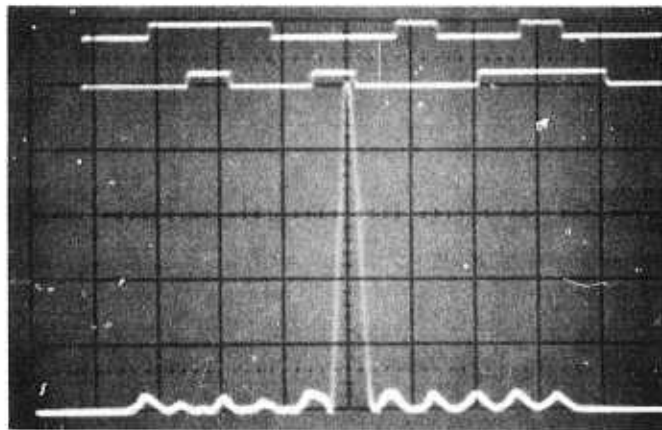


→ | ← 1  $\mu$ s

FIG. 3.2-1--V-FM chirp pulse compression



→ | ←  $1\mu s$



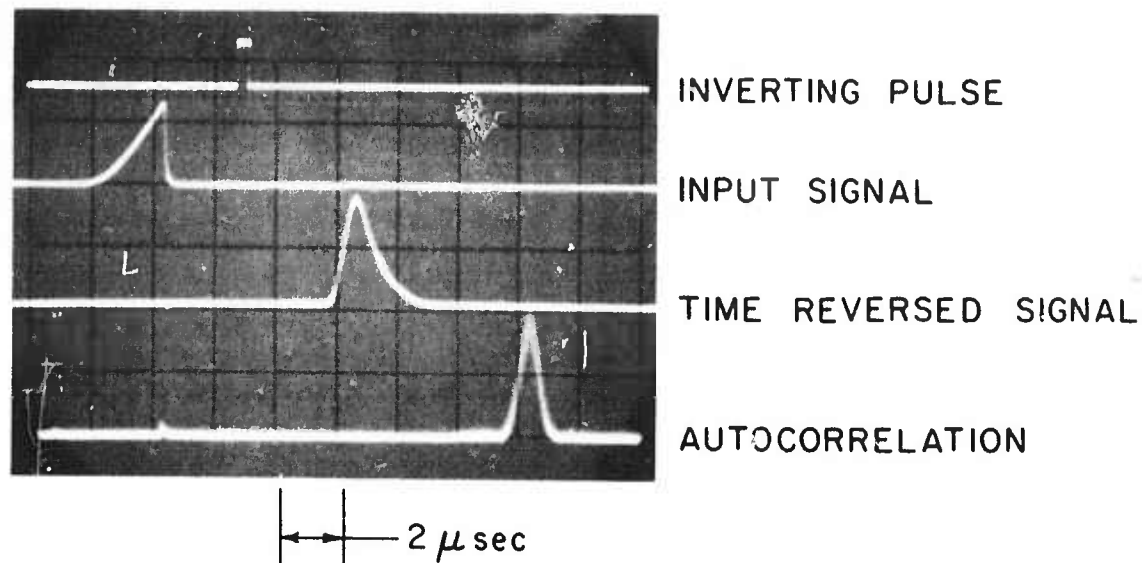
→ | ←  $0.5\mu s$

FIG. 3.2-2--7-bit and 11-bit biphase Barker code correlations.

To operate the acoustic convolver as a correlation filter, the reference signal has to be time inverted [see Eq. (3.2-1)]. The time inversion of digital codes is generally done by simply generating the inverted code, but the inversion of analog nonsymmetrical codes is more complex. The parametric convolver can also perform this task and true correlators can be built by cascading two devices.

While the input signal is entirely under the semiconductor, a  $\delta$ -function or short pip is applied on the semiconductor at twice the input frequency. Through the space charge nonlinearity, an idler is generated carrying the modulation of the input signal. Because of the phase relations between the pip ( $2\omega, k=0$ ) and the signal ( $\omega, k$ ), the idler propagates backward ( $\omega, -k$ ) and it will thus be an inverted replica of the input. Since the duration of the pip  $T_{\text{pip}}$  is small compared to the delay under the semiconductor,  $T_A$ , the efficiency of the device is reduced from  $F_T$  by a factor of  $(T_{\text{pip}}/T_A)^2$ . In the particular case shown in Fig. 3.2-3, the pip has a 3 dB width of 250 nsec and a peak power of 22 dBm,  $T_A = 5.5 \mu\text{sec}$  and  $F_T = -45 \text{ dB}$ ; the inverted signal is found to be 51 dB below the input. This is within 1 dB of the theoretically predicted 50 dB.

Because of the high efficiency of the semiconductor convolvers, it is possible to cascade two such devices and build a true correlator. This is illustrated in Fig. 3.2-3(b). A first device is operated simultaneously as a time inverter and a time delayer; the two signals are then convolved in a second device. The various waveforms are shown in Fig. 3.2-3(a) in the case of an asymmetrical triangle. The



(a)

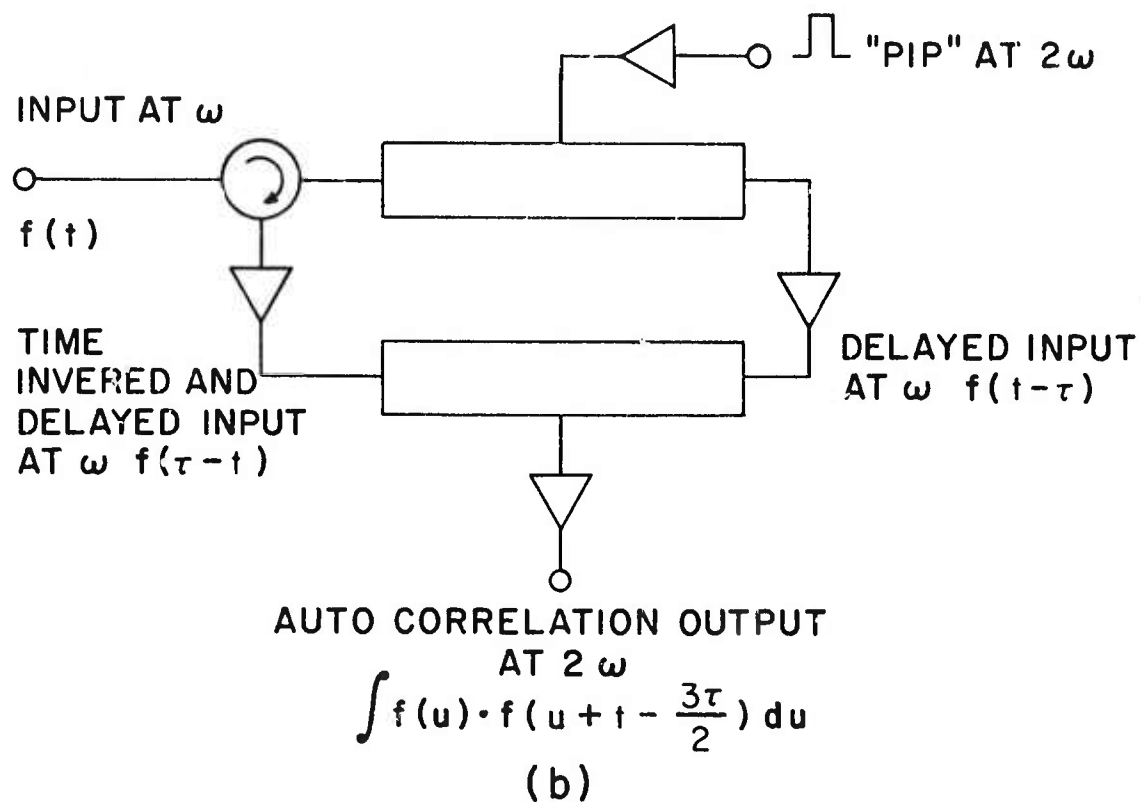


FIG. 3.2-3--Time inversion and autocorrelation of an asymmetrical triangle with acoustic device.

total insertion loss is approximately 80 dB, but, due to extra sources of noise, the dynamic range is limited to some 20 dB.

Among the other possible applications of the acoustic convolvers, let us mention the parametric amplifiers. We have attempted to build backward and forward propagating acoustic wave amplifiers of this type. Let us consider two forward propagating waves with frequency  $\omega_1, \omega_2$  and propagation constant  $k_1 = \omega_1/v(\omega_1)$ ,  $k_2 = \omega_2/v(\omega_2)$ , respectively, where  $v(\omega)$  is the surface wave velocity which is, in general, a function of frequency in a layered medium. As these waves propagate under the semiconductor, they are parametrically coupled and a third forward propagating wave is generated at the frequency  $\omega_3 = \omega_2 - \omega_1$  and with a propagation constant  $k_3 = \omega_3/v(\omega_3)$ . Another forward wave is also generated at the sum frequency but we shall not consider it here. If the three waves are well phase matched, i.e., if  $\Delta\varphi = k_3L - (k_2 - k_1)L$  is small, amplification of the third wave is possible with low input powers. Unfortunately, in the airgap structure, the gap introduces a very large dispersion;<sup>28</sup> for example, on  $\text{LiNbO}_3$  with a gap height of 1000 Å, the phase mismatch is as high as 140  $\pi/\text{cm}$  or 0.45  $\pi$  per wavelength when  $\omega_3 \sim \omega_1 \sim 100$  MHz and  $\omega_2 \sim 200$  MHz. Even with a gap of 5000 Å, the mismatch is still some 70  $\pi/\text{cm}$  (or 0.23  $\pi$  per wavelength). The threshold powers required for amplification are extremely high and practical devices are not feasible.

To avoid this difficulty, we have tried to operate the amplifier in the degenerate backward wave mode. In this mode, the input is a forward propagating wave at the frequency  $\omega_1$  and with propagation

constant  $k_1 = \omega_1/v(\omega_1)$ ; it is pumped by applying a spatially uniform signal at  $\omega_2 = 2\omega_1$  on the semiconductor. Through the parametric coupling, a backward propagating wave is generated at frequency  $\omega_2 - \omega_1 = \omega_1$  and with the propagation constant  $-k_1$ ; this wave grows sinusoidally with distance. This principle was tried out experimentally and a backward growing wave was detected. However, the system was unstable because of the difficulty of keeping the input signal and the pump in synchronism and at fixed frequencies. The smallest error introduces a phase mismatch and much larger pump powers are required to obtain amplification.

The dispersion problems of both the forward and backward wave parametric amplifiers can probably be eliminated with some effort. However, as the convolution and optical imaging devices appear to be of far more practical importance at the present time, we decided to investigate them further rather than concentrate on the problems of parametric amplification.

A more practical application is the Direct Fourier Transform of electrical signals, demonstrated by Otto.<sup>38</sup> A pulse compression experiment is set up in which the signal to be transformed modulates the amplitude of one of the chirps. The frequency scale on the output is a linear function of the chirp rate and can thus be varied. We shall not detail this process any further since a generalized approach to acoustic transforms will be described in the next chapter.

The parametric effects in the semiconductor-piezoelectric structure are not limited to those of the second order. The expansion in Eq. (2.2-5) can be carried out to higher order. The third-order

nonlinear term, in particular, allows for the coupling of three waves. We have demonstrated such a coupling by using the semiconductor convolver as follows. Two surface waves are launched in opposite directions at the same frequency  $\omega_1$ ; the corresponding input electrical powers are assumed to be equal to  $P_e^{\omega_1}$ . In addition, a spatially uniform potential is generated across the semiconductor by applying to the semiconductor electrode, a signal of frequency  $\omega_2$  and power  $P_e^{\omega_2}$ . Via the third-order nonlinearity, spatially uniform potentials are generated at the frequencies  $2\omega_1 \pm \omega_2$ . The corresponding detected powers are  $P_e^{2\omega_1 \pm \omega_2}$ . Since the same port is used to feed in some signals and to detect others, a careful filtering is required to avoid any stray mixing outside the semiconductor. In an experiment carried out to detect third-order effects, we used the device whose convolution characteristics are given in the first column of Table 3.1. The input frequencies are  $\omega_1/2\pi = 105$  MHz and  $\omega_2/2\pi = 195$  MHz. The nonlinear output is detected at  $(2\omega_1 - \omega_2)/2\pi = 15$  MHz. A small signal analysis predicts  $P_e^{2\omega_1 - \omega_2}$  to be of the form

$$P_e^{2\omega_1 - \omega_2} \propto P_e^{\omega_2} \times (P_e^{\omega_1})^2.$$

In fact, the output power is experimentally given by the relation

$$P_e^{2\omega_1 - \omega_2} \text{ mW} = 5.10^{-11} \cdot P_e^{\omega_2} \text{ mW} \times (P_e^{\omega_1} \text{ mW})^\alpha$$

where

$$\alpha = 1.614 - 0.175 \log (P_e^{\omega_2} \text{ mW}).$$



This expression shows a saturation mechanism which increases with the power applied to the semiconductor. By contrast, acoustic powers up to  $P_e^{\omega_1} = 25$  dBm did not contribute any further saturation effect. In any event, the amplitude of the third-order nonlinearity is fairly high and it can be the basis for a new type of signal processing device. For example, the acoustic surface waves can be used to scan a nonuniform electric field distribution at the frequency  $\omega_2$ , present at the interface between semiconductor and piezoelectric. If this field is set up by a bulk acoustic wave in the piezoelectric substrate, an acoustic imaging device could be built. Let us note, however, that in the case of an airgap device, a bulk wave impinging normally on the free surface of the piezoelectric material would not give rise to a strong normal component of electric field in the airgap.

CHAPTER IV  
OPTICAL SIGNAL PROCESSING AND IMAGING

4.1 INTRODUCTION

The coupling between acoustic wave and the semiconductor in the piezoelectric-semiconductor structure depends on the electronic properties of the semiconductor surface; specifically the conductivity and the surface state charge density. The former parameter affects the nonlinear convolution coupling and the propagation loss directly, the latter parameter controls the dc surface potential and hence, indirectly, the interaction strength. Because of the photoconductivity of the semiconductor, these surface parameters vary locally according to the intensity of any incident illumination on the semiconductor. The semiconductor can therefore play the role of an optical image sensor. In order to turn the device into an imaging system or, in other words, a solid state camera, one needs a scanning mechanism.

One of the simplest scanning mechanisms is schematically represented in Fig. 4.1-1(a). We denote by  $I(z)$  the optical intensity pattern illuminating the semiconductor. If  $f(t) \exp(j\omega t)$  and  $g(t) \exp(j\omega t)$  are the two input electrical signals, the convolver output is given by the integral

$$h(t) = \exp(2j\omega t) \int f(t - z/v) \cdot g(t + z/v) \cdot B(z) dz \quad (4.1-1)$$

where the nonlinear coupling coefficient is now a function of space

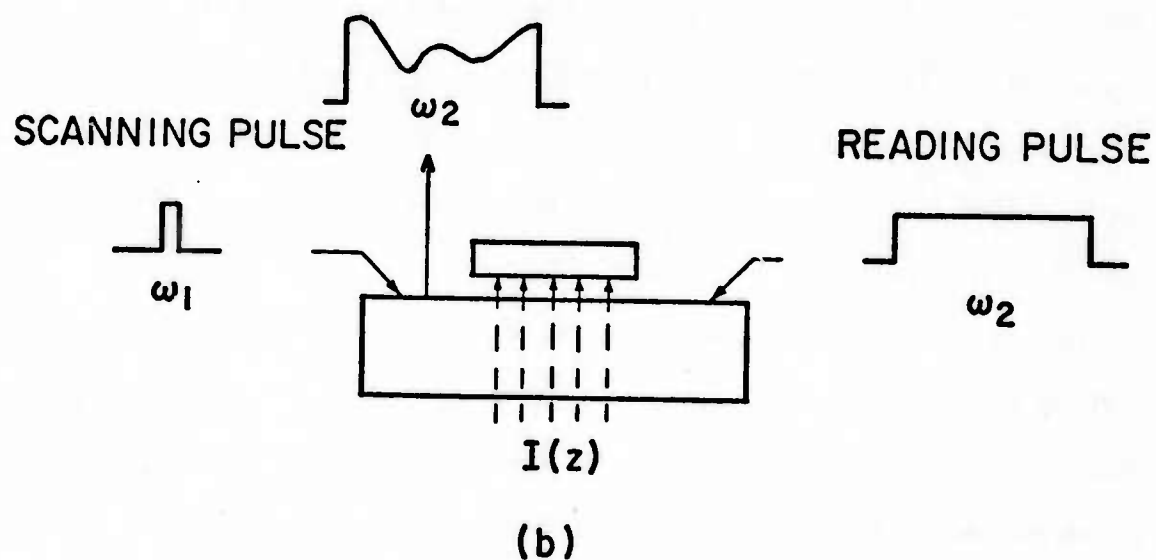
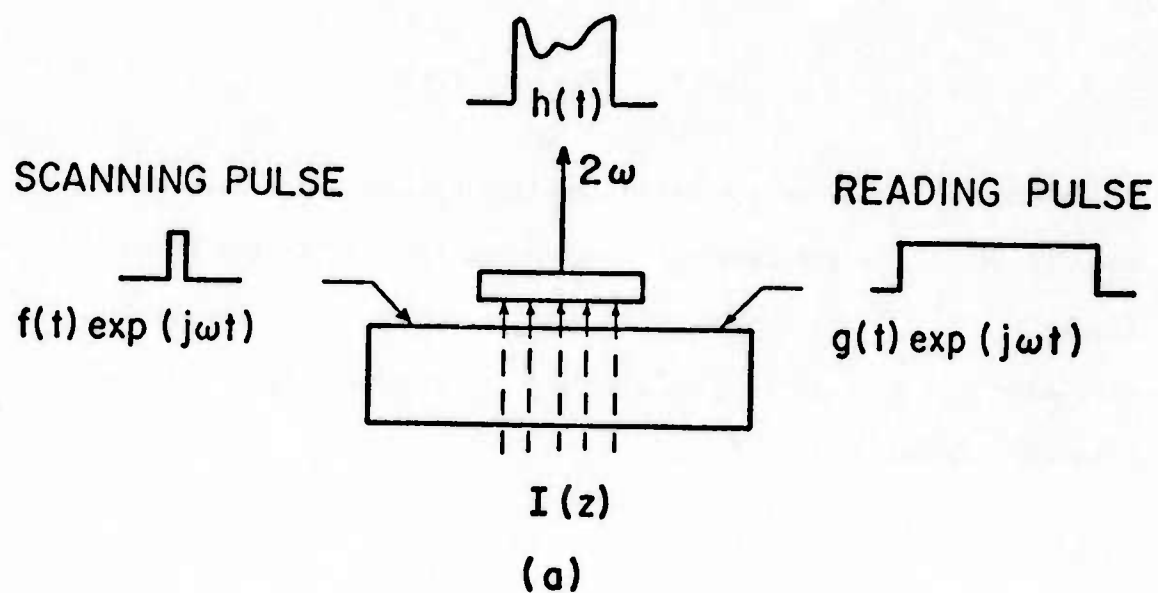


FIG. 4.1-1--Two techniques used for scanning optical images.  
 (a) The convolver technique with output at  $2\omega$ ;  
 (b) The Quate technique (reference 8).

$B(z)$  because of the illumination. To first order, we can write it as follows:

$$B(z) = B_0 + b \cdot I(z) \quad . \quad (4.1-2)$$

If we now let  $g(t)$  be a constant amplitude signal or a long pulse, and  $f(t)$  be a very narrow pulse which can approximate the Dirac function  $\delta(t)$ , the narrow pulse will, in effect, scan the semiconductor at the acoustic wave velocity  $v$  and the output will be given by the relation

$$h(t) = \exp(2j\omega t) \cdot v \cdot B(vt) = \exp(2j\omega t) \cdot v \cdot [B_0 + b I(vt)] \quad . \quad (4.1-3)$$

It follows that the image will appear as the modulation of the output waveform. Several other scanning schemes exist and they have been reviewed by Kino.<sup>54</sup> They either make use of the light dependence of the convolution effect as in the scheme just presented, or of the propagation loss introduced by the semiconductor. The first device built on this principle was due to Quate and his co-workers.<sup>8</sup> Its operation is represented in Fig. 4.1-1(b). They sent a long pulse, called the reading pulse, along the delay line under the semiconductor. This pulse was attenuated because of the presence of the semiconductor. A second narrow pulse, called the scanning pulse, was sent along the delay line in the opposite direction. When this pulse was present at a particular point, its interaction with the semiconductor changed the surface condition in this region, and hence the attenuation of the reading pulse. In addition, in the presence of light, the attenuation

depended not only on the amplitude of the scanning pulse but also on the carrier density at the point where the scanning pulse was present. Thus the amplitude of the reading pulse as a function of time depended directly on the spatial distribution of carrier density determined by the illumination of the image.

In all these systems, it will be noticed that there is an output even in the absence of illumination. In the presence of illumination, this output is modulated and the modulation should be of limited depth to conserve the linearity of the photodetection system. Thus the "dark current" is not too different from the "current" with illumination, and such systems have a small dynamic range. In addition, in all the imaging systems where a short pulse is used to scan the image, the resolution is limited by the width of the scanning pulse. The narrower this pulse, the better the resolution but the lower the input energy and the worse the output signal power. There will therefore be a trade-off between resolution and output signal-to-noise ratio. Finally, the scan rate of such systems is fixed and it is equal to the acoustic wave velocity.

In order to solve some of these difficulties and thus build a useful device, Quate and his co-workers made use of the storage in surface states and the variation of the decay time of these states with illumination to enhance the sensitivity of the imaging device. As we discussed in Chapter II, the properties of surface states depend very much on the surface preparation and they are difficult to control, especially when the surface of the semiconductor is left

unprotected from contamination. For these reasons, we decided not to use them and, instead, to take different approaches to eliminate all the difficulties mentioned previously.

The methods adopted are presented in the rest of this chapter, with the purpose of showing the various principles involved. In Section 4.2, we describe a simple means of lowering the "dark current" to arbitrarily low levels. A study of the dark current level is given and comparison between experiment and theory made. The dynamic range is then only a function of the photoconductivity of the semiconductor and of its effect on the nonlinear coupling. We have obtained dynamic ranges of 30 to 35 dB with a threshold illumination of 50 to 100  $\mu\text{W}/\text{cm}^2$ . Low illumination threshold operation ( $1 \mu\text{W}/\text{cm}^2$ ) was also obtained by using storage in surface states.

A detailed presentation of some of the processes, in particular, the carrier generation and transport in the illuminated semiconductor, is rather involved and would require a very extensive experimental study. The results presented here are not complete but with the help of Chapter II, they allow for a quantitative understanding of most of the phenomena involved in the modulation of the convolution efficiency by light and in the associated signal processing.

In Section 4.3 we show how, in the semiconductor convolver, we are able to obtain directly Fresnel and Fourier spatial transforms of the optical image. The original images are then reconstructed by carrying out the inverse transform. In the case of the Fresnel transform, this is done by inserting the output signal, which is in the form

of an rf chirp, into a dispersive delay line. In the case of the Fourier transform, a spectrum analyzer or a second convolver is used to obtain the inverse transform. The employment of such transforms gives a major improvement in signal-to-noise ratio because of the large scanning times used for one spot. Furthermore, these techniques allow for an arbitrarily narrow output bandwidth and an arbitrary scan rate. Such features are desirable for transmitting signals over links of limited bandwidth, for eliminating inessential information from a picture, and for differentiation against impulse noise. Several systems have been tested to verify these principles. With the device and signal characteristic used, the theoretical resolution limit of 0.25 mm has been achieved and two-dimensional pictures are presented.

#### 4.2 IMPROVED SENSITIVITY IMAGING DEVICE

The basic device used for optical imaging has been adapted from the one represented in Fig. 3.1-1. The piezoelectric is well polished on both sides in order to allow the light to reach the semiconductor active surface. In addition, the semiconductor surface is thermally oxidized to reduce the surface recombination centers and thereby increase the light sensitivity. Although BGO might have seemed a good choice for its good mechanical characteristics, it had to be rejected because of its very strong optical activity.<sup>55</sup> When a BGO crystal is illuminated, low mobility charges are induced within it and they oscillate at a low frequency which depends on the light



intensity and the presence of a dc electric field. These charges set up internal fields which are detected by the semiconductor and it is as if the interaction uniformity of the convolver were highly unstable.

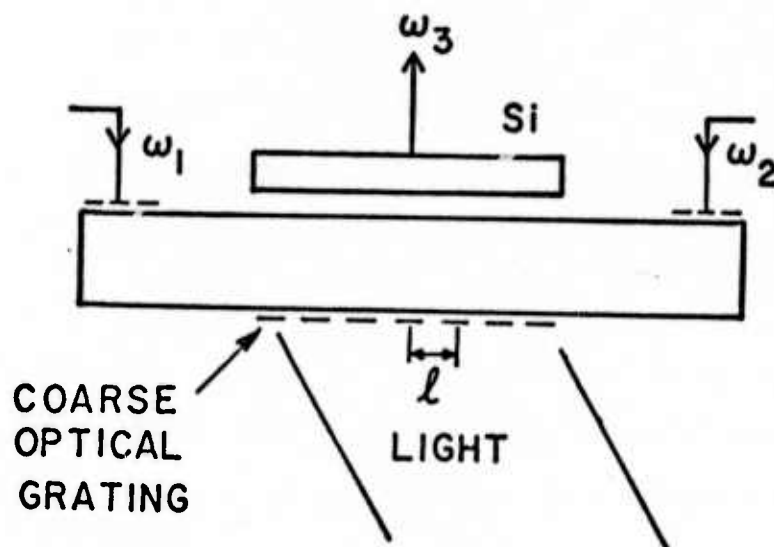
#### 4.2.1 Dark Signal Reduction - General Principle

Since the silicon used is photoconductive, illuminating it modulates the carrier density and hence the nonlinear coupling. The simplest way to read-out an image is to insert a narrow rf pulse, the scanning pulse, at one end and a long pulse at the other end of the delay line. The convolution output will be modulated and the output as a function of time corresponds to the illumination along one line of the image. One of the original difficulties of this system was its limited dynamic range because of the inherently high output with no light present (the dark current). To make the dark current very small, we passed the light incident on the semiconductor through a coarse optical grating of period  $\ell$ , as shown in Fig. 4.2-1. This, in effect, introduces a wavenumber  $K$  into the light beam, such that  $K\ell = 2\pi$ .

Now the optimum output is obtained with two input signals of frequencies  $\omega_1, \omega_2$ , propagation constants of  $k_1, k_2$ , respectively, such that

$$k_1 - k_2 = \pm K \quad (4.2-1a)$$

$$\omega_1 - \omega_2 = \pm Kv, \quad (4.2-1b)$$



$$Kl = 2\pi$$

$$k_1 - k_2 \pm K = 0$$

$$\omega_1 - \omega_2 = \pm K v$$

$$\omega_3 = \omega_1 + \omega_2$$

FIG. 4.2-1--Schematic of imager with low dark current.

where  $v$  is the velocity of the acoustic surface wave. By using a nondegenerate system with input frequencies  $\omega_1, \omega_2$  displaced by the amount given in Eq. (4.2-1b), a strong output is obtained when the device is illuminated, with a very small output when there is no light. Thus the "dark current" is caused to be very small. It should be noted that if three colored gratings of different periodicities are used, the device can be arranged to give outputs at three different frequencies corresponding to the three primary colors.

In order to evaluate the "dark current" reduction, we consider the input signals as being two square pulses of frequency  $\omega_1$  and  $\omega_2$ , respectively, and of duration  $T_A$  smaller than the delay under the semiconductor. Recalling the results of Section 2.1.1, and considering again the center of the semiconductor as the origin  $z = 0$ , the output convolution voltage is of the form

$$V = \exp [j(\omega_1 + \omega_2)t] \int \exp [j(k_1 - k_2)z] dz$$

where the integral is evaluated over the region of overlap of the two acoustic pulses. We find that  $V$  is given by the following expressions:

$$V = \exp [j(\omega_1 + \omega_2)t] \cdot \frac{v}{\pi \Delta F} \sin 2\pi \Delta F t \quad \text{for } 0 \leq t \leq T_A/2$$

$$V = \exp [j(\omega_1 + \omega_2)t] \cdot \frac{v}{\pi \Delta F} \sin 2\pi \Delta F (T_A - t) \quad \text{for } T_A/2 \leq t \leq T_A$$

(4.2-2)

where  $\Delta F = (\omega_1 - \omega_2)/2\pi$ .

Figure 4.2-2 shows the envelope of the output waveform for various values of the product  $\Delta F \cdot T_A$ . When  $\Delta F = 0$ , the output has a triangular shape; it extends for a time  $T_A$  and its maximum amplitude is  $v \cdot T_A$ . This is the usual result for degenerate convolution. When a frequency offset is introduced,  $\Delta F \neq 0$ , the output waveform is composed of two symmetrical portions of sine waves. For very small offsets in frequency satisfying the condition  $\Delta F \cdot T_A \leq 0.5$ , the amplitude is maximum at the center of the waveform and the maximum amplitude is  $v T_A \sin(\pi \Delta F \cdot T_A) / (\pi \Delta F / T_A)$ . As  $\Delta F$  increases, the maximum dark current becomes  $v T_A / (\pi \Delta F \cdot T_A)$ .

The reduction  $R$  in dark current brought by the introduction of the offset in frequency  $\Delta F$  is therefore

$$R = 20 \log (\pi \Delta F \cdot T_A) \quad (\text{dB}) \quad (4.2-3)$$

as soon as  $\Delta F \cdot T_A$  is greater than 0.5. If  $\Delta F \cdot T_A \leq 0.5$ , it will be seen that  $R$  is given by the relation

$$R = 20 \log \frac{\pi \Delta F \cdot T_A}{\sin(\pi \Delta F \cdot T_A)} \quad (\text{dB})$$

In this case,  $R$  is 4 dB or less, which is insufficient in practice. As a consequence, the only useful formula is given by Eq. (4.2-3).

The dark signal was measured with two devices operated in this nondegenerate mode. The input signals are square pulses of duration 3 or 4  $\mu\text{s}$ ; one of the input frequencies is fixed at 105 MHz; the other allowed to vary from 105 to 115 MHz. The results are plotted in Fig. 4.2-3 vs the frequency offset  $\Delta F$ . Also represented are the

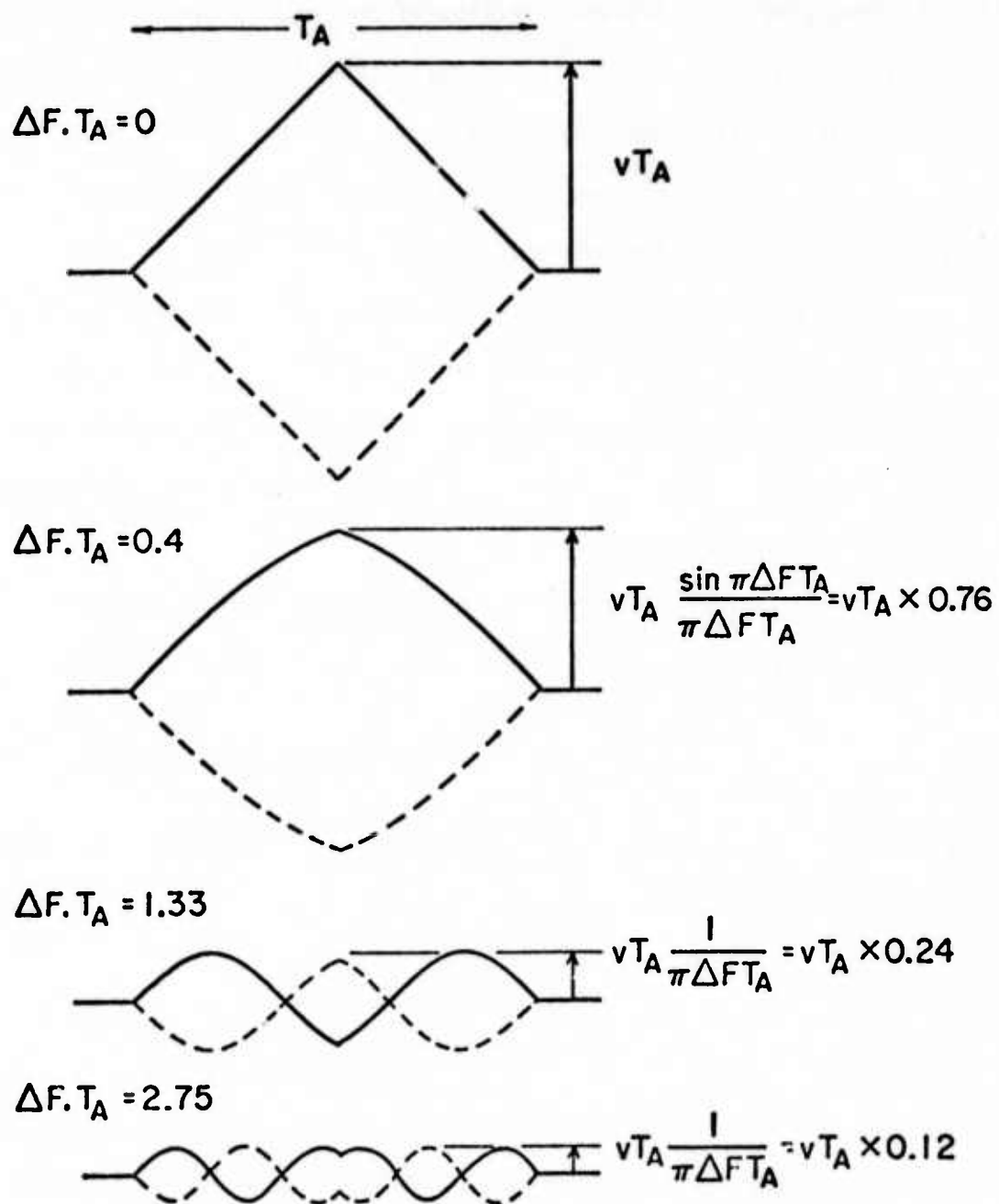


FIG. 4.2-2--Output convolution of two square pulses of duration  $T_A$  and whose center frequencies are offset by an amount  $\Delta F$ .

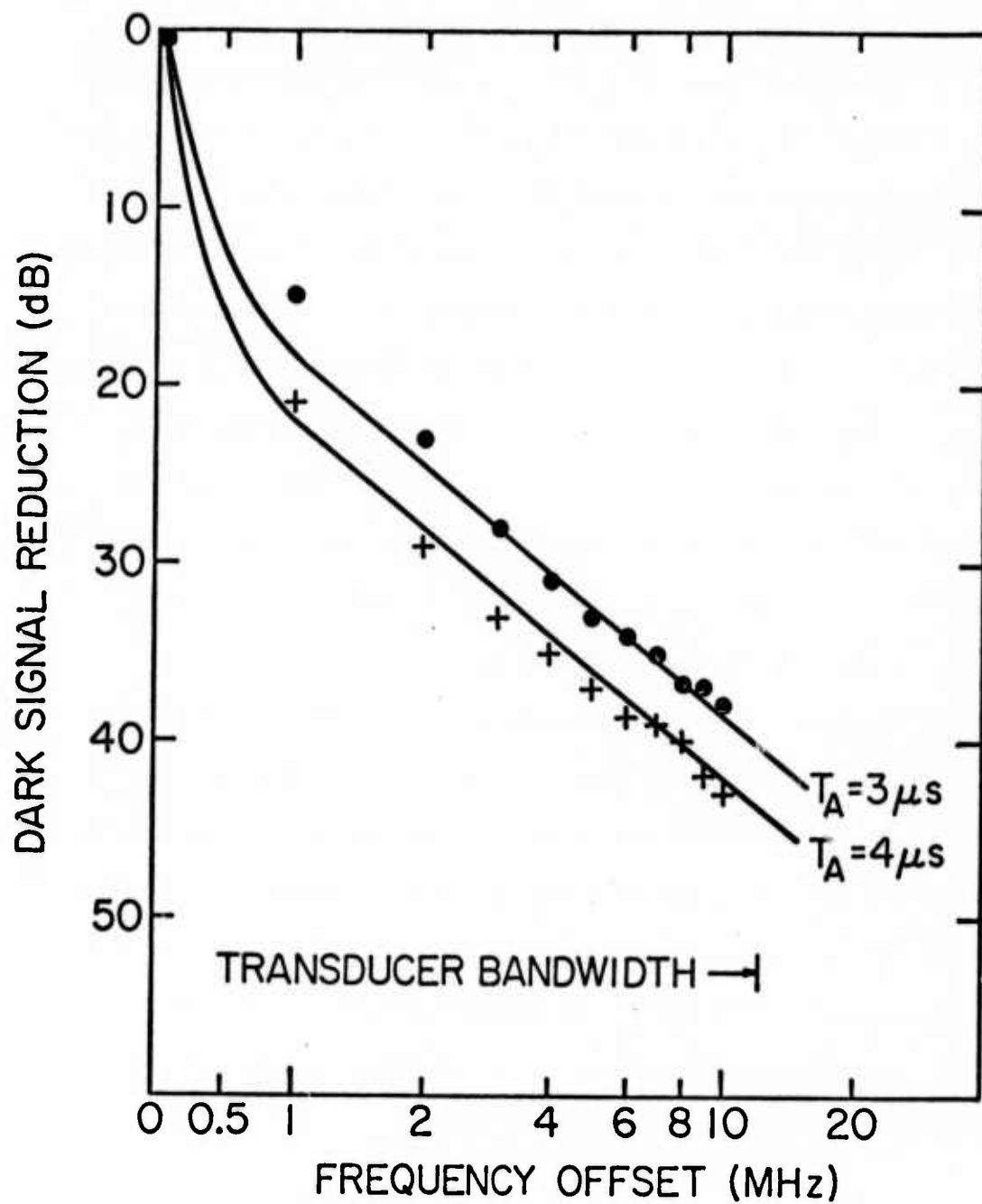


FIG. 4.2-3--Dark signal reduction due to a frequency offset. Two sets of experimental data are shown and compared to the theoretical curves (full lines).

theoretical variations for the two cases  $T_A = 3 \mu s$  and  $T_A = 4 \mu s$ . It will be seen that the experimental data are within 1 dB of the theoretical predictions. In addition, with  $4 \mu s$  square pulses and  $\Delta F = 10 \text{ MHz}$ , the dark signal reduction is 43 dB. The dark signal only decreases as  $1/\Delta F$  because of the relatively large high frequency components of the square pulses used. If a lower dark signal is required, one should reduce the spectrum of the inputs so that, when the offset is introduced, these spectra do not overlap. This is easily achieved by rounding off the edges of the pulses used. Ideally, if the spectra of the input signals are limited to  $20/T_A$ , these signals will still very much resemble square pulses but the dark current will be zero as soon as  $\Delta F$  is greater than  $40/T_A$ . If  $T_A = 4 \mu s$ , this means  $\Delta F > 10 \text{ MHz}$ .

The transducers used in these experiments have a center frequency of 108 MHz and a 3-dB bandwidth of 20 MHz. They will therefore introduce some extra loss when they are operated above 118 MHz or below 98 MHz. In order to avoid this further effect, we limited the experimental frequency range to 10 MHz and we fixed one of the input frequencies at 105 MHz. To accommodate larger frequency offset, transducers with unequal center frequencies are used as we shall see in Section 4.3.

#### 4.2.2 Light Sensitivity and Dynamic Range

In this sub-section, we give a more quantitative description of the effect of illumination on the behavior of the convolver. The principal process is the carrier generation in the semiconductor.



Depending on the surface condition prior to illumination, different types of phenomena can take place. A complete presentation is rather involved because of the difficulty of evaluating some of the optical parameters like the quantum efficiency and spectral response, and because the thermal equilibrium assumption does not hold when the semiconductor is illuminated.

As a first step, we study the case of a semiconductor at flat band or in the accumulation regime before the illumination is present. This mode is relatively simple and corresponds to the case of oxidized n-type silicon in the absence of bias. In this case, the light causes the carrier concentration to increase by an amount  $\Delta N$ . The dependence of the convolution on  $\Delta N$  is studied theoretically. By making simplifying assumptions, we derive the general form of  $\Delta N$ . Its magnitude, its dependence on the frequency offset, and the diffusion length in the semiconductor are presented and compared to experiments.

As a second step, we study the response to light of the imaging device as a function of the type of semiconductor used and the dc bias that may be applied to it. Experimental convolution vs light characteristics are discussed qualitatively on the basis of simple physical arguments.

#### Light sensitivity in flat band or accumulation case

Recalling the results of Chapter II, we find that the convolution output is made up of two terms: 1) the nonlinear coupling term (the  $\omega$ -value) which has been seen to be essentially inversely proportional to the free carrier concentration, when the semiconductor surface is at

flat band or accumulated, and 2) the propagation loss term which varies exponentially with the surface resistivity.

Let us now assume the semiconductor surface is either at flat band or in accumulation, so that we can define an equivalent surface concentration  $N$ . When the convolver is illuminated, electron-hole pairs are created and the electron carrier density is perturbed by an amount  $\Delta N$ , and the hole carrier density by an amount  $\Delta P$ . For a semiconductor at flat band, the carrier concentration remains uniform and we can write  $\Delta N = \Delta P$ . If the semiconductor surface is accumulated, internal fields exist in the material, the carrier concentration is not uniform and the relation  $\Delta N = \Delta P$  is not strictly true. In what follows, we shall be dealing mainly with weak accumulation corresponding to a surface potential of the order of  $q\phi_{s0}/kT = 1$  in the absence of light. The bulk of the semiconductor will stay at flat band under illumination and  $\Delta N = \Delta P$  there. By writing the expression for the total charge to be neutral, before and after illumination, we can evaluate the excess majority carrier concentration at the surface for a given excess in the bulk. The details of this calculation are not presented here. It can be shown that the excess carrier concentration profile in the semiconductor remains uniform to within 15 to 20%. The departure from uniformity is maximum for an excess carrier density equal to 5 times the bulk concentration in the dark. For lower and higher illuminations, the uniformity condition is almost verified. And in the following we shall therefore consider  $\Delta N$  as being uniform and equal to  $\Delta P$ .

In the experiments, the grating is composed of dark stripes  $m$  times wider than the white stripes; the spatial duty cycle is therefore  $a = 1/(m+1)$ . Because of the grating, the photon flux  $\Phi(z)$  varies from zero to  $\Phi_M$ . It can be expanded in the following Fourier series

$$\Phi(z) = \sum_{n=0}^{\infty} \Phi_n \cos(nKz) \quad (4.2-4)$$

where

$$\Phi_0 = a\Phi_M \quad \text{and} \quad \Phi_n = 2a \frac{\sin \pi na}{\pi na} \Phi_M, \quad n \neq 0.$$

The perturbation  $\Delta N$  can also be represented by a series as follows:

$$\Delta N = \sum_{n=0}^{\infty} \Delta N_n \cos(nKz). \quad (4.2-5)$$

The coefficients  $\Delta N_n$  are linearly related to  $\Phi_n$  through a factor  $F(nK)$  which accounts for the diffusion effects in the semiconductor. For small  $nK$ ,  $F$  is essentially constant and as  $nK$  increases, the diffusion becomes stronger and the corresponding perturbation in carrier density is reduced. An expression for  $F(nK)$  will be given later.

If two acoustic waves are propagating in opposite directions, when they reach any point under the semiconductor, the product of their amplitudes will have been attenuated by an amount given by the following expression:

$$\exp \left[ - \int_0^L \alpha_r(z) dz \right] \triangleq \exp(-\bar{\alpha}_r L)$$

where  $L$  is the total length of the semiconductor. The propagation loss is therefore not a function of position  $z$  but depends on the average illumination of the semiconductor. By contrast, the nonlinear coupling is going to depend on  $z$  and if  $\omega_1, \omega_2$  and  $k_1, k_2$  are the center frequencies and the propagation constants of the two acoustic waves, respectively, the output convolution signal appears at the frequency  $\omega_1 + \omega_2$ . Its amplitude is given by Eq. (2.1-4) to be  $V$  where

$$V \propto \exp(-\bar{\alpha}_r L) \int_{-L/2}^{L/2} \frac{\exp[j(k_2 - k_1)z]}{N + \sum \Delta N_n \cos(nKz)} dz \quad (4.2-6)$$

If the input signal center frequencies are identical,  $k_1 = k_2$  and the convolver is operated in a degenerate mode; it responds to the dc component of the inverse of the concentration; hence, for low level injection ( $\Delta N_n \ll N$ ), the output voltage is given by the following expression

$$V_{\text{deg}} \propto \exp(-\bar{\alpha}_r L) \cdot \frac{1}{N} \left( 1 - \frac{\Delta N_0}{N} \right) \quad (4.2-7)$$

In the high level injection mode, the high frequency component  $\Delta N_{n>0}$  will contribute to the dc component of  $1/(N + \Delta N)$ . A general evaluation requires a complete Fourier analysis. If we neglect the diffusion effects, the factor  $F(nK)$  is independent of  $nK$ .  $\Delta N$  will therefore follow exactly the photon flux; it will vary stepwise between zero and  $\Delta N_M$ . The inverse concentration varies stepwise between  $1/N$  and  $1/(N + \Delta N_M)$ . Its dc component is straightforward to

evaluate and leads to the following expression for  $V_{\text{deg}}[V(\text{degenerate})]$ :

$$V_{\text{deg}} \propto \exp(-\bar{\alpha}_r L) \frac{1}{N} \left( 1 - \frac{a \Delta N_M}{N + \Delta N_M} \right) . \quad (4.2-8)$$

If the input signal center frequencies are offset by  $\Delta\omega = \pm K\nu$ , the convolver only responds to one of the spatial harmonics of  $1/(N + \Delta N)$ ; and, in the low level injection case, the output voltage is proportional to  $\Delta N_1$  as follows:

$$V_{\text{non deg}} \propto \exp(-\bar{\alpha}_r L) \frac{1}{N} \frac{\Delta N_1}{2N} . \quad (4.2-9)$$

In the high level injection case and in the absence of diffusion, we find that

$$V_{\text{non deg}} \propto \exp(-\bar{\alpha}_r L) \frac{1}{N} \frac{a \Delta N_M}{N + \Delta N_M} \frac{\sin \pi a}{\pi a} . \quad (4.2-10)$$

To test the validity of the previous relations, we used the convolver whose characteristics were summarized in the first column of Table 2.3. The semiconductor is an epitaxial  $n/n^+$  silicon with an epi-layer concentration of  $7 \times 10^{20} \text{ m}^{-3}$  and an epitaxial layer thickness  $Y = 3 \text{ } \mu\text{m}$ . The epitaxial nature of the semiconductor was not important in the study of the convolution efficiency presented in Chapter II because the nonlinear process takes place in the first Debye length of the semiconductor. On the contrary, here, the thickness of the epi-layer plays an important role when light is shined at the semiconductor. The  $n^+$  substrate sets up a potential barrier which keeps the holes from flowing into the bulk. The hole current is therefore

zero at  $y = Y$ . In other words, all the minority carriers generated by the light are confined to the epi-layer. They can diffuse or recombine with electrons in the layer or at its surface. The diffusion length of holes in silicon is always much larger than the epi-layer thickness.<sup>22</sup> In addition, we saw in Chapter II that because of the presence of surface states, the surface of the semiconductor is naturally accumulated. This accumulation corresponds to a dc surface potential  $q\phi_{s0}/kT = 1$  in the absence of light and the surface majority carrier concentration is approximately  $19 \times 10^{20} \text{ m}^{-3}$ . This enhanced surface concentration reduces the surface recombination velocity<sup>26</sup> and we may neglect this effect. It follows that the excess hole concentration  $\Delta P$  will be almost uniform across the epi-layer. When steady-state is reached, we can equate the current generation due to the illumination, to the sum of the diffusion current along the surface and the recombination current in the epi-layer, thus writing

$$\Phi_n \eta \Gamma = \Delta P_n Y/\tau + (nK)^2 D Y \Delta P_n \quad (4.2-11)$$

$\eta$  is the quantum efficiency and  $\Gamma$  the absorption ratio in the semiconductor.  $\tau$  is the minority carrier lifetime and  $D$  the diffusion constant;  $\Delta N_n = \Delta P_n$  is the excess carrier concentration corresponding to the harmonic component of the flux  $\Phi_n$ . Equation (4.2-11) can be put in the final form

$$\Delta N_n = \Delta P_n = \frac{\Phi_n \eta \Gamma}{(nK)^2 D Y + Y/\tau} = \Phi_n F(nK) \quad (4.2-12)$$

which provides an expression for the factor  $F(nK)$ .

The light source employed is a tungsten filament lamp producing white light. The illumination power,  $P_{\text{light}}$ , was measured with a silicon photodetector and we estimated the maximum photon flux to be

$$\Phi_M = 4 \times 10^{18} P_{\text{light}} \text{ photons/m}^2/\text{s} , \quad (4.2-13)$$

where  $P_{\text{light}}$  is expressed in  $\text{W/m}^2$ . The maximum illumination obtainable corresponds to  $100 \text{ W/m}^2$ . (Typical room light illumination corresponds to approximately  $0.3 \text{ W/m}^2$ .) The quantum efficiency was assumed to be  $\eta = 0.5$  and the absorption coefficient  $\Gamma = 0.7$ .<sup>21</sup>

In a first experiment we used a grating with a duty cycle  $a = 0.5$  and corresponding to the small frequency offset  $\Delta F = 0.4 \text{ MHz}$  so that diffusion could be neglected. From Eqs. (4.2-4), (4.2-5), and (4.2-12), the excess electron concentration is found to be given by the relation

$$\Delta N_M = \frac{4 \times 10^{20} \times 0.5 \times 0.7}{3 \times 10^{-6} / \tau} = 4.67 \times 10^{25} \tau \text{ m}^{-3} . \quad (4.2-14)$$

On the other hand, we measured the decrease in degenerate convolution due to the illumination and we found  $-3.5 \text{ dB}$ . From Eq. (4.2-8), we can therefore write

$$20 \log \left( 1 - \frac{a \Delta N_M}{N + \Delta N_M} \right) = -3.5 .$$

This relation yields the value of the excess concentration:

$$\Delta N_M / N = 1.9 ,$$

which corresponds to high level injection. We saw earlier that



$N = 19 \times 10^{20} \text{ m}^{-3}$ , hence the value of  $\Delta N_M$ :  $\Delta N_M = 36 \times 10^{20} \text{ m}^{-3}$ .

And from Eq. (4.2-14) the lifetime necessary to fit the experimental data is found to be  $\tau = 77 \text{ } \mu\text{s}$ . The time  $\tau$  was also measured directly; the light is chopped at a fast rate and the rise time of the output waveform is measured. This method yields  $\tau = 70 \pm 10 \text{ } \mu\text{s}$ , which agrees well with the previous conclusion.

Knowing the value of  $\Delta N_M/N$ , we can now predict the level of the nondegenerate convolution in the presence of light, relative to the degenerate convolution in dark. This ratio comes from Eq. (4.2-10) and we obtain the result

$$\left. \frac{P_{\text{non deg w. light}}}{P_{\text{deg in dark}}} \right|_{\text{predicted}} = 20 \log \left( \frac{a \Delta N_M}{N + \Delta N_M} \cdot \frac{\sin \pi a}{\pi a} \right) = -13.5 \text{ dB} . \quad (4.2-15)$$

The directly measured value of this same ratio was  $-12.5 \pm 0.5 \text{ dB}$ . The fair agreement with the predicted value is a check of the consistency of the theoretical expressions given earlier.

Finally, the ratio defined in Eq. (4.2-15) was measured for various grating periodicities, i.e., various frequency offsets. In the experimental set-up, the grating is illuminated with a white light source of given power and the image of the grating is focused on the semiconductor by means of a lens. By changing the relative positions of the grating, the lens and the semiconductor, we vary the periodicity of the imaged grating. But, at the same time, the intensity of the illumination received by the semiconductor changes. Later, in conjunction with

Fig. 4.2-5, we shall discuss the variation of the nondegenerate convolution power with the illumination power; we shall see that with high illumination level, as is the case here, the convolution varies as  $P_{\text{light}}^{1.4}$ . With this added data, we can correct the measured values of the nondegenerate convolution power and hence normalize them to a given illumination level. This is what has been done and the results plotted in Fig. 4.2-4 are normalized to the illumination level corresponding to the frequency offset  $\Delta F = 1.75 \text{ MHz}$ .

As we have already discussed, for low frequency offsets, diffusion may be neglected. The nondegenerate convolution power output is independent of the offset; in addition, the excess carrier concentration is high and the "high level injection theory" should be used. For very large offsets, the excess concentrations are small because of the strong effect of diffusion; the low level injection approximation becomes valid and Eq. (4.2-9) can be used with  $\Delta N_1$  as given by Eq. (4.2-12). With this approximation, we obtain the theoretical variation denoted "low level theory" and shown in Fig. 4.2-4. The values of the diffusion constant and life time of the minority carriers (hole) we used are  $D = 6.3 \times 10^{-4} \text{ m}^2/\text{s}$  and  $\tau = 77 \text{ } \mu\text{s}$ , respectively. The experimental points are seen to be in good agreement with the previous conclusions, in the ranges where each of the two approximations holds. In the intermediary range, the diffusion effects are important but the low level injection approximation is not valid; several Fourier components in the expansion of  $\Delta N(z)$  should be kept. They are affected differently by diffusion according

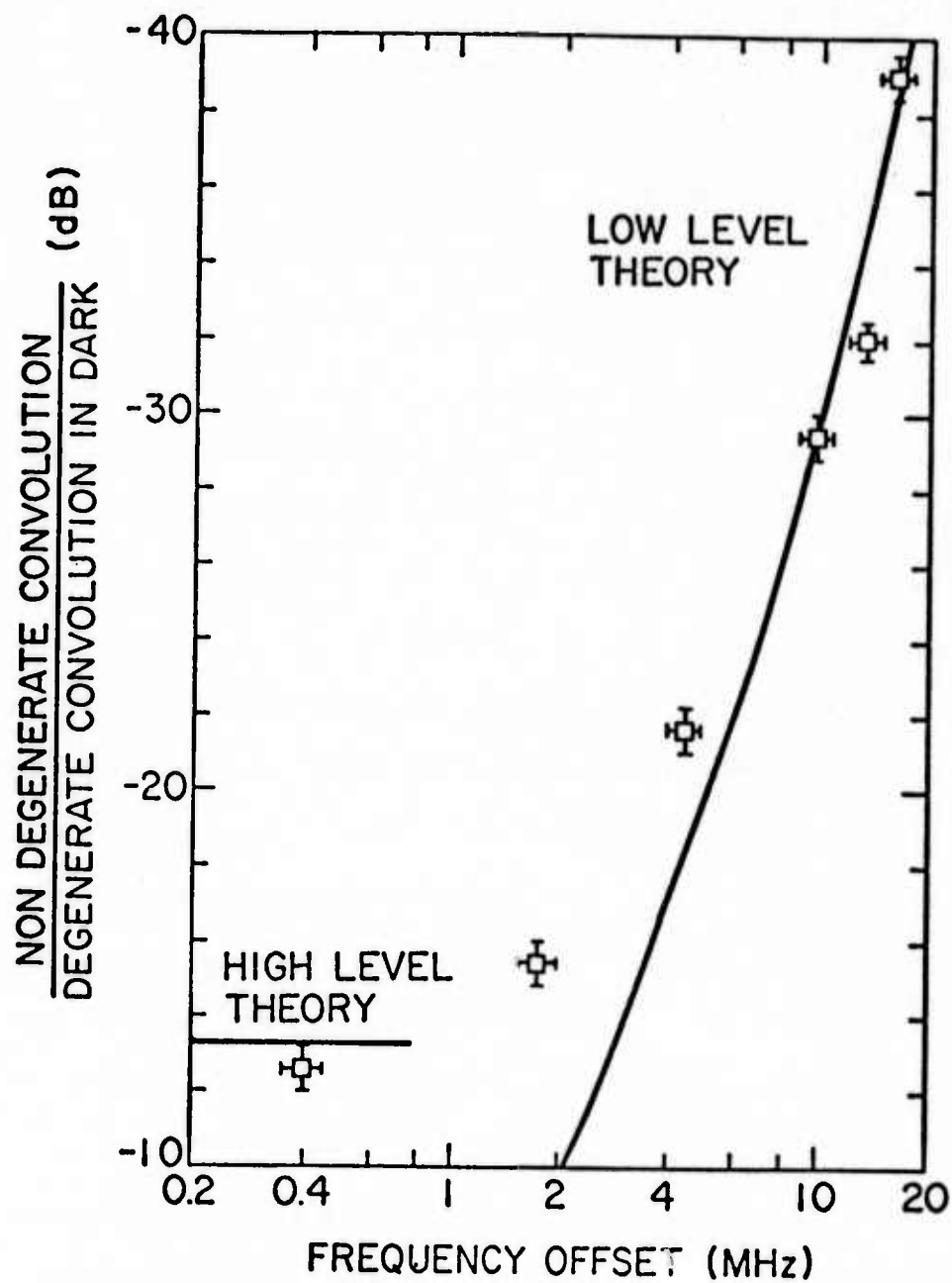


FIG. 4.2-4--Ratio of nondegenerate convolution power to degenerate convolution power in dark vs frequency offset for an  $n/n^+$  silicon sample under light accumulation conditions ( $P_{\text{light}} = 100 \text{ W/m}^2$ ).

to Eq. (4.2-12) and, in a rigorous study, one should use Eq. (4.2-6) to evaluate the nondegenerate convolution output. Had we conducted such a study, we would have been able to smoothly link the two theoretical curves of Fig. 4.2-4.

#### Dynamic range and light sensitivity

We define the dynamic range of the imaging device as the variation of the convolution output power when the illumination varies from the minimum detectable level to the saturation level. The minimum detectable illumination level is also called the threshold level. It is a function of the dark signal reduction since the lower the dark signal, the more sensitive the detection system and hence the lower the threshold level. It is also dependent on the sensitivity of the convolution phenomenon to any increase in carrier concentration in the semiconductor. These two features, the dark signal reduction and the sensitivity to carrier concentration increase, are functions of the periodicity of the grating as we saw earlier. But, in addition, the latter feature depends in a rather complicated fashion, on the nature of the semiconductor and its surface potential.

To examine this dependence, we have measured the nondegenerate convolution power as a function of the illumination. The plots corresponding to the n- and p-type silicon samples studied earlier (see Table 2.3) are shown in Fig. 4.2-5. The grating used has a duty cycle  $a = 0.25$  and the frequency offset is 10 MHz. In addition, the illumination was measured at the semiconductor, i.e., through the grating, and the illumination power used in Fig. 4.2-5 therefore corresponds to  $a \cdot P_{\text{light}}$ , with our definition of  $P_{\text{light}}$ .

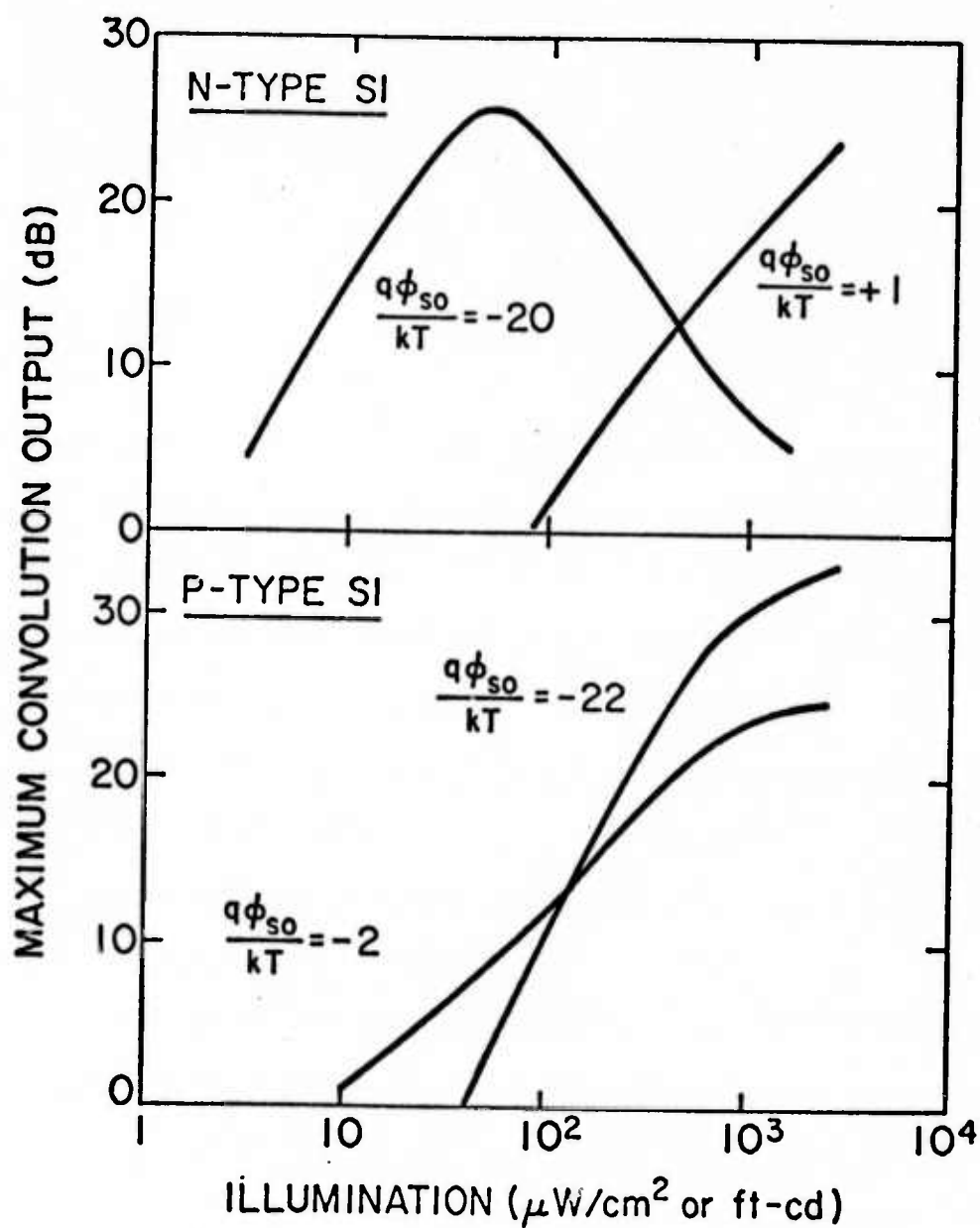


FIG. 4.2-5--Experimental convolution response to white illumination. The parameter  $q\phi_{so}/kT$  is the surface potential. The frequency offset is  $\Delta F = 10$  MHz. The grating duty cycle is  $a = 0.25$  and the illumination is measured through the grating, i.e.,  $P_{\text{light}} \times a$ .

In the absence of any biasing voltage, the n-type semiconductor has a slightly accumulated surface. We have studied earlier in this section, how the light affects the behavior of the device for a given illumination level. Figure 4.2-5 (top curve with  $q\phi_{s0}/kT = 1$ ) now shows the variation of the nondegenerate convolution with the light level: the threshold level is  $0.8 - 1.0 \text{ W/m}^2$  and the dynamic range 20 - 25 dB. In addition, for lower illuminations, the convolution shows a square law dependence on the illumination power, which is in accordance with Eq. (4.2-9) and Eq. (4.2-12); as the light increases, high level saturation occurs and the convolution power now varies as  $P_{\text{light}}^{1.4}$ . For an even higher illumination, the excess density  $\Delta N_M$  in Eq. (4.2-10), will go on increasing and we might expect  $V_{\text{non deg}}$  to level off and remain constant.

When the semiconductor is initially driven in strong depletion, rather different processes take place which allow for a much lower threshold illumination level. We consider the same silicon sample as previously, and we apply a bias voltage so that its surface potential becomes  $q\phi_{s0}/kT = -20$ ; a corresponding depletion layer is generated at the surface of the semiconductor with a width given by  $l = 6.3 \lambda_d = 0.94 \mu\text{m}$ . Under illumination, the minority carriers (holes) created in the depletion layer are pulled almost instantaneously toward the surface, under the influence of the large electric field present in the depletion layer. Concurrently, the electrons move toward the bulk of the semiconductor. Due to the presence of surface states, the holes will either be trapped or will recombine as they reach the surface. If  $\tau_{ss}$  is the life time for recombination at the surface, the mobile

hole charge at the surface per unit area is found to be  $\Delta P_s = G \cdot \tau_{ss}$ , where  $G$  is the generation rate of holes in the depletion layer, per unit area. Thus, if  $\tau_{ss}$  is large, and it can be several ms,  $\Delta P_s$  can be relatively large and the corresponding light sensitivity very high.

If we call  $\alpha_{ph}$  the attenuation constant of the light in the semiconductor, we find that  $\Delta P_s$  is given by the following expression:

$$\Delta P_s = \alpha_{ph} l 4 \times 10^{18} a \cdot P_{light} \cdot \eta \Gamma \cdot \tau_{ss} \quad (4.2-16)$$

where  $l$  is the depletion layer width. For lower illumination levels,  $\Delta P_s$  will be smaller than the total surface state density and a steady state is reached between light generation and surface trapping in which the traps are incompletely filled. We may rewrite Eq. (4.2-16) in the form

$$\Delta P_s = N_d \lambda_d g^+ \quad (4.2-17)$$

where

$$g^+ = \frac{\alpha_{ph} l 4 \times 10^{18} a \cdot P_{light} \cdot \eta \Gamma \cdot \tau_{ss}}{N_d \lambda_d} ; \quad (4.2-18)$$

$g^+$  is, as in Eq. (2.2-24), a measure of the "inversion" charge at the surface. The presence of the trapped charge will partially screen the dc bias field and reduce the depletion layer width. Since the effect of such a reduction on the convolution is minor (see Chapter II), we shall neglect this phenomenon here. On the contrary, by following the same argument as in Section 2.2, the surface charge  $\Delta P_s$  will reduce



the effect of the acoustic fields on the semiconductor. This reduction is characterized by the factor  $R$  defined in Eq. (2.2-27). It was seen to be dependent on  $g^+$ . The reduction in degenerate convolution and consequently the level of the nondegenerate convolution will therefore also depend on  $g^+$ ; furthermore we are going to see that, due to the large time constants associated with the surface states, the light sensitivity in this process is increased.

To put this result in quantitative terms, we refer to Fig. 4.2-5 (top half). For a given convolution output (say, 24 dB), we see that the illumination level  $aP_{\text{light}}$  required, is reduced from  $25 \text{ W/m}^2$  to  $0.3 \text{ W/m}^2$  when the semiconductor is driven into strong depletion. In this case, the variation in degenerate convolution between dark and light was measured to be -2.5 dB. The reduction factor should therefore be some 2.5 dB corresponding to  $g^+ = 2$ . By using Eq. (4.2-16) with  $l = 0.94 \text{ } \mu\text{m}$ ,  $\alpha_{\text{ph}} = 2 \times 10^5 \text{ m}^{-1}$ ,  $\eta = 0.5$ ,  $N_d = 7 \times 10^{20} \text{ m}^{-3}$ ,  $\Gamma = 0.7$ ,  $\lambda_d = 0.15 \text{ } \mu\text{m}$  and  $\tau_{\text{ss}} = 2 \text{ ms}$ , we find

$$g^+ = 1.5 \quad \text{and} \quad \Delta P_s = 1.5 \times 10^{13} \text{ m}^{-2}.$$

These results are in reasonable agreement with the predicted values. There is some inaccuracy in the determination of  $\alpha_{\text{ph}}$  and as a consequence, an inaccuracy in the number of electron-hole pairs actually generated. We also note that  $\Delta P_s$  is smaller than the total surface state density which had been found to be in the  $10^{14} \text{ m}^{-2}$  range.

As the illumination is increased, Fig. 4.2-5 shows that saturation occurs. This is mainly due to the complete filling up of the surface states and to the depletion layer reduction which follows.

Thus, eventually the output convolution will decrease.

Similar measurements have been made with bulk p-type silicon ( $100 \Omega\text{-cm}$ ) and the plots of the convolution output vs light are shown in the lower half of Fig. 4.2-5. With no bias, this silicon sample is somewhat depleted ( $q\phi_{s0}/kT = -2$ ). It exhibits a low threshold level ( $0.1 \text{ W/m}^2$ ). As the surface is driven into strong depletion (curve  $q\phi_{s0}/kT = -22$ ), the threshold level becomes higher but the light sensitivity is improved. By studying the pulsed bias response of the convolver, as we described in Chapter II, the surface state time constant has been estimated to be in the  $200 - 300 \mu\text{s}$  range compared to  $2 \text{ ms}$  in the case of the n-type silicon. The response of the system to light is a function of the minority carrier charge at the surface, itself proportional to  $G \cdot \tau_{ss}$  [see Eq. (4.2-16)]. Since  $\tau_{ss}$  has a reduced value, to obtain the same response, higher illumination levels, i.e., higher  $G$ , are required with the p-type silicon.

The presence of a strong surface depletion together with long life surface states therefore allows for large threshold level reductions and increase in sensitivity of the device. This feature, although interesting, relies on the properties of the surface states, which are difficult to control and to reproduce. In addition, when an MOS structure, like ours, is illuminated, low mobility charges are created in the silicon oxide, i.e., in slow surface states, and, under the influence of the dc field, dipoles are slowly formed. As a consequence, after illumination for some time, charges corresponding to the grating periodicity can be stored in the oxide, and the dark current reduction capability and hence the dynamic range of the system

are lost. This is because, even in the dark, a periodic (field) pattern is present in the system. Such an oxide storage mechanism took place in some of our experiments. The read-in time for such storage was some 10 to 20 minutes and the decay time of the storage was of the order of 1 or 2 days.

All the arguments presented here in conjunction with Fig. 4.2-5 are rather qualitative and simplistic. Nonetheless, they provide a fairly good understanding of the effect of light on a convolver using a semiconductor whose surface is at flat band or is slightly accumulated. They also lead to conclusions which are in reasonable agreement with experiments.

A more detailed study would certainly be of interest in order to predict more fully the behavior of the system as a function of the semiconductor surface condition. Such a study would require very careful measurements of the various characteristics of the convolver vs bias and light. In order to make repeatable experiments and to get rid of the difficulties we have encountered, the configuration of the experimental device should probably be altered. The major mechanical problems has to do with the presence of the airgap and its uniformity. It is evident that the smaller the semiconductor sample, the easier it is to maintain the uniformity of the gap. Hence in a physics oriented research project, smaller semiconductor samples could be employed with lengths of the order of 5 mm. One might then expect to obtain uniform interaction regions. The second main problem is related to the surface of the semiconductor and its passivation. Along all the steps of the preparation of the samples - cleaning, oxidation, scribing

or cutting, mounting - high standards of cleanliness must be obeyed to avoid contamination of the surfaces. Finally, even with these precautions, the semiconductor will remain in contact with the laboratory atmosphere. This will result in a long-term irreversible drift of the characteristics of the surfaces. This difficulty should be reduced if the experimental device is put together and kept under vacuum.

It should also be noticed that when a "dc" bias voltage is applied to the structure, stray effects may arise due to the motion of charges in the oxide, as we stated earlier. To avoid this phenomenon, the bias should be turned on for small periods of time and the measurement done rapidly. Finally, a study of the optical response should be done employing monochromatic light, so that the absorption constants and the illumination power be well defined. A study as a function of light wavelength is also very useful to determine the various optical transitions in the semiconductor.

From the results presented here, we have seen that a dynamic range of 20 - 25 dB with a threshold illumination level of  $1 \text{ W/m}^2$  are typical of the unbiased semiconductor convolver. Larger dynamic ranges, from 25 to 35 dB, can and have been obtained with a finer grating and an offset of 20 MHz. It should however be pointed out that increasing the frequency offset any further will not necessarily increase the dynamic range. The dark current decreases as  $(\Delta F)^{-2}$  but the response to light for large offsets decreases as  $(\Delta F)^{-4}$ . A finer grating is nonetheless required if high resolution imaging devices are needed (see Section 4.3). To increase the dynamic range beyond 35 dB, other methods would have to be used. A possible method is to

create, at the semiconductor surface, finely spaced potential wells to prevent the carrier diffusion and hence increase the Modulation Transfer Factor and the dynamic range. These potential wells can be created by deposition of Schottky barriers on the semiconductor or by using the buried layer technology now currently employed in Charge Coupled Devices.<sup>56</sup> By this method, the light sensitivity would also be increased because of the possibility of integrating the photo-injected charge over long times. This charge cannot diffuse and is therefore stored in the potential wells. This again is a concept used in the CCD devices.

#### 4.2.3 Example of "Direct" Imaging

One of the simplest optical imaging devices that can be built on the principles presented in the last two sections, is represented in Fig. 4.2-6(a). The object, in the form of a transparency, is projected through the piezoelectric substrate onto the semiconductor in the convolver. An optical grating in front of the object (a photographic transparency) introduces a spatial periodicity in the optical signal. Its effect on the interaction is cancelled out by introducing a relative offset  $\Delta F$  of the correct amount in the center frequencies of the two input signals. A narrow scanning pulse at frequency  $F$  is convolved with a long pulse at  $F + \Delta F$ ; the output at  $2F + \Delta F$  then corresponds to one line of the image.

An example of such a "direct" imaging with a narrow scanning pulse of  $0.15 \mu\text{s}$  width and a grating periodicity of  $350 \mu\text{m}$  ( $\Delta F = 10 \text{ MHz}$ ) is shown in Fig. 4.2-6(b). The object once reduced through the lens system is composed of 4 white stripes  $1 \text{ mm}$  wide and  $1 \text{ mm}$  apart. The input

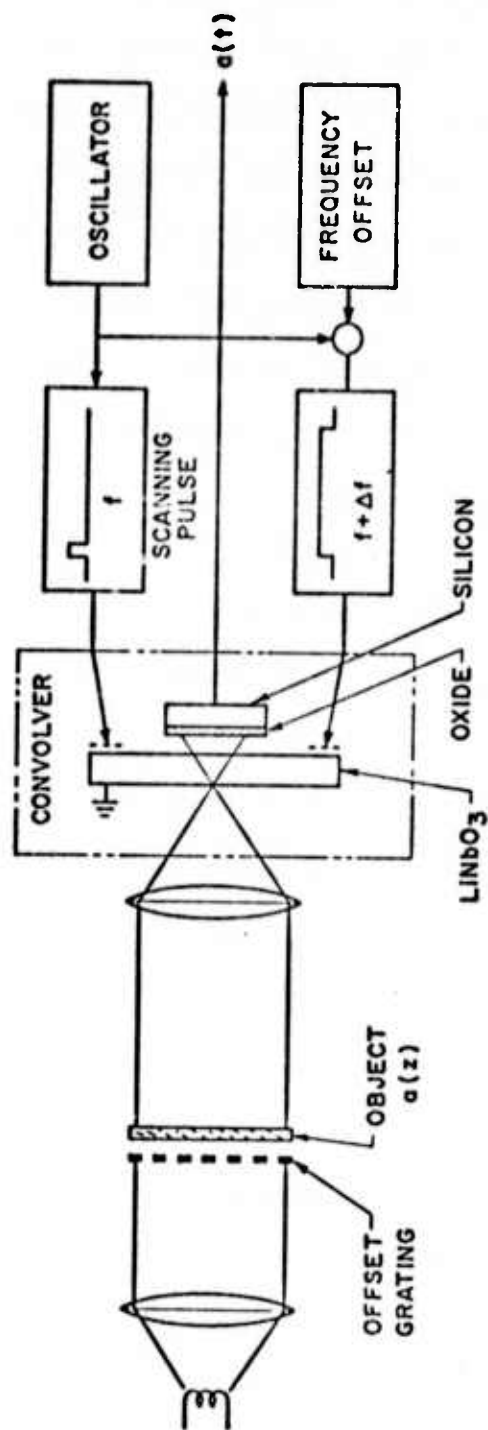
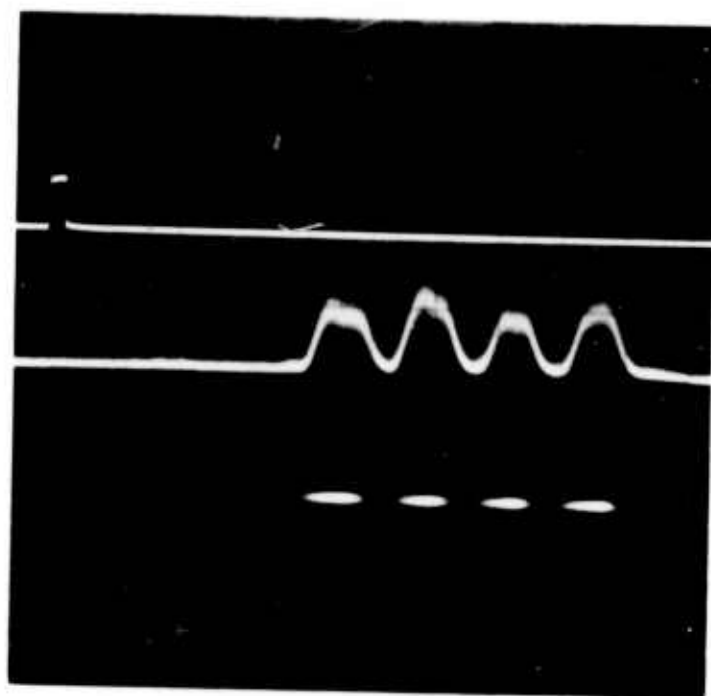


FIG. 4.2-6(a)--Schematic of the system used for direct imaging.



SCANNING PULSE  $.15 \mu s$

A-SCAN

B-SCAN

$\longleftrightarrow 0.5 \mu s$

FIG. 4.2-6(b)--Direct imaging of a 2 mm period pattern. Input frequencies 105 and 115 MHz.



frequencies are 105 and 115 MHz. The amplitude display of the output, called the A-scan image, shows in this particular example, a contrast of 15 dB. If this signal is used to modulate the intensity of the electron beam of a CRT, a B-scan is obtained. Both types of scans are shown in Fig. 4.2-6(b).

#### 4.3 TRANSFORM TECHNIQUES APPLIED TO OPTICAL IMAGING

So far we have discussed the simplest situation, that of a short pulse scan of the image. In this scan mode, a high resolution requires that the time taken to scan one spot in the image be short, which decreases the output power, and there is a trade-off between signal-to-noise ratio and resolution. We now consider the possibility of using more complicated waveforms of long-time duration (the line time) to scan one line of the image. In this case, the output will be a transform of the illumination distribution. If we feed this output into a correctly designed matched filter, as in radar systems, it is possible to obtain a short pulse signal corresponding to a spot in the image, i.e., to make an inverse transform of the scanning signal. As in radar, such matched filter pulse compression techniques give rise to an improvement in the signal-to-noise ratio because any spot in the image is now scanned for the line time rather than the spot time. Besides, according to the type of input signals used, generation of various transforms with different properties will be possible. As a goal, the chosen transform should reduce the correlation in the image so that the quantity of information to be transmitted is lowered and hence the required bandwidth. We have employed the Fourier and the

Fresnel Transforms because they are easiest to implement with simple linear FM chirp signals. Other digital and analog transforms are also of interest.<sup>58</sup>

#### 4.3.1 Spatial Fresnel Transform and Imaging

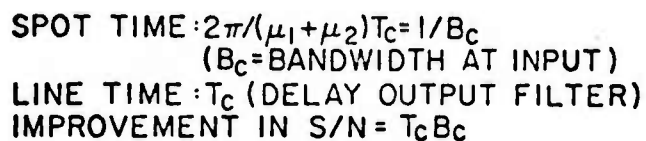
Let us consider the complete system represented in Fig. 4.3-1. Two linear FM chirp signals are inserted into opposite ends of the semiconductor device, with frequencies  $\omega_a = \omega_1 + \mu_1 t$ ,  $\omega_b = \omega_2 - \mu_2 t$ , respectively; they give rise to two waves with linear variation of frequency and a square law variation of phase. Using the center of the device as a reference, we find that the phase of the resultant product signal is

$$\phi(z, t) = \phi_a + \phi_b = (\omega_1 + \omega_2)t + (\omega_2 - \omega_1) \frac{z}{v} + \frac{\mu_1}{2} \left(t - \frac{z}{v}\right)^2 - \frac{\mu_2}{2} \left(t + \frac{z}{v}\right)^2. \quad (4.3-1)$$

With a grating filter with  $K = (\omega_2 - \omega_1)/v$ , the output signal due to a carrier density variation  $n(z)$  along the length of the devices, caused by illumination with light is

$$F(t) = e^{j(\omega_1 + \omega_2)t} \int n(z) e^{j \frac{\mu_1 - \mu_2}{2} \left(t^2 + \frac{z^2}{v^2}\right)} \times e^{-j(\mu_1 + \mu_2) \frac{tz}{v}} dz. \quad (4.3-2)$$

When  $\mu_1 \neq \mu_2$ , a Fresnel transform is obtained. In this case, a chirp output with a chirp rate  $\mu_1 - \mu_2$ , a chirp duration  $T_C$  and



- 128 -

a bandwidth  $B_s = (\mu_1 - \mu_2) T_C / 2\pi$  is obtained from one spot at  $z_0$  in the image [let  $n(z) = \delta(z_0)$  in the integral of Eq. (4.3-2)]. The image can be reconstructed by inserting the output signal into a suitably matched filter, matched to a chirp rate  $\mu_1 - \mu_2$ .

One advantage of the use of the grating filter is the elimination of spurious signals due to multiple reflections. The forward propagating wave, whose electric field varies as  $\exp[j(\omega_1 t - k_1 z)]$ , can be partially reflected by the end transducers or by the edges of the semiconductor, because of the electrical or mechanical discontinuities they introduce. A backward wave of amplitude  $\exp[j(\omega_1 t + k_1 z)]$  is therefore excited. The combination of these two waves will generate a nonlinear potential which varies as  $\rho \exp(2j\omega_1 t)$ . When the convolver is operated in a degenerate mode,  $2\omega_1$  is the frequency of the detected output and this spurious potential is detected. This signal corresponds to the autoconvolution product of the input at  $\omega_1$ . It is found to be  $-20 \log |\rho|$  dB below the true convolution output. By contrast, when the convolver is operated in a degenerate mode, only the potential which varies as  $\exp[j(\omega_1 + \omega_2)t \pm j(k_2 - k_1)z]$  are detected. The previously described spurious signal will therefore not interfere. The major disturbance now comes from the convolution product of the first reflections of the two input waves. Because two reflections are involved in the process, this spurious convolution signal is  $-40 \log |\rho|$  dB below the main signal. In practice  $-40 \log |\rho|$  is 40 or more, hence, multiple transit convolutions will not be a severe

problem for the nondegenerate system, consequently, signals of arbitrary length can, and have been used.

In Appendix A, a rigorous mathematical derivation of the entire process of obtaining an optical transform is given. It is shown how the chirped signals have to be chosen to achieve a given resolution. One conclusion is that if we suppose that the time length of the chirps is  $T_C$ , the minimum resolvable spot, defined as the distance between 4 dB points, equivalent to the Rayleigh criterion, is of length  $d_s$  where

$$d_s = 2\pi v / (\mu_1 + \mu_2) T_C = v / B_C . \quad (4.3-3)$$

Thus  $B_C$  is the total bandwidth of the chirps, or the bandwidth required for the pulse scan of the minimum resolvable spot. This does not take into account the resolution limitation implied by the optical grating. If the grating periodicity is  $\ell$ , and the frequency offset  $\Delta F = v / \ell$ , the resolution limit due to the grating,  $d_g$ , is of the order of one period, i.e.,

$$d_g \sim \ell = v / \Delta F . \quad (4.3-4)$$

Due to the nature of the input chirped signals used, the difference between the instantaneous frequencies of the two signals varies from  $\Delta F - B_C/2$  to  $\Delta F + B_C/2$ , where  $\Delta F$  is the center frequency offset to which the grating periodicity is matched. The dark signal reduction  $R(\Delta F) = 20 \log (\pi \Delta F \cdot T_A)$ , defined in Section 4.2.1, therefore depends on time. In order to keep the dark signal at a low level at all times, a suitable criterion is that  $R(\Delta F - B_C/2)$  does not differ

by more than 3 dB from  $R(\Delta F)$ . It follows that  $B_C$  should not exceed  $\Delta F$ . Referring back to Eqs. (4.3-3) and (4.3-4), we conclude that the resolution limit introduced by the grating is comparable to the limit inherent in the transform system  $d_g \sim d_s$ . The grating will, in addition, have the effect of widening the apparent width of small details by an average of one half period  $l/2$ . The practical minimum resolution is therefore approximately  $d_s \approx 1.5 l$ .

Another result derived in Appendix A is that the effective scan velocity along the convolver becomes

$$v_s = v(\mu_1 - \mu_2)/(\mu_1 + \mu_2). \quad (4.3-5)$$

Thus an arbitrary scan velocity can be obtained. The number of resolvable spots is still  $N = L/d_s$ , where  $L$  is the length of the imaging device.

It is also shown in Appendix A that the optimum signal-to-noise ratio improvement in using this matched filter chirped scan is equal to the time bandwidth product of system, or

$$G = N(B_C/B_s) = N(v/v_s) = T_C v/d_s = T_C B_C. \quad (4.3-6)$$

There is an improvement of  $B_C/B_s$  because the bandwidth of the noise entering the matched filter is decreased by that factor, and there is a factor  $N$ , the number of resolvable spots which arises because of the large increase in the time spent obtaining a signal from one particular spot in the image.

For a TV line with  $T_C = 60 \mu\text{sec}$ ,  $B_s = 5 \text{ MHz}$ ,  $N = 300$ , we would use an acoustic device with a delay of  $T_A = 6 \mu\text{sec}$  and a

chirp bandwidth  $B_C = 50$  MHz ; the signal-to-noise ratio improvement would be  $60 \times 50$  , i.e., 35 dB.

Several experiments have been conducted with the same optical arrangement as in Fig. 4.2-6. In a first stage, we used a grating filter with a periodicity of  $350 \mu\text{m}$  ( $\Delta F = 10$  MHz) and the suboptimal figures  $T_C = 20 \mu\text{s}$  ,  $T_A = 4 \mu\text{s}$  ,  $B_s = 1.5$  MHz,  $B_C = 7.5$  MHz leading to a theoretical 30 point resolution. The dispersive filter was an acoustic strip line waveguide with a total dispersion of  $40 \mu\text{s}$  over 3 MHz. Half of the dispersion, i.e.,  $20 \mu\text{s}$  over 1.5 MHz, was actually used in these experiments. Examples of pictures taken with this device, by mechanically scanning in one direction, are shown in Fig. 4.3-2. The number of lines is approximately 20 and the experimental resolution approximately 30 points, i.e.,  $d_s = 0.5$  mm . This was determined by noticing that the center portion of the "A" of "TAC" is well detected. This portion measures 0.5 mm and the total field of view is 14 mm wide. The output signal-to-noise ratio is 20 dB but nonuniformities in the interactions region and in the response to light limit the grey scale dynamic range of the picture.

In a later stage, we built a convolver whose input interdigital transducers have 3 dB bandwidths of  $108 \pm 11$  MHz and  $134 \pm 20$  MHz, respectively. A different grating of periodicity  $175 \mu\text{m}$  was used, allowing for a frequency offset  $\Delta F = 20$  MHz . With this larger offset, it is possible to increase the chirp bandwidths and hence the resolution. Examples of two-dimensional pictures taken with this new system are shown in Fig. 4.3-3. The chirp parameters are





FIG. 4.3-2--Pictures taken with the system shown in Fig. 4.3-1. The chirp excursions are 4.5 and 3.0 MHz for 20  $\mu$ s, the resolution is approximately 30 points, the number of lines is approximately 20.



(a)



(b)



(c)



(d)

FIG. 4.3-3--(a) Two-dimensional picture taken with the Fresnel transform imaging system. The chirp excursions are 9.8 and 7.6 MHz for 25  $\mu$ s. The minimum resolvable spot is  $d_g \sim 0.25$  mm (50 points).

(b),(c),(d) Effect of bandwidth limitations of the Transform signal on the reconstituted image.  
 (b) no limitation; (c) suppression of the lower frequencies; (d) suppression of the higher frequencies.

as follows:  $T_C = 25 \mu s$  ,  $B_C = 17.5 \text{ MHz}$  ,  $B_s = 2.1 \text{ MHz}$  and  $T_A = 3.5 \mu s$  (corresponding to 12.5 mm of semiconductor actually being used). The minimum resolvable spot is then  $d_s = 0.20 \text{ mm}$  and the number of points is 50. Referring to Fig. 4.3-3(a), the center triangle of the letter "A" is seen to be well resolved. Since its base is 0.65 mm we can indeed estimate the minimum resolvable spot at 0.2 mm. The resolution limit implied by the grating is slightly higher,  $d_g = 1.5 \times 0.175 \text{ mm} \approx 0.25$  .

With this resolution,  $d_g \approx 0.25 \text{ mm}$  , and 3 cm long silicon samples, it is possible to obtain pictures with a 120 point resolution. The uniformity of the interaction under such long samples requires a technology to keep the airgap uniform;<sup>50</sup> in addition, the projected images have to be free of aberrations. If the object is a standard 35 mm slide, the projection ratio is close to one so a good "relay" lens must be used and the illumination of the object has to be uniform. A diffuser in front of the light source will achieve this uniformity simply.

In the Fresnel transform signal, each spot of the object is represented by a chirp whose center frequency is a linear function of the position of the spot and whose excursion is fixed and equals  $B_s$  [see Appendix A, Eq. (A-4)]. If this signal, i.e., the output of the convolver, is fed into a bandwidth-limited filter, the portions of the reconstituted image corresponding to the suppressed frequencies will be lost, in addition, the chirp excursion will be reduced and the compression that takes place in the matched filter will not be as efficient; therefore the quality of the image worsens, the resolution decreases [see Eq. (A-14)], and so does the signal-to-noise ratio [see Eq. (A-19)]. Experimental demonstration of this phenomenon is

shown in Fig. 4.3-3 (b,c,d). In Fig. 4.3-3(b), the total output bandwidth  $B_s = 2.1$  MHz is not limited; in (c) the lower 0.5 MHz of the spectrum is cut-off, and in (d), the upper 0.7 MHz are cut-off. As predicted, portions of the image are lost and the image quality is somewhat deteriorated. In Fig. 4.3-3(b,c,d), the vertical synchronization is not as good as in Fig. 4.3-3(a), and this accounts for the vertical blur.

#### 4.3.2 Spatial Fourier Transform and Imaging

When we let  $\mu_1 = \mu_2 = \mu$  in Eq. (4.3-2), the output as a function of time is the spatial Fourier transform of the carrier density, and hence of one line of the image. A more physical view of the process is schematized in Fig. 4.3-4. The variation of the propagation constant  $k^{(1)}$  and  $k^{(2)}$  of the two acoustic pulse waves are represented as functions of position at a given time  $t$ . The difference  $\Delta k$  between the propagation constants is found to be given by the relation

$$\Delta k = k^{(2)} - k^{(1)} = -2\mu t/v \quad . \quad (4.3-7)$$

It is seen to be invariant with  $z$ ; so the output electrode picks the Fourier component with the spatial frequency  $\Delta k$ . The output is given by a relation of the form

$$V_{op} = \int n(z) \exp(j\Delta k z) dz = \int n(z) \exp\left(-2j \frac{\mu t}{v} z\right) dz \quad , \quad (4.3-8)$$

where  $n(z)$  represents the nonlinear coupling variation along the semiconductor. Here  $n(z)$  corresponds to the optical image focused

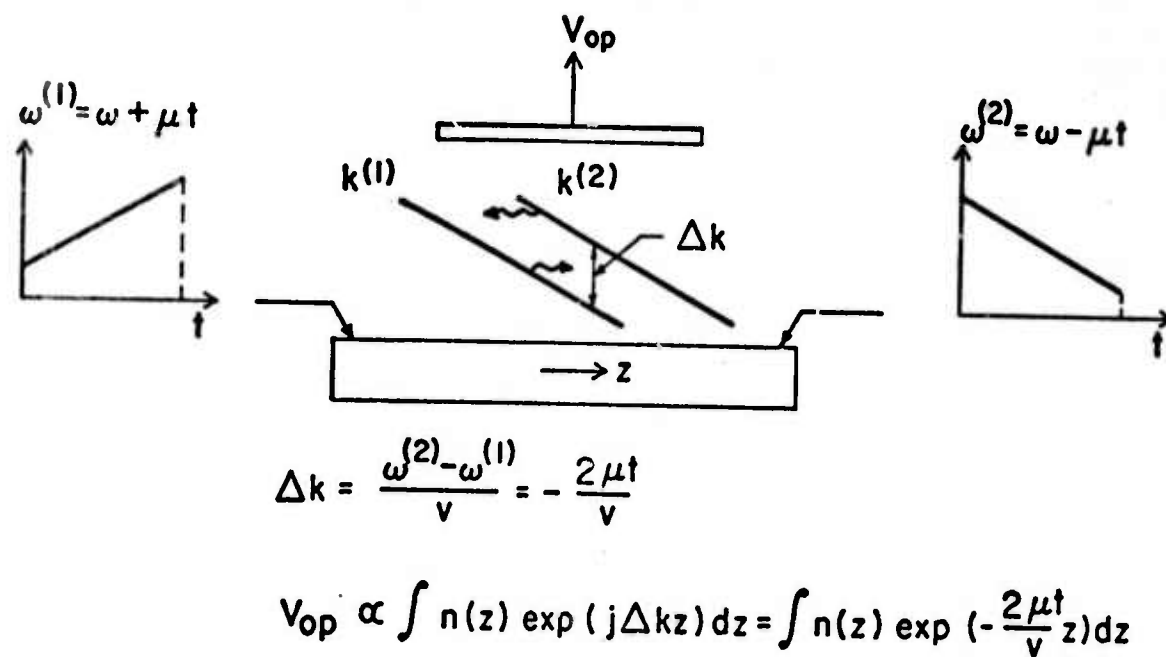


FIG. 4.3-4--Principle of the generation of the Fourier Transform in a convolver.

on the semiconductor. By using an acoustic convolver,<sup>38</sup> or a spectrum analyzer, and inserting this signal in the proper way, an inverse Fourier transform of the input signal can be obtained, and hence the original image signal recovered. This device offers the further important advantage that it tends to differentiate against impulse noise because impulse noise modulation of the Fourier transform signal gives rise to a uniform background on the image rather than points of light.

An acoustic convolver can be utilized to take the Direct Fourier transform of an electrical signal. The first demonstration of this operation was done by Otto.<sup>38</sup> Two linear FM chirps of opposite slopes are fed into the convolver and the signal to be analyzed, modulates the amplitude of one of the chirps. If we call  $f(t)$  this signal, the convolution output is given by an expression similar to Eq. (A-20)

$$h(t) = \exp(j\omega_3 t) \int_{-L/2}^{L/2} f(t - z/v) \exp(-j2\mu t z/v) dz \quad (4.3-9)$$

with the change of variable  $\tau = t - z/v$ , and the notation  $L/v = T_A$ ,  $h(t)$  can be put in the following form:

$$h(t) = \exp[j(\omega_3 - 2\mu t)t] \int_{t-T_A/2}^{t+T_A/2} f(\tau) \exp(-j2\mu t \tau) d\tau \quad (4.3-10)$$

The integration process taking place in the convolver is seen to be identical to the one of a spectrum analyzer. It is to be noted that when the integration is completed, the exponent  $-2\mu t^2$  drops out, so  $h(t)$  represents the Direct Fourier transform of  $f(t)$ .

Appendix A gives a derivation of the Fourier transform imaging process. It is shown that the values of the resolution, the scan

velocity and the signal-to-noise ratio enhancement are still given by Eqs. (4.3-3), (4.3-5), and (4.3-6), where the filter chirp rate  $\mu_1 - \mu_2$  is replaced by the spectrum analyzer internal frequency scanning rate  $a$ . It will be noted that in this case, the chirp lengths can, in principle, be arbitrarily long, while the total input bandwidth is dictated by the resolution required. The output bandwidth from the device, however, is reduced by the ratio of the delay time  $T_A$  in the convolver to the length of the chirp  $T_C$  (the scan time). We have carried out several experiments to demonstrate these principles and check these theoretical results.

A first example is illustrated in Fig. 4.3-5. A grating filter with a  $350 \mu\text{m}$  period is used in front of the device to give good dynamic range, approximately 25 dB. An object consisting of a photographic transparency is also placed in the path of the incident light, and a signal corresponding to the Fourier transform of the object is produced as shown in Fig. 4.3-6(a). In this case, the input signals are 10 ms long chirps of opposite sign with center frequencies of 115 and 105 MHz, and frequency excursion of 2.5 MHz. In the example shown, we used a simple 7 period grating with a periodic spacing of approximately 2 mm as the illuminated object, and displayed the output amplitude as a function of time, as shown in the figure. The center peak corresponds to the zero spatial frequency component and the two main lobes to the periodicity of the grating.

Using the very slow scan, the simplest way to reconstitute the image is with a spectrum analyzer. The output from the spectrum analyzer is shown in Fig. 4.3-6(b), and is seen to correspond well to



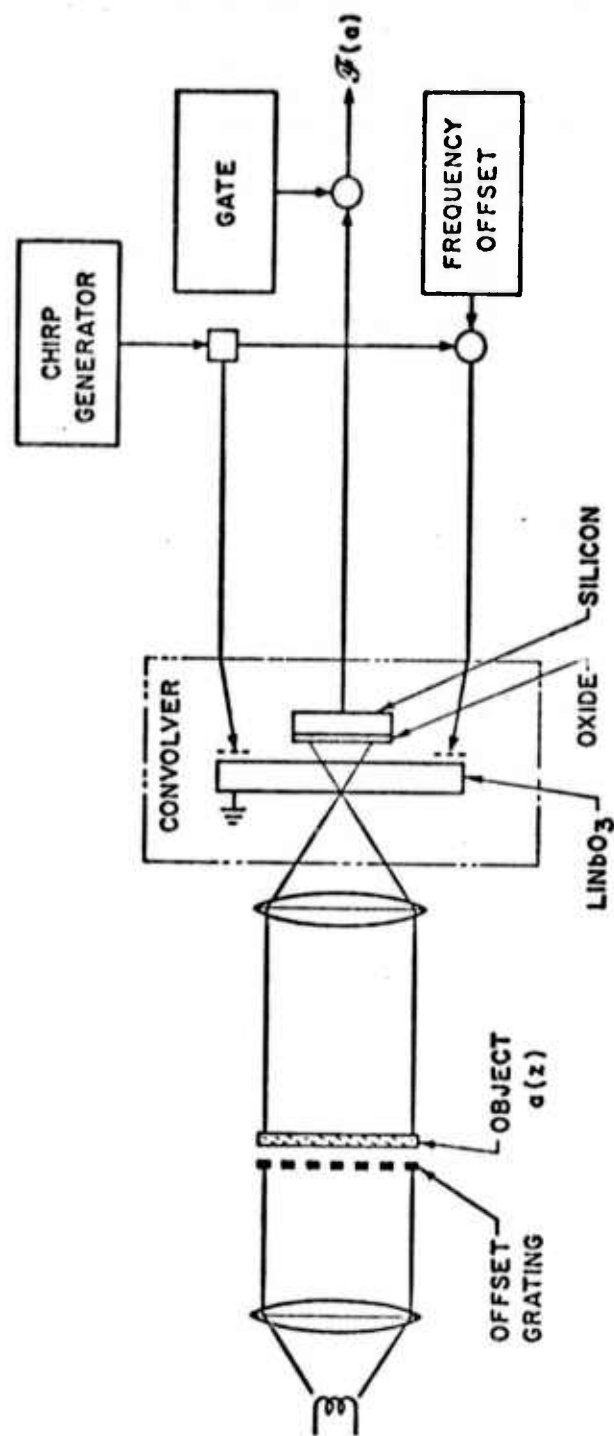
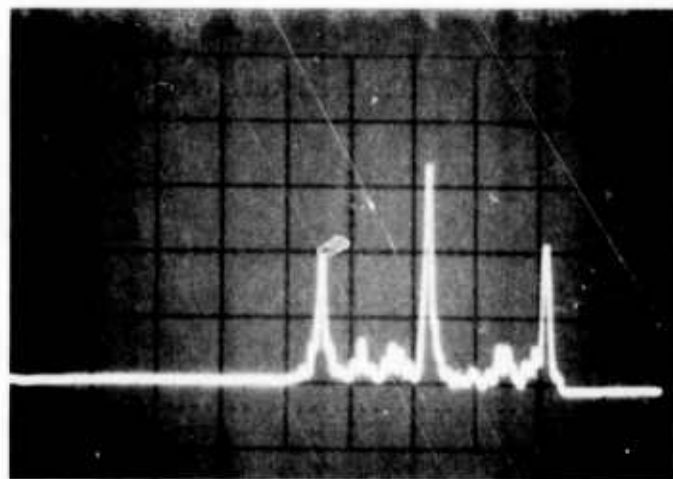


FIG. 4.3-5--Schematic of the system used for taking a Fourier transform.

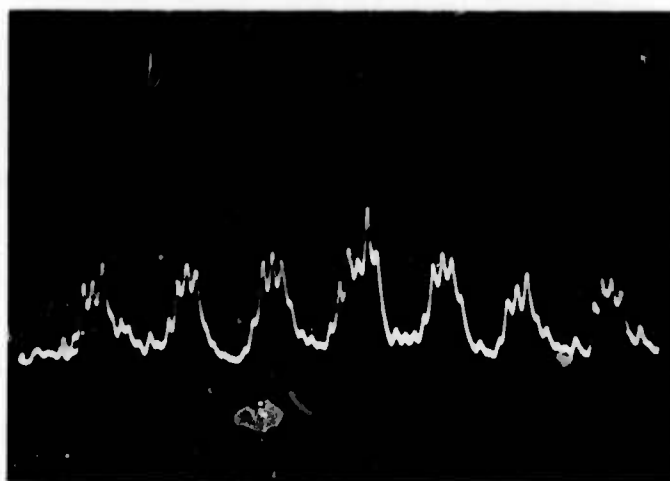


(a)

FOURIER TRANSFORM

→ | ← 2 ms

FIG. 4.3-6(a)-- A Fourier transform of a periodic grating with a period of 2 mm. A grating filter of  $350\text{ }\mu\text{m}$  spacing was used with input frequencies of 115 and 105 MHz and chirps with a total excursion of 2.5 MHz and 10 ms.



(b)

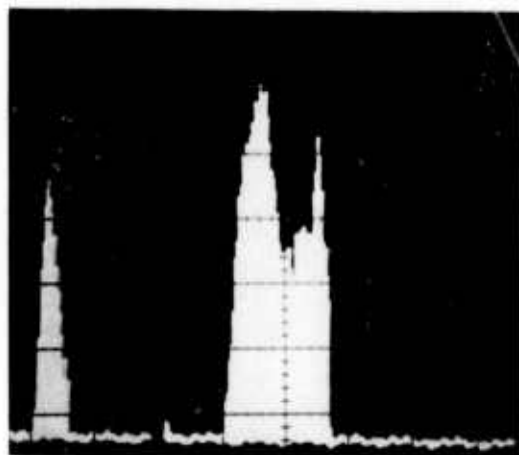
INVERSE TRANSFORM  
= IMAGE

→ | ← 1 s

FIG. 4.3-6(b)--The inverse Fourier transform taken with a spectrum analyzer.

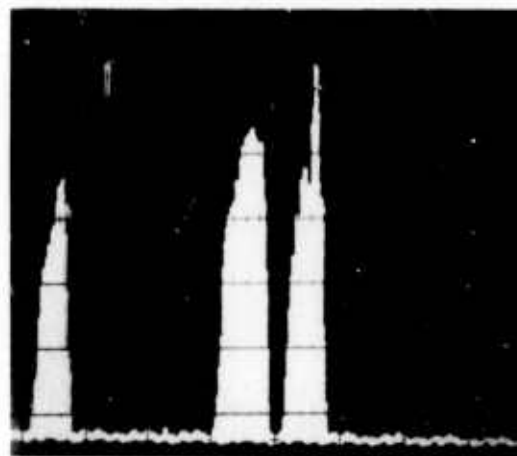
the configuration of the original object. It is apparent that the output bandwidth is determined by the chirp rate, and that the Fourier transform technique samples any point on the image for the whole length of the chirp. Thus the use of this technique provides a considerable enhancement of the signal-to-noise ratio, as compared to employing a direct narrow pulse scan. To demonstrate this feature, it is interesting to compare the output shown in Fig. 4.3-6(b) to the output obtained with the direct imaging system described in Section 4.2.3 and represented in Fig. 4.2-6(b). The objects have the same periodicity in both cases and the convolvers are identical. It is evident that the resolution, showing up in the sharpness of the picture, and the signal-to-noise ratio are much improved by the use of the transform system.

A measure of the resolution was carried out with a similar set-up and a grating with a periodicity of  $l = 175 \mu\text{m}$ . The frequency offset to introduce between the center frequencies of the input chirped signals is therefore 20 MHz. The semiconductor was uniformly illuminated over 5 mm and an opaque strip superimposed in order to create a dark slit in the optical signal. This method was adopted in preference to the opposite method in which a slit of light is used to illuminate the semiconductor because the "white" output signal level is not very uniform. With this method, the effect of the light is more easily evaluated. Figure 4.3-7(a) shows the output amplitude variation with time for a uniform white light illumination of 5 mm of silicon. The output is not flat due to some spatial irregularities in the airgap coupling and local variations in light sensitivity. This a major inconvenience in making a viable imaging



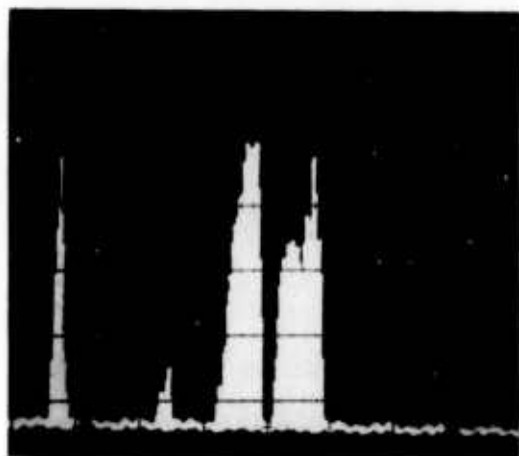
UNIFORM ILLUMINATION

(a)



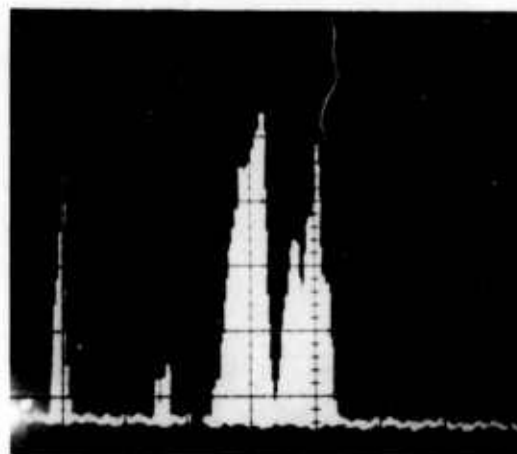
0.93 mm DARK SLIT

(b)



0.66 mm DARK SLIT

(c)



0.24 mm DARK SLIT

(d)

FIG. 4.3-7--Examples of A-scans obtained with a Fourier transform imaging system. The total input bandwidth is  $B_C = 14$  MHz.  
(a) Uniform illumination of 5 mm of semiconductor;  
(b), (c), (d) Superposition of dark slits of various widths.

system. Yet, the study of the resolution is not much affected by this problem, if we look at the effect on the image, of the introduction of a dark slit in the optical input. We use Fig. 4.3-7(a) as a reference, and by comparing it to similar images taken in the presence of the dark slits, we obtain the effect of the slit alone.

If  $B_C$  is the total input bandwidth, i.e., twice one chirp bandwidth, the minimum resolvable spot is  $d_s$ , whose expression is given by Eqs. (A-14) or (A-25),

$$d_s = v/B_C . \quad (4.3-11)$$

As mentioned earlier in Section 4.3.1, the maximum bandwidth acceptable not to deteriorate the signal-to-noise ratio, is equal to the frequency offset  $\Delta F$ . Hence, the minimum resolvable spot with a given system is

$$d_{s \min} = v/\Delta F . \quad (4.3-12)$$

The grating will, in addition, have the effect of widening the apparent width of small details by an average of one half period  $l/2$ . The practical minimum resolution is therefore  $1.5l$ , i.e., in this case 0.25 mm.

In Fig. 4.2-7, we show some of the A-scans obtained with  $B_C = 14$  MHz and  $T_C = 140 \mu s$ , with a uniform illumination (a), and with dark slits of various widths (b), (c), (d). Theoretically, one would expect a  $\sin X/X$  type of decrease due to the slit. Experimentally, due to diffusion in the semiconductor (MTF), the very sharp edges in the focused image disappear and as seen in Fig. 4.2-7(b), (c), (d), only the main

lobe of this decrease is visible. Its width varies as the slit width and the depth of modulation weakens for the narrowest slit (0.24 mm), whose width is comparable to the resolution limit for this particular case ( $d_s = 0.25$  mm). From these oscillograms and similar ones obtained with  $B_C$  of 6.4 MHz and 18 MHz, we measured the apparent widths of the dark slits and compared them to the actual values. The results are summarized in Table 4.1. When the total input bandwidth is 6.4 MHz,  $d_s = 0.545$  mm and the wider slits of width 0.93 and 0.66 mm are well detected; their apparent width is found to be within 10% of the true value. By contrast, the narrower slits are not seen at all, for their width is much smaller than the resolution limit of 0.545 mm. With larger bandwidths,  $B_C = 14$  MHz and  $B_C = 18$  MHz, the resolution limit due to the transform system,  $d_s$ , is reduced to 0.250 and 0.195 mm respectively, and the narrowest slit used (0.17 mm) is seen. It appears wider because of the previously mentioned widening effect of the grating when the spot size becomes of the order of the grating period  $l$ . As seen in Table 4.1, the apparent width is comparable to what we define as the "artificial" width

$$d_{\text{artificial}} = d_{\text{real}} + l/2 .$$

As a conclusion, with  $B_C = 18$  MHz, the resolution limit is approximately 0.25 mm, a result similar to what was obtained previously in the Fresnel transform system. It corresponds to 0.35 mm, i.e., 3 points per mm of silicon, as had been expected.

TABLE 4.1

EXPERIMENTAL STUDY OF THE RESOLUTION IN A FOURIER TRANSFORM IMAGING SYSTEM

Chirp Characteristics	$B_C$ (MHz)	6.4	14	18
	$T_C$ ( $\mu s$ )	140	140	140
Resolution (theory)	$d_s$ (mm)	0.545	0.250	0.195
Slit width (mm)	Experimental width (mm)			Remarks
0.93	0.70 $\pm$ 0.10	0.95 $\pm$ 0.10	-----	
0.66	0.65 $\pm$ 0.05	0.64 $\pm$ 0.04	-----	
0.24	not detect.	0.37 $\pm$ 0.05	-----	artificial width 0.24 + 0.08 = 0.32
0.17	not detect.	0.25 $\pm$ 0.05	0.25 $\pm$ 0.05	artificial width 0.17 + 0.08 = 0.25 resolution limit

An example of a picture taken with a Fourier transform imaging system by mechanically scanning in one direction, is shown in Fig. 4.2-8(a). The chirped signals have a bandwidth of 5.7 MHz and a duration of  $40 \mu\text{s}$  ( $B_C = 11.4 \text{ MHz}$ ). The portion of the semiconductor actually used extends over 11 mm, and corresponds to an acoustic delay of  $T_A = 3 \mu\text{s}$ ; the resulting number of resolvable points is therefore  $N = B_C \cdot T_A = 35$ .

In an actual system, the output of the imaging device, i.e., the Fourier transform signal, is sent through a transmission channel. The reconstitution of the image — the decoding by second Fourier transform — is carried out at the receiver end of the channel. The frequency in the transmitted signal therefore corresponds to time in the decoded image. In Fig. 4.2-8(b), (c), (d), we have simulated reduction or alteration of the transmission channel bandwidth. The total bandwidth required for an accurate reconstitution is 800 kHz [see (b)]. Now, if the lower or intermediary frequencies of the bandwidth are cut-off, portions of the image will be lost accordingly, but this will not affect the quality of the remaining image. This is a unique feature of the Fourier transform system. In contrast, in a classical direct imaging system, or even in a Fresnel Transform system (see Section 4.3.1), a bandwidth reduction would result in the degradation of the entire image.

In some imaging applications, the quality of the image does not have to be uniform over the entire field of view; the center part should be better resolved than the outer portions. This is particularly true in some TV tracking systems, and in such systems, a transform coding of the previous type with a tapered bandwidth would be suitable.





(a)



NO FILTER  
(0-800KHz)

(b)



HI-PASS FILTER  
( $F_c = 250$ KHz)

(c)



STOP-BAND FILTER  
(400-750KHz)

(d)

FIG. 4.3-8--(a) Two-dimensional picture taken with a Fourier transform imaging system using chirped signals of total bandwidth  $B_C = 11.4$  MHz.

(b), (c), (d) Demonstration of the effect on the reconstituted image of a frequency filtering of the Fourier transform signal.

## CHAPTER V

### CONCLUSIONS

In this work we have been concerned with acoustic surface waves on a piezoelectric substrate and their interaction with a neighboring semiconductor separated by a small airgap. The emphases has been put on the capabilities of the system to generate the convolution product of two signals. It has been shown that the semiconductor can produce a large nonlinear coupling between acoustic waves and that high efficiency signal processors can be built. In addition, new types of optical imaging systems have been demonstrated by making use of the fact that the semiconductor is a photosensitive continuous array which can be scanned by acoustic waves.

We have presented a theory of the semiconductor-airgap-piezoelectric coupling. This theory is new in that it accounts for any depletion, accumulation or inversion layer at the surface of the semiconductor. Such layers exist on real surfaces because of the presence of surface states, and they can be varied artificially by applying a bias field across the structure. Experimental verification in the case of  $\text{LiNbO}_3$ -Si systems resulted in a direct measurement of the surface state distribution and time constant on Silicon, and in the first demonstration showing that acoustic field techniques are potential tools for the investigation of semiconductor surfaces. It has also been ascertained that the convolver efficiency is maximum when a depletion layer is present at the surface of the semiconductor; a result which has been left out in previous theories.

We have shown that the study of the convolution output can result in the direct measurement of semiconductor parameters which are otherwise difficult to evaluate. This measurement is also non-destructive since no electrode is deposited on the surface of the semiconductor and it is simple to change samples. To use the acoustic device, in its present form as an investigation tool for semiconductor surfaces, one would have to employ small semiconductor samples to ensure a uniform interaction between the piezoelectric and semiconductor media. Particular care should be paid to the preparation and mounting of the samples, and a study under vacuum is advisable.

We have described, at length, the effect of a bias voltage and how it can be interpreted. A study versus controlled illumination and temperature would also be of interest if more detailed information is needed. Such a study was beyond the scope of this work, but it could be the nucleus of some future work in the field of semiconductor physics.

The characteristics of the system as a signal processor have been studied. A convolution efficiency of  $-44$  dBm, one of the highest values reported, with time-bandwidth product in the 200 range, have been observed. The results are in good agreement with theory. Several signal processing applications have been demonstrated. We have shown that the convolver is, in essence, a programmable linear filter. As such, it has been used as a compression filter or a matched filter for the recognition of digital and analog codes. Due to the parametric nature of the wave coupling in the system, time inversion of a signal is possible and

autocorrelation have been demonstrated for the first time by cascading two devices. Other parametric applications have been studied, to a lesser extent.

We employed the photoconductivity of the semiconductor to turn the convolution device into an imaging device. By introducing a periodicity in the optical signal and operating the system with offset input center frequencies, we have shown low dark current and large dynamic range operation. These improvements have been shown to agree well with theoretical calculations. In addition, a new method of scanning the image has been demonstrated. Long time signals are fed into the acoustic convolver and a real time Fourier or Fresnel transform of the image is generated. A major improvement in signal-to-noise ratio has been obtained and the scan velocity has been made arbitrary.

It should be noted that these scanning methods are not possible with electron beam devices like the vidicons, and they have not been demonstrated with CCDs. They may very well not be applicable to these devices. With acoustic systems, these methods are particularly simple to implement and they increase the versatility of the system to a large extent.

These new concepts have all been tested with the separated medium semiconductor-piezoelectric convolver because of the experience we have had with this structure and because of its versatility. The airgap uniformity and the semiconductor surface treatment are problems requiring particular attention in this device configuration. Reproducible devices will have to be monolithic. Such structures are being developed and the principles presented here would apply directly to them.

## APPENDIX A

### IMAGING BY TRANSFORM CODING

We give here a derivation of the mathematical results associated with the convolution and filtering processes that take place in the complete imaging systems using transform techniques.

#### Notation:

$L$  = length of the semiconductor

$v$  = acoustic wave velocity

$T_A = L/v$  acoustic delay under the semiconductor.

The input chirped signals have the following characteristics:

- duration  $T_C$
- chirp rate  $\mu_1$  and  $-\mu_2$  in  $\text{rd/s}^2$
- total input bandwidth  $B_C = (\mu_1 + \mu_2) T_C/2\pi$
- dispersive filter bandwidth  $B_s = (\mu_1 - \mu_2) T_C/2\pi$  .

#### Convolver Output:

We take the center of the semiconductor as the origin  $z = 0$  .  
If the two input electrical signals are  $f_1(t)$  and  $f_2(t)$  and the carriers density is uniform, the output voltage of the convolver  $h(t)$  is given by

$$h(t) = \int_{-L/2}^{L/2} f_1(t - z/v) f_2(t + z/v) dz \quad . \quad (A-1)$$

Now let  $f_1$  and  $f_2$  be the chirped signals of center frequency  $\omega_1$  and  $\omega_2$  and chirp rate  $\mu_1$  and  $-\mu_2$ , respectively:

$$f_1(t) = \exp j \left( \omega_1 + \frac{\mu_1 t}{2} \right) t, \quad (\text{A-2})$$

and

$$f_2(t) = \exp j \left( \omega_2 - \frac{\mu_2 t}{2} \right) t. \quad (\text{A-3})$$

Due to the presence of the grating, we assume no dark current and hence the output of the convolver, from any point  $z$  in the sample, is proportional to the light generated carrier density  $n(z)$  and we express this output as

$$h(t) = \exp(j\omega_3 t) \int_{-L/2}^{L/2} n(z) \exp j \left[ \frac{\mu_1 - \mu_2}{2} \left( t^2 + \frac{z^2}{v^2} \right) - \frac{\mu_1 + \mu_2}{v} zt \right] dz \quad (\text{A-4})$$

The output corresponding to one spot of light at  $z_0$  is obtained by letting  $n(z) = \delta(z - z_0)$  in Eq. (A-4)

$$h_0(t) = \exp j \left[ \omega_3 - \frac{\mu_1 + \mu_2}{v} z_0 + \frac{\mu_1 - \mu_2}{2} t \right] t \times \exp j \left( \frac{\mu_1 - \mu_2}{2} \right) \frac{z_0^2}{v^2}$$

$h_0(t)$  is an FM chirp with a chirp rate  $\mu_1 - \mu_2$  and its center frequency is the linear function of position

$$\omega(z_0) = \omega_3 - \frac{\mu_1 + \mu_2}{v} z_0 \quad (A-5)$$

$h_0(t)$  can also be expressed as follows

$$h_0(t) = \exp j \left[ \omega_3 t + \frac{\mu_1 - \mu_2}{2} \left( t - \frac{z}{v_s} \right)^2 - \frac{2\mu_1\mu_2}{\mu_1 - \mu_2} \left( \frac{z}{v} \right)^2 \right] \quad (A-6)$$

where we note the time delay  $z/v_s$  where  $v_s$  is defined by the relation

$$v_s = \frac{\mu_1 - \mu_2}{\mu_1 + \mu_2} v \quad (A-7)$$

To reconstitute the original image  $n(z)$ , we must thus feed  $h(t)$  into a filter matched to a chirp rate  $\mu_1 - \mu_2$  and a chirp length  $T_C$ . Such a filter must have an impulse response proportional to  $h(-t)$ ; this impulse response, denoted  $f(t)$ , is therefore given by the relation

$$f(t) = A \cdot \exp j \left[ \omega_3 t + \frac{\mu_1 - \mu_2}{2} t^2 \right] \cdot \Pi \left( \frac{t}{T_C} \right) \quad (A-8)$$

where  $\Pi$  is unity in the interval  $[-T_C/2, T_C/2]$  and zero outside it;  $A$  is a normalization factor obtained by writing that the amplitude response of the filter is unity over its bandwidth, i.e.,

$$\left| \int f(t) \exp(j\omega t) dt \right| = 1, \text{ for } \omega_3 - (\mu_1 - \mu_2)T_C/2 < \omega < \omega_3 + (\mu_1 - \mu_2)T_C/2$$

One can find<sup>59</sup> that  $A = (B_s/T_C)^{1/2}$ . We did not account for the time delay in the expression for  $f(t)$ . The output of the filter is given by the convolution integral of the input  $h(t)$  and the impulse response  $f(t)$ , hence

$$g(t) = \int h(\tau) \cdot f(t - \tau) d\tau \quad (\text{A-9})$$

By using Eqs. (A-4) and (A-8),  $g(t)$  can be expressed as follows

$$g(t) = \left( \frac{B_s}{T_C} \right)^{1/2} \int_{-L/2}^{L/2} n(z) \exp j \left\{ \omega_3 t + \frac{\mu_1 - \mu_2}{2} \left[ \left( \frac{z}{v} \right)^2 - t^2 \right] \right\} \\ \times \int_{t-T_C/2}^{t+T_C/2} \exp \left[ j(\mu_1 - \mu_2) \tau \left( t - \frac{z}{v_s} \right) \right] d\tau \quad (\text{A-11})$$

The integral over  $\tau$  introduces a  $\sin X/X$  function. After a few rearrangements, we obtain



$$g(t) = \sqrt{B_s T_C} \exp(j\omega_3 t) \int_{-L/2}^{L/2} n(z) \times \frac{\sin \pi B_s (t - z/v_s)}{\pi B_s (t - z/v_s)} \exp \left[ -j \frac{2\mu_1 \mu_2}{\mu_1 - \mu_2} \cdot \left( \frac{z}{v} \right)^2 \right] dz \quad (A-12)$$

The  $\sin X/X$  function is the "scanning function." It is peaked about the point  $z = v_s(t)$ , hence  $v_s$  is the actual scan velocity given by the relation

$$v_s = \frac{\mu_1 - \mu_2}{\mu_1 + \mu_2} v = v \frac{B_s}{B_C} \quad (A-13)$$

The 3 dB width of the "scanning function" defines the minimum resolvable spot  $d_s$ :

$$d_s = \frac{v_s}{B_s} = \frac{v}{B_C} \quad (A-14)$$

The number of resolvable spots is therefore given by

$$N = \frac{L}{d_s} = B_C T_A = B_s T_C \quad (A-15)$$

The last equality comes from the definitions of the velocities  $v$  and  $v_s$ ; we can indeed write

$$L = vT_A = v_s T_C .$$

For medium-to-high resolution ( $N \geq 30$ ), the scanning function is sharply peaked about  $z = v_s(t)$ . In this case it can be shown that over the center lobe of width  $2d_s$ , the phase error, in the integral of Eq. (A-12), is only  $\pi/N$ . We may therefore approximate the phase term in this integral by its value at  $z = v_s(t)$ . The limits of integration can also be removed to infinity if we consider that  $n(z)$  is zero outside the interval  $[-L/2, L/2]$ . Finally, to obtain the amplitude of the reconstituted image, we approximate the scanning function by the dirac function

$$\frac{v_s}{B_s} \delta(z - v_s(t)) .$$

Equation (A-16) follows:

$$g(t) = \sqrt{\frac{T_C}{B_s}} v_s n(v_s t) \exp - j \left[ \frac{2\mu_1 \mu_2 (\mu_1 - \mu_2)}{(\mu_1 + \mu_2)^2} \cdot t^2 + \omega_3 t \right] . \quad (A-16)$$

$g(t)$  is a replica of  $n$ , chirped with a chirp rate approximately equal to  $\mu_1 - \mu_2$  and a center frequency  $\omega_3$ .

### Comparison with the Direct Imaging System

In a direct imaging system, a narrow pulse of width  $\theta$  scans the semiconductor at a velocity  $v$ . The output is

$$g_{\text{direct}}(t) = \exp(j\omega_3 t) \int n(z) \Pi \left[ \frac{t - z/v}{\theta} \right] dz.$$

The resolution is simply  $v\theta$  and the number of resolvable spots  $\frac{L}{v\theta} = \frac{T_A}{\theta}$ . Besides the output bandwidth is  $\theta^{-1}$ . The  $\Pi$  function can be approximated by  $v\theta \delta(x - vt)$  and  $g_{\text{direct}}(t)$  becomes

$$g_{\text{direct}}(t) = v\theta n(vt) \exp(j\omega_3 t). \quad (\text{A-17})$$

For a given resolution let us now compare the  $S/N$  ratio in the two systems.

In the chirp system the signal amplitude is given by Eq. (A-16) and the noise is proportional to the bandwidth  $B_s$ . In the direct imaging system the signal amplitude is given by Eq. (A-17) and the bandwidth used is  $\theta^{-1}$ ; hence

$$(S/N)_{\text{chirp system}} = \frac{v_s^2 T_C / B_s}{4kT B_s}$$

$$(S/N)_{\text{direct system}} = \frac{(v\theta)^2}{4kT\theta^{-1}}.$$

Since the resolutions have to be identical, we can write

$N = T_A \Theta^{-1} = T_A B_C$ . We then obtain the S/N improvement  $G$  provided by the Transform Coding of the image.  $G$  is given by

$$G = T_C B_C. \quad (A-18)$$

We used Eq. (A-14). Equivalent forms for  $G$  are readily derived:

$$G = N \frac{T_C}{T_A} = N \frac{v}{v_s} = N \frac{B_C}{B_s} \quad (A-19)$$

#### Design Curves

We denote by  $a$  the dispersion of the reconstitution filter (in Hz/sec), by definition of  $a$ ,  $2\pi a = \mu_1 - \mu_2$ . Besides, we call  $B_1$  and  $B_2$  the frequency excursion in the two input chirped signals so that  $2\pi B_1 = \mu_1 T_C$  and  $2\pi B_2 = \mu_2 T_C$ . With these additional notations we give below a summary of the results needed in designing the system:

$$a T_C = B_1 - B_2$$

$$B_C = B_1 + B_2$$

$$B_s = B_1 - B_2$$

$$N = B_s T_C = B_C T_A.$$

We can express  $B_C$ ,  $T_C$  and  $B_s$  in terms of the acoustic delay time  $T_A$ , the filter dispersion  $a$  and the number of resolvable spots  $N$ . We obtain

$$\begin{aligned} B_C &= N/T_A \\ T_C &= (N/a)^{1/2} \\ B_s &= (aN)^{1/2} \end{aligned}$$

Figure A-1(a) gives plots of  $B_C$ ,  $T_C$  and  $B_s$  vs  $N$  in the particular experimental case where  $T_A = 4 \mu\text{sec}$  and  $a$  is  $3 \text{ MHz}/40 \mu\text{sec}$ . These plots allow us to determine  $B_1$ ,  $B_2$  and  $T_C$ , the chirp characteristics, to achieve any resolution  $N$  below 120. Figure A-1(b) gives plots of  $T_C$  and  $B_s$  vs  $a$  for the three resolutions  $N = 120, 200$  and  $300$ . If the line time  $T_C$  and the resolution  $N$  are given, one can therefore find what dispersive filter to use.

#### The Particular Case of the Fourier Transform Coding

When the two input chirped signals have equal and opposite chirp rates, the output of the convolver is given by Eq. (A-4) where

$$h(t) = \exp(j\omega_3 t) \int_{-L/2}^{L/2} n(z) \exp(-j2\mu z t/v) dz \quad (\text{A-20})$$

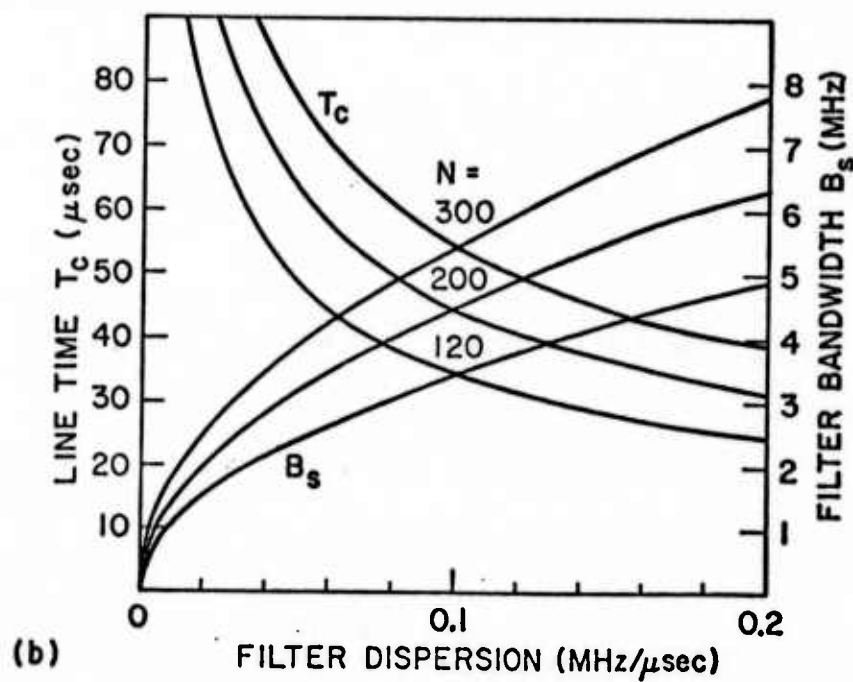
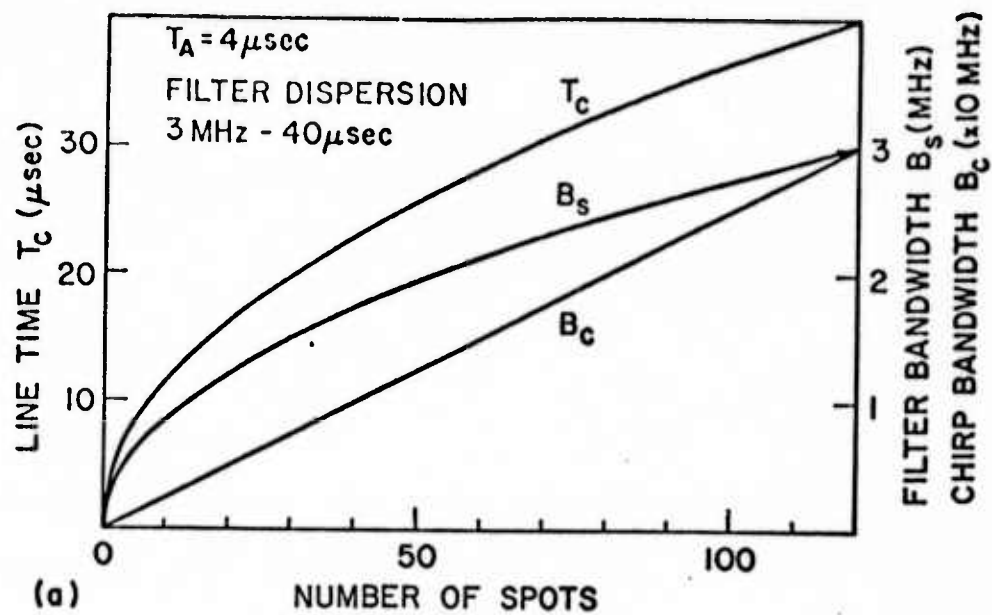


FIG. A-1 Design curves for the imaging system by Fresnel transforms.

- (a) Line time, filter bandwidth and chirp bandwidth  
 $T_A = 4 \mu\text{s}$  and  $a = 3 \text{ MHz}/40 \mu\text{s}$ .
- (b) Line time and filter bandwidth vs filter dispersion  
for various numbers of resolvable spots.

$h(t)$  is the Fourier Transform of  $n(z)$ , the instantaneous frequency being

$$\omega(z) = \omega_3 - 2\mu z/v \quad (\text{A-21})$$

Reconstitution of the image is done by feeding  $h(t)$  into a spectrum analyzer of center frequency  $\omega_3$ . If  $\bar{T}$  is the integration time and  $a$  the frequency scanning rate (in Hz/s) in the spectrum analyzer, its output is given by

$$g(t) = \sqrt{a} \int_{t-\bar{T}/2}^{t+\bar{T}/2} \int_{-L/2}^{L/2} n(z) \exp \left[ j \left( \omega_3 - \frac{2\mu z}{v} \right) t_1 \right] \times \exp \left[ -j \left( \omega_3 - 2\pi a t \right) t_1 \right] dt_1 dz \quad (\text{A-22})$$

where  $\sqrt{a}$  is the normalization factor. The integration over  $t_1$  is straightforward and it yields the following result

$$g(t) = \bar{T} \sqrt{a} \int_{-L/2}^{L/2} n(z) \frac{\sin \pi a \bar{T} (t - z/v_s)}{\pi a \bar{T} (t - z/v_s)} \times \exp \left[ -j \left( \frac{\mu z}{v} - \pi a t \right) \bar{T} \right] dz \quad (\text{A-23})$$

This result is the equivalent of Eq. (A-12) and we can draw similar conclusions. The actual scan velocity  $v_s$ , the minimum resolvable spot  $d_s$  and the number of resolvable spots  $N$  are respectively

$$\begin{aligned} v_s &= v\pi a/\mu \\ d_s &= \pi v/\mu\bar{T} \\ N &= L/d_s = T_A\mu\bar{T}/\pi \end{aligned} \quad (\text{A-24})$$

To obtain the amplitude of the reconstituted image, we approximate the  $\sin X/X$  function of Eq. (A-23) by the Dirac function

$$\frac{v_s}{a\bar{T}} \delta(z - v_s t)$$

Eq. (A-25) follows

$$g(t) \sim \frac{1}{\sqrt{a}} v_s n(v_s t) \quad (\text{A-25})$$

The noise in the transform system is proportional to the spectrum analyzer bandwidth  $a\bar{T}$ ; the signal amplitude is given by Eq. (A.25).

Hence

$$\begin{aligned} (S/N)_{\text{Transform System}} &= \frac{v_s^2/a}{4kT a\bar{T}} \\ (S/N)_{\text{Direct System}} &= \frac{(v\theta)^2}{4kT \theta^{-1}} \end{aligned}$$



as we saw earlier. The resolutions of the two systems have to be equal, hence  $N = T_A \mu \bar{T} / \pi = T_A \Theta^{-1}$  ; the S/N improvement  $G$  provided by the transform coding of the image is therefore given by

$$G = \mu \bar{T}^2 / \pi \quad (\text{A-26})$$

It will be noted that the bandwidth of the spectrum analyzer  $a\bar{T}$  is the equivalent of the filter bandwidth  $B_s$  of the Fresnel Transform system. Furthermore in practice, the integration time  $\bar{T}$  is greater or equal to the chirp time  $T_C$  ,  $T_C$  should be used in Eq.(A-24), (A-26) and all the results of the Fourier Transform system reduced to those derived earlier for the Fresnel Transform system.

## APPENDIX B

### SILICON CLEANING AND OXIDATION PROCEDURES

We give here the Silicon cleaning and oxidation procedures we have followed in the preparation of the silicon wafers which required a thermally grown oxide layer. The cleaning procedure was developed by B. T. Khuri-Yakub at the Stanford Integrated Circuits Laboratory.

#### Wafer Cleaning:

Use a clean quartz beaker, clean tweezers and a clean quartz wafer holder.

1. Boil in trichlorethylene for 5 minutes.
2. To remove any photoresist or wax, heat in hot  $\text{H}_2\text{SO}_4:\text{H}_2\text{O}_2$  (3:1) for 10 minutes.
3. Rinse in de-ionized (DI)  $\text{H}_2\text{O}$  for at least 1 minute.
4. Submerge in warm solution of  $\text{H}_2\text{O}:\text{H}_2\text{O}_2:\text{NH}_4\text{OH}$  (5:1:1) for 5 to 10 minutes (while in the above solution, scrub with Q-tip only if needed).
5. Rinse in DI  $\text{H}_2\text{O}$  for at least 1 minute.
6. Submerge in warm solution of  $\text{H}_2\text{O}:\text{H}_2\text{O}_2:\text{HCl}$  (5:1:1) for 5 to 10 minutes.
7. Rinse in DI  $\text{H}_2\text{O}$  for at least 1 minute.
8. Dip in 50:1 -  $\text{H}_2\text{O}:\text{HF}$  solution for 30 seconds.
9. Rinse thoroughly in DI  $\text{H}_2\text{O}$  for at least 5 minutes; then rinse several times in double distilled  $\text{H}_2\text{O}$ . Blow dry with  $\text{N}_2$ , and process. Do not store.

Thermal Oxidation:

- 15 minutes in wet  $O_2$  or 30 minutes in dry  $O_2$  at  $1200^{\circ}C$  to obtain approximately  $1000 \text{ \AA}$  of oxide.
- Then 5 minutes annealing in  $N_2$  at  $1200^{\circ}C$  .

## REFERENCES

1. R. M. White and F. W. Voltmer, Appl. Phys. Letters 8, 40-42 (1966).
2. J. H. Collins, K. M. Lakin, C. F. Quate, and H. J. Shaw, Appl. Phys. Letters 13, 314-316 (1968).
3. W. C. Wang and P. Das, "Surface Wave Convolver via Space Charge Nonlinearity," 1972 IEEE Ultrasonics Symposium Proceedings, 316-321 (1972).
4. O. W. Otto and N. J. Moll, Electronics Letters 8, 600-602 (1972).
5. M. Yamanishi and T. Kawamura, "Acoustic-Surface-Wave Convolver Using Nonlinear Electron Interactions in Coupled Semiconductor-Piezoelectric Systems," 1972 IEEE Ultrasonics Symposium Proceedings, 288-291 (1972).
6. C. F. Quate and R. B. Thompson, Appl. Phys. Letters 16, 494-496 (1970).
7. T. Oseki and S. Saito, IEEE Trans. Sonics and Ultrasonics SU-18, 215-219 (1971).
8. N. J. Moll, O. W. Otto, and C. F. Quate, J. de Physique 33, Colloque C-6, Supplement, 231-234 (November-December, 1972).  
Also: C. F. Quate, IEEE Trans. Sonics and Ultrasonics SU-21, 283-288 (1974).
9. S. Takada, H. Hayakawa, and N. Mikoshiba, "Surface-Wave-Acousto-electric Image Scanner," Proc. of the Fifth Conference (1973 International) on Solid-State Devices, 194-198. Also:  
T. Shiosaki, T. Kuroda, and A. Kawabata, Appl. Phys. Letters 26, 7, 360-362 (1975).

10. H. Gautier, G. S. Kino, and H. J. Shaw, "Acoustic Transform Techniques Applied to Optical Imaging," 1974 IEEE Ultrasonics Symposium Proceedings, 99-103 (1974).
11. L. A. Coldren, Appl. Phys. Letters 18, 317-319 (1971).  
Also: "Monolithic Acoustic Surface Wave Amplifiers," Ph.D. Dissertation, Stanford University (1972).
12. B. T. Khuri-Yakub and G. S. Kino, Appl. Phys. Letters 25, 188-190 (1974).
13. M. Luukkala and P. Merilainen, Electronics Letters 10, 6, 80-81 (1974).
14. L. A. Coldren, Appl. Phys. Letters 25, 473 (1974).
15. S. Ludvik, "Acoustic Surface Wave Interactions in Piezoelectric Semiconductors," Ph.D. Dissertation, Stanford University (1972).
16. T. Grudkowski and C. F. Quate, Appl. Phys. Letters 25, 99-101 (1974).
17. T. W. Grudkowski and C. F. Quate, "Optical Image Scanning using Nonlinear Surface Wave Interaction in GaAs," 1974 IEEE Ultrasonics Symposium Proceedings, 749-752 (1974).
18. B. A. Auld, Acoustic Fields and Waves in Solids, (Wiley-Interscience, 1973), Vos. I and II.
19. G. S. Kino, S. Ludvik, H. J. Shaw, W. R. Shreve, J. M. White, and D. K. Winslow, IEEE Trans. on Microwave Theory and Techniques MTT-21, 4, 244-255 (1973).
20. O. W. Otto, J. Appl. Phys. 45, 10, 4373-4383 (1974). Also:  
O.W. Otto, "Theoretical Comparison of the Spacecharge-Enhanced Acoustic Surface Wave Convolvers," 23rd Microwave Research Institute

Symposium on Optical and Acoustical Micro-Electronics, New York, April 16-18, 1974.

21. S. Takada, K. Hoh, H. Hayakawa and N. Mikoshiba, Proc. of the 4th Conference on Solid-State Devices, Tokyo, Supplement to the Japanese J. Appl. Phys. 42, 21-29 (1973).
22. S. M. Sze, Physics of Semiconductor Devices (Wiley-Interscience, 1969).
23. T. C. Lim, E. A. Kraut, and R. B. Thompson, Appl. Phys. Letters 20, 127-129 (1972).
24. W. R. Shreve, "Parametric Interactions of Acoustic Rayleigh Waves," Ph.D. Dissertation, Stanford University (1974).
25. R.S. Cobbold, Theory and Applications of Field-Effect Transistors, (Wiley-Interscience, 1970).
26. P. Richman, MOS Field-Effect Transistors and Integrated Circuits (Wiley-Interscience, 1973).
27. A. S. Grove, Physics and Technology of Semiconductor Devices (Wiley, 1967).
28. G. S. Kino and T. M. Reeder, IEEE Trans. Electron Devices ED-18, 10, 909-920 (1971).
29. A. Many, Y. Goldstein, and W. B. Grover, Semiconductor Surfaces (North-Holland Publishing Co., 1965).
30. W. C. Wang, "A Novel Ultrasonic Oscillator and Convolution Integrator," presented at the Joint Services Technical Advisory Committee Meeting, Polytechnic Institute of Brooklyn, Brooklyn, N.Y., 1966).

31. B. A. Auld and G. S. Kino, IEEE Trans. Electron Devices ED-18, 10, 898-908 (1971).
32. P. L. Castro and B. E. Deal, J. Electrochem. Soc. 114, 225-274 (1967).
33. A. S. Grove, B. E. Deal, E. H. Snow, and C. T. Sah, Solid-State Elec. 8, 145-163 (1965).
34. E. H. Nicollian and A. Goetzberger, Bell Syst. Tech. J. 46, 1055-1134 (1967).
35. H. Hayakawa and G. S. Kino, Appl. Phys. Letters 25, 178 (1974).
36. A. Bers and J. H. Cafarella, Appl. Phys. Letters 25, 133 (1974).
37. J. H. Cafarella, A. Bers, and E. Stern, "Surface Acoustoelectric Correlator with Surface State Memory," 1974 IEEE Ultrasonics Symposium Proceedings 216-219 (1974). Also:  
A. Bers and J. H. Cafarella, "Surface Wave Correlator - Convolver with Memory," 1974 IEEE Ultrasonics Symposium Proceedings 778-787.
38. O. W. Otto, Electronics Letters 8, 623-624 (1972).
39. J. M. White, D.K. Winslow, and H. J. Shaw, Electronics Letters 8, 446-447 (1972).
40. M. V. Luukkala and G. S. Kino, Appl. Phys. Letters 18, 393-394 (1971).
41. L. O. Svaasand, Appl. Phys. Letters 15, 300-302 (1969).
42. W. C. Wang, Appl. Phys. Letters 18, 337-338 (1971).
43. C. W. Turner, I. M. Mason, and J. Chambers, Electronics Letters 7, 696-697 (1971).
44. G. S. Kino, W. R. Shreve, and H. R. Gautier, "Parametric Interactions of Rayleigh Waves," 1972 IEEE Ultrasonics Symposium Proceedings 285-287 (1972).

45. L. R. Adkins, "Monolithic Aluminum Nitride/Silicon-on-Sapphire Strip Coupled Convolvers," 1974 IEEE Ultrasonics Symposium Proceedings 228-231 (1974).
46. I. M. Mason, M. O. Motz, and J. Chambers, Electronics Letters 8, 429-430 (1972). Also:  
P. E. Lagasse, I. M. Mason, and E. A. Ash, IEEE Trans. Microwave Theory and Technique MTT-4, 225-236 (1973).
47. N. K. Batani and E. L. Adler, "Acoustic Convolvers Using Ribbon Waveguide Beamwidth Compressors," 1974 IEEE Ultrasonics Symposium Proceedings 114-116 (1974).
48. Ph. Defranould and C. Maerfeld, "Acoustic Convolver Using Multistrip Beamwidth Compressors," 1974 IEEE Ultrasonics Symposium Proceedings 224-227 (1974).
49. W. R. Shreve and G. S. Kino, "Strip Coupled Acoustic Convolvers," 1973 IEEE Ultrasonics Symposium Proceedings 145-147 (1973).
50. J. M. Smith, E. Stern, A. Bers, and J. Cafarella, "Surface Acoustoelectric Convolvers," 1973 IEEE Ultrasonics Symposium Proceedings 142-144 (1973).
51. M. Yamanishi, T. Kawamura, and Y. Nakayama, Appl. Phys. Letters 21, 146-148 (1972).
52. J. M. Smith, E. Stern, and A. Bers, Electronics Letters 9, 145-146 (1973).
53. G. E. Cook and M. Bernfeld, Radar Signals - An Introduction in Theory and Application, (Academic Press, New York, 1967).



54. G. S. Kino, "Acoustical Scanning of Optical and Acoustic Images,"  
23rd. Microwave Research Institute Symposium on Optical and  
Acoustical Micro-Electronics, New York, April 16-18, 1974.
55. P. V. Lenzo, J. Appl. Phys. 43, 3, 1107-1111 (1972).
56. G. F. Amelio, Scientific American 230, 22-31 (February 1974). Also:  
Review Paper in Electro-Optical System Design (April 1974).
57. M. R. Boudry, Appl. Phys. Letters 22, 530-531 (1973).
58. A. Whitehouse, private communication.
59. A. W. Rihaczek, Principles of High Resolution Radar (McGraw-Hill  
Book Co., 1969).